027735-1-F

NAGW-499

Theoretical and Experimental Models of The Diffuse Radar Backscatter From Mars

A. W. England

May, 1995

THE UNIVERSITY OF MICHIGAN

Radiation Laboratory
Department of Electrical Engineering
and Computer Science
Ann Arbor, Michigan 48109-2122
USA

Final Report for:

NASA GRANT NAGW-2199

THEORETICAL AND EXPERIMENTAL MODELS OF THE DIFFUSE RADAR BACKSCATTER FROM MARS

Work performed during July 1, 1990
through June 30, 1994
(plus a 6 month, no-cost extension)

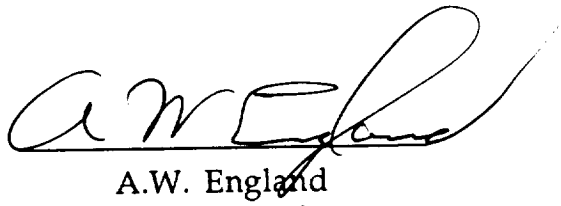

A.W. England
Principal Investigator

Radiation Laboratory
Department of Electrical Engineering
and Computer Science
The University of Michigan
Ann Arbor, MI 48109-2122
Ph: (313) 936-1340
FAX (313) 763-1503
england@eecs.umich.edu

May 19, 1995

Table of Contents

I Statement of Objectives

Our general objective for this work was to develop a theoretically and experimentally consistent explanation for the diffuse component of radar backscatter from Mars. The strength, variability, and wavelength independence of Mars' diffuse backscatter are unique among our Moon and the terrestrial planets. This diffuse backscatter is generally attributed to wavelength-scale surface roughness and to rock clasts within the Martian regolith. Through the combination of theory and experiment, we attempted to bound the range of surface characteristics that could produce the observed diffuse backscatter. Through these bounds we gained a limited capability for data inversion. Within this umbrella, specific objectives were:

(a) To better define the statistical roughness parameters of Mars' surface so that they are consistent with observed radar backscatter data, and with the physical and chemical characteristics of Mars' surface as inferred from Mariner 9, the Viking probes, and Earth-based spectroscopy.

(b) To better understand the partitioning between surface and volume scattering in the Mars regolith.

(c) To develop computational models of Mars' radio emission that incorporate frequency dependent, surface and volume scattering.

II Approach

There is never enough radar scattering data to invert Mars radar backscatter profiles to obtain unambiguous estimates of surface roughness - even if we possessed the scattering theory that would allow us to do so. Our approach to the problem has been to assume something about the statistical roughness characteristics of Mars' surface, and, based upon this roughness model, to develop a limited scattering theory or empirical law that could be used to relate observed backscatter to roughness. We are currently testing this approach by developing a classification algorithm based upon the empirical law developed in this investigation. Applying this algorithm to SIR-C data, we will attempt to classify Andean Volcanics according to their roughness. This application is funded by the SIR-C project and is not strictly a part of the Mars investigation.

III Assumed Surface Statistics

For roughness characteristics, we assumed a power-law surface. Several investigations have suggested that roughness profiles of many natural surfaces obey a power spectrum of the type,

$$S_z(f) = c\, f^{-\beta} \tag{1}$$

[e.g., 7-8, 10, 22, 26, 28, 30-31, 34-35, 52, 60] where S_z is the power spectral density, f is spatial frequency, c is a scaling constant, and β is a constant that is related to the fractal dimension of the surface [e.g., 21]. We tested this hypothesis on several flows of the Mount St. Helens volcano and found that fresh flows in that environment do, in fact, exhibit a power-law spectrum over several decades of spatial frequency both below and above the range of spatial frequencies of observing radars. In contrast, water deposited sediments of Mount St. Helens ejecta do not obey a power-law. While aeolian deposition on Mars may be like fluvial deposition at Mount St. Helens and not obey a power-law, the assumption that Mars volcanic deposition does obey a power law gives us a place to begin. We have presented various of these findings in several forums [65-66] and published the work in Geophysical Research Letters [2]. The GRL paper is included on the following 4 pages.

GEOPHYSICAL RESEARCH LETTERS, VOL. 20, NO. 15, PAGES 1603-1606, AUGUST 6, 1993

MULTI-SCALE ROUGHNESS SPECTRA OF MOUNT ST. HELENS DEBRIS FLOWS

Richard T. Austin and Anthony W. England

Radiation Laboratory, Dept. of Electrical Engineering and Computer Science, University of Michigan

Abstract. A roughness spectrum allows surface structure to be interpreted as a sum of sinusoidal components with differing wavelengths. Knowledge of the roughness spectrum gives insight into the mechanisms responsible for electromagnetic scattering at a given wavelength. Measured spectra from 10-year-old primary debris flow surfaces at Mount St. Helens conform to a power-law spectral model, suggesting that these surfaces are scaling over the measured range of spatial frequencies. Measured spectra from water-deposited surfaces deviate from this model.

Introduction

Recent investigations [Evans et al., 1988; Gaddis et al., 1989] demonstrate that radar images are a useful tool in the study of volcanic terrain. Although there have been experimental investigations of radar scattering by such terrains, there have been few rigorous attempts to link the scattering cross section to quantitative surface roughness. Scattering from many volcanic terrains is difficult to model due to their extreme roughness and short correlation lengths. Rough surface scattering theories often assume that surfaces possess a Gaussian autocorrelation function (and corresponding Gaussian roughness spectrum) [Chen and Fung, 1988; Thorsos and Jackson, 1989]. In contrast, many natural surfaces are better described by power-law spectra [Berry and Hannay, 1978; Sayles and Thomas, 1978; Huang and Turcotte, 1989, 1990; England, 1992]. (These spectral forms are compared in Figure 1.) Rough surfaces that have structure over a wide range of spatial scales may be described using the concepts of fractal geometry introduced by Mandelbrot [1983]. Random rough fractal surfaces have power-law spectra; the slope of such a spectrum is related to the surface's fractal dimension (Austin et al., Special Problems in the Estimation of Power-Law Spectra as Applied to Topographical Modeling, submitted to *IEEE Transactions on Geoscience and Remote Sensing*, 1993, hereinafter referred to as Austin et al., submitted manuscript, 1993). In this report, we examine estimates of the roughness spectra of volcanic debris flows at several spatial scales.

Debris Flow Measurements

Surface roughness measurements were performed on several debris flows near Mount St. Helens (Cascade Range, northwestern United States) during September 1990. Mt. St. Helens was chosen because of its ease of access and its extremely young terrains. The surfaces that we examined were located in the debris avalanche west-northwest of the volcano, along the North Fork Toutle River valley (Figure 2). Most of the debris was deposited during the eruption of Mount St. Helens on 18 May 1980. Since then, the deposits have undergone erosion by wind and water. The sites chosen for measurement were visually representative of principal surface textures, accessible to logging roads, and located in large homogeneous areas which should be distinguishable in a radar image. Figure 3 shows one of the rougher surfaces. A geologic description of the debris avalanche is given by Glicken [1989].

Our objectives were to characterize the surface roughness of the debris flows at scales smaller than, on the order of, and larger than the radar wavelength of common remote sensing radars. Two measurement techniques were used. A computer-driven, 2D laser profilometer recorded surface height profiles of square grids with sides between 8 cm and 1 m in length. The grids were sampled at intervals ranging from 2 mm to 2 cm. We used surveying instruments to measure elevation at grid points within larger square areas measuring 32 m on a side. Sampling intervals within the larger squares were 1–4 m.

The 2D laser profilometer system was designed specifically for this experiment. Its main component is a surveying electronic distancemeter (EDM), which uses an infrared laser to measure distance. The EDM is mounted on an XY table, allowing the EDM to scan a surface area of up to 1 m^2. The EDM laser has a spot diameter of approximately 1.5 mm. In its most precise mode, the standard deviation of the measured surface height is 3 mm. Surface height profiles from a typical grid are shown in Figure 4. While the two large rocks are quite prominent, a larger sample of the surface would show even larger "lumps."

Larger-scale topography was surveyed. Square grids with sides of 32 m were delineated by cables with markers at 1 m intervals. A self-leveling surveying level and stadia rod were then used to measure the surface height at intervals of 1–4 m, depending on the surface roughness.

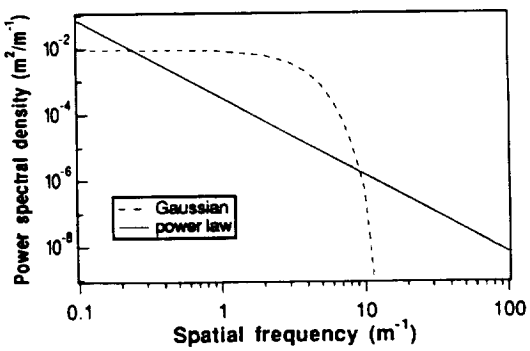

Fig. 1. A comparison of Gaussian and power-law spectra.

Paper Number 93GL01875
0094-8534/93/93GL-01875$03.00

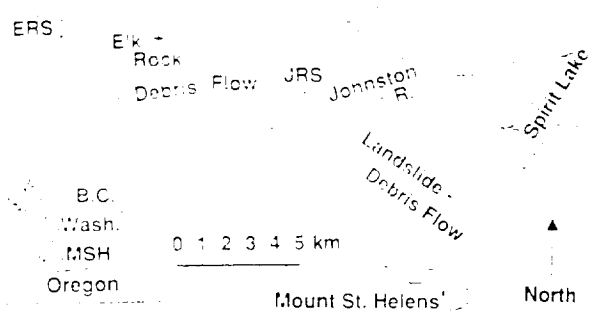

Fig. 2. The Johnston Ridge site (JRS) is located about 10 km northwest of the crater. The Elk Rock site (ERS) is located farther west, about 19 km west-northwest of the crater.

Spectral Estimation

Estimates of the roughness spectrum were calculated from both types of elevation data. Profilometer data suffered from errors which prevented the direct application of spectral estimation techniques. Since the measurements could not be repeated, it was necessary to apply corrective filtering. The procedure is fully described in Austin and England [1991].

As previously noted, investigators have found that many natural surfaces are scaling. Linear profiles of such surfaces have (over the range of measurable spatial frequencies) a surface roughness spectrum (power spectral density of surface height) S_Z that has the form of a power law:

$$S_Z(f) = c|f|^{-\beta}, \tag{1}$$

where f is the spatial frequency and c and β are constants, with $1 < \beta < 3$. β is sometimes called the spectral slope; a power-law spectrum is linear with slope $(-\beta)$ when plotted on a log-log scale.

Power-law surfaces with isotropic statistics have a two-dimensional roughness spectrum S_{Z2D} that has a similar form:

$$S_{Z2D}(f_r) = a f_r^{-\gamma}, \tag{2}$$

where f_r is the radial spatial frequency satisfying $f_r^2 = f_x^2 + f_y^2$, and $2 < \gamma < 4$. Because estimation of directional spectra requires a much greater quantity of data,

Fig. 3. A sample surface scanned by the EDM. The surface has been spray-painted to increase its reflectivity.

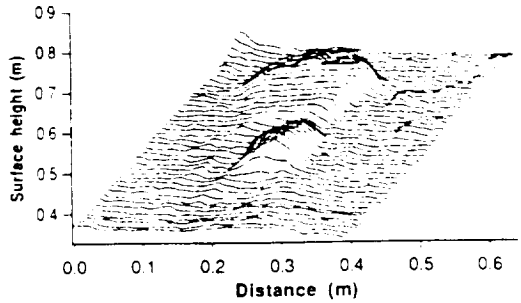

Fig. 4. A typical profilometer scan, showing surface height profiles. The grid measures 40 cm × 40 cm, with data points spaced 1 cm apart. Total surface height variation is 10.8 cm.

we assume in this study that the surfaces have isotropic statistics as a first-order approximation.

Power-law spectra introduce unique difficulties in the spectral estimation process. In a related paper (Austin et al., submitted manuscript, 1993), we describe how Capon's estimator provides an estimate of the roughness spectrum that is better than that given by Fourier-based estimators (such as the periodogram) in the power-law case. Capon's estimator (described in Kay [1988]) essentially customizes a filter at each frequency of interest to minimize the total power output subject to the constraint that the gain at the frequency of interest is unity. In the power-law case, the low-frequency side lobes are reduced, thus Capon's estimator suffers less from spectral leakage, which can make Fourier estimates insensitive to the power-law slope β. Capon's estimator also has less variance than comparable Fourier-based estimators.

Capon's estimator, $\hat{P}_{CAP}(f)$, is obtained by first calculating an estimate of the autocorrelation matrix $\mathbf{R}_{ZZ}$, whose elements are defined as

$$[\mathbf{R}_{ZZ}]_{kl} = E\,[Z[n]Z[n+k-l]], \tag{3}$$

where $Z[n]$ is the surface height and $E[\cdot]$ indicates an expected value. Capon's estimator is then given by

$$\hat{P}_{CAP}(f) = \frac{p\Delta}{\mathbf{e}^H \hat{\mathbf{R}}_{ZZ}^{-1} \mathbf{e}}, \tag{4}$$

where p is the maximum dimension of the autocorrelation matrix, Δ is the sampling interval, $\hat{\mathbf{R}}_{ZZ}^{-1}$ is the inverse of an estimate of the autocorrelation matrix, and

$$\mathbf{e} = \left[\, 1 \quad e^{j2\pi f\Delta} \quad e^{j4\pi f\Delta} \quad \cdots \quad e^{j2\pi(p-1)f\Delta} \,\right]^T, \tag{5}$$

in which f is the spatial frequency. $\mathbf{e}^H$ is the Hermitian transpose of (5).

The bias of Capon's estimator is independent of N (the number of points in a sampled row) but is dependent on p, the dimension of the autocorrelation matrix. For a data set of length N, an increase in p will result in reduced bias at the cost of increased variance. We set $p \approx 0.3N$ and calculated a Capon's spectral estimate for each row of each profilometer or survey grid. (The mean row height was subtracted before calculating the estimate.) The spectral estimates were then averaged over the rows of each grid.

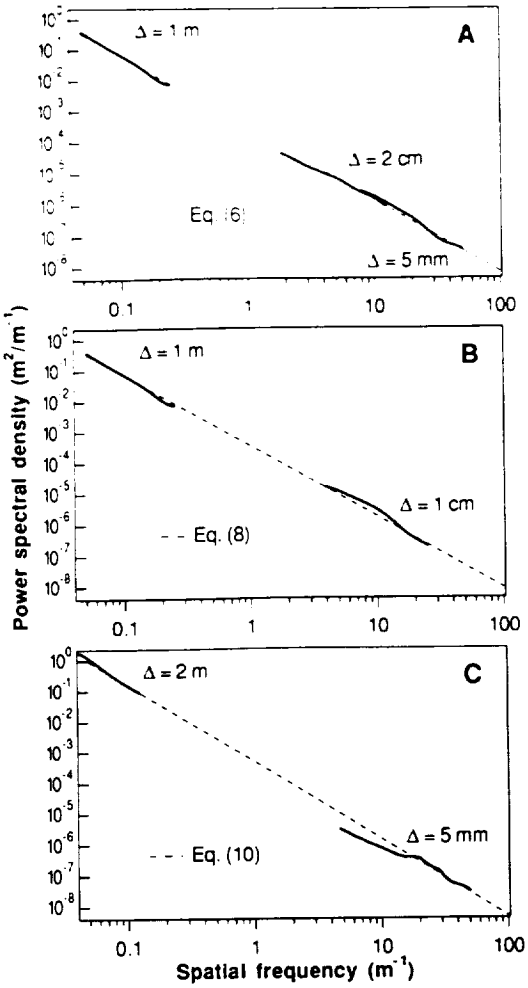

Fig. 5. (A) Survey and profilometer spectra from a JRS primary debris flow. (B) The same survey spectrum with a profilometer spectrum from an adjacent debris flow. (C) Spectra from a mixed terrain survey and a primary debris flow scan at ERS.

The high-frequency half of each averaged estimate was discarded to reduce the effect of aliasing. Averaged estimates at a single scale or at multiple scales were then fit with a power-law function (1), where appropriate, using a minimum absolute deviation fit. Profile (1D) spectra fitting the power-law model were then converted to surface (2D) spectra using the formulation given in (Austin et al., submitted manuscript, 1993), in which the 1D and 2D roughness spectra are related through their corresponding autocorrelation functions and the 2D autocorrelation function is assumed isotropic.

Although this method of determining the surface spectrum from linear profiles was made necessary by the profilometer problems, it is not without benefit. One grid of measured surface heights yields many linear profiles. The profile rows are not completely independent, but the row spectral estimates can still be averaged to obtain a significant decrease in variance, allowing us to set p (in Capon's estimator) higher to decrease the bias. This averaging would not be possible with a two-dimensional estimator, given the same measured data.

Measured Roughness Spectra

The first site that we examined (JRS) was located in the debris flow area adjacent to and due west of Johnston Ridge (see Figure 2). This area of the debris flow exhibited large variations in relief (e.g., 8 m in a 32 m × 32 m survey grid). The roughest surfaces that we measured in this area were the primary debris flow surfaces, i.e., debris flow surfaces whose present state is due to the removal of material by wind and water. Spectra from the roughest of these are shown in Figure 5A. The survey spectrum is the curve extending from 0.05 to 0.25 m^{-1}; the higher frequency spectra were computed from profilometer scans. The linear character of these spectral estimates suggests that a power-law spectrum is appropriate for this surface. The equation of the power-law fit to these estimates is

$$\hat{S}_Z(f) = (3.21 \times 10^{-4})|f|^{-2.34}. \quad (6)$$

(The hat denotes an estimate.) This fit is shown as a dashed line in Figure 5A. While we do not know that the spectrum follows this power law at the intermediate (unmeasured) spatial frequencies, we do think that it is significant that both the meter- and centimeter-scale spectra are well fit by the same power law.

We can convert (6) to an estimate of the surface (2D) spectrum, obtaining the following power law:

$$\hat{S}_{Z2D}(f_r) = (1.77 \times 10^{-4}) f_r^{-3.34}. \quad (7)$$

In Figure 5B, the same survey spectrum is shown together with a profilometer spectrum collected on a similar

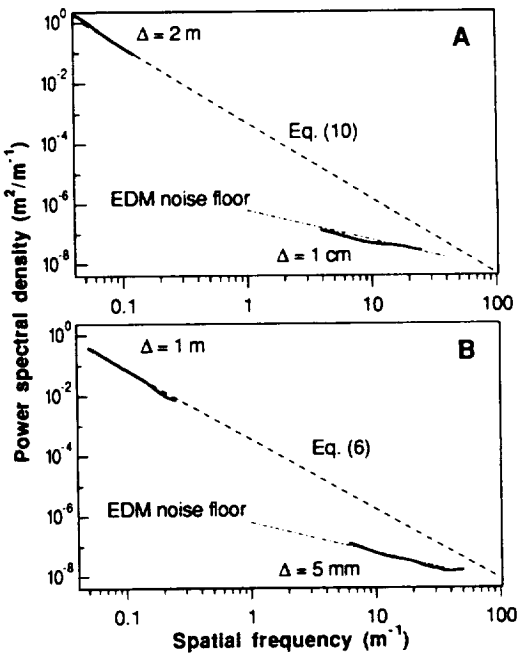

Fig. 6. (A) A profilometer spectrum (Δ = 1 cm) of an ERS sedimented surface, shown with the survey spectrum of the local mixed terrain, the power-law fit (10), and the EDM noise floor. (B) A profilometer spectrum (Δ = 5 mm) of a JRS sedimented surface, shown with the survey spectrum of the surrounding primary debris flow, the power-law fit (6), and the EDM noise floor.

flow near adjacent to the one surveyed. A power-law fit to these estimates gives the following spectra:

$$\hat{S}_{Z}(f) = 1.55 \times 10^{-4} |f|^{-2.51} \quad (8)$$

$$\hat{S}_{Z2D}(f_r) = 1.95 \times 10^{-4} f_r^{-3.51} \quad (9)$$

The other area that we examined, ERS, was located in the North Fork Toutle River valley due west of Elk Rock. The valley was a mixture of hummocky debris mounds scattered across a flat, sedimented plain. A profilometer scan from one of the debris mounds yielded the spectral estimate shown at the high-frequency end of Figure 5C. The figure also shows an estimate from a survey grid containing both terrain types. (The debris mounds were typically smaller than the 32 m × 32 m survey area.) A power-law fit may be appropriate here as well and is shown in the figure. The equations for this fit are

$$\hat{S}_{Z}(f) = (4.98 \times 10^{-4})|f|^{-2.51} \quad (10)$$

$$\hat{S}_{Z2D}(f_r) = (2.86 \times 10^{-4}) f_r^{-3.51} \quad (11)$$

Surfaces formed of water-deposited sediments within the hummocky debris had spectra that were markedly different from those of the primary surfaces. For example, in Figure 6A, we see that the spectral estimate from a scan of such a surface lies on the noise floor due to the limited precision of the EDM. The true spectrum of this surface must lie below this level and therefore cannot form a power-law trend with the survey spectrum of the local mixed terrain. This difference in spectral behavior is consistent with the visible character of the sedimented surface, which appeared quite flat. Similar remarks apply to the profilometer spectrum of a water-deposited sediment at the Johnston Ridge site, which is shown in Figure 6B with the survey spectrum of the surrounding primary debris flow.

Conclusions

Spectral estimates derived from multi-scale topographical measurements of several debris flow surfaces at Mount St. Helens show differences that correspond to observed surface characteristics. The extremely rough surfaces affiliated with 10-year-old primary debris flows possess roughness spectra that are well modeled by a power-law function at certain length scales, implying that these surfaces are scaling over the measured range of spatial frequencies. Surfaces created through sedimentation have spectra that lie below the noise floor at higher spatial frequencies and thus do not fit the power-law model.

While we are not yet able to develop a classifier of volcanic terrains based on surface roughness spectra, this study shows that a power-law spectrum is a reasonable descriptor of some volcanic surfaces. The scattering properties of such surfaces are not well understood. There has been some application of standard scattering models to surfaces of this type, but rougher volcanic terrains often violate assumptions made in these models (e.g., rms height $\ll$ radar wavelength). The present study and the others cited demonstrate the need for power-law scattering models in the remote sensing of volcanic debris flows and other natural surfaces. We are pursuing such a model through both theoretical and experimental studies.

Acknowledgments. The authors thank Bruce Babb and the staff of the Mount St. Helens National Volcanic Monument for their cooperation, Kyle McDonald and Bob Austin for assistance in the surface measurements, and two anonymous reviewers for their thoughtful comments and suggestions. This work is supported under NASA Grant NAGW-2199 and a shared NASA SIR-C project.

References

Austin, R. T., and A. W. England, Surface Characterization of Volcanic Debris Flows at Multiple Scales, in *Proceedings of the 1991 International Geoscience and Remote Sensing Symposium*, pp. 1675–1678, IEEE, New York, 1991.

Berry, M. V., and J. H. Hannay, Topography of random surfaces, *Nature*, *273*, 573, 1978.

Chen, M. F., and A. K. Fung, A numerical study of the regions of validity of the Kirchhoff and small-perturbation rough surface scattering models, *Radio Science*, *23*, 163–170, 1988.

England, A. W., The fractal dimension of diverse topographies and the effect of spatial windowing, in *Geol. Soc. of Canada Paper 90-4: Ground Penetrating Radar*, ed. J. A. Pilon, 57–61, 1992.

Evans, D. L., T. G. Farr, J. J. van Zyl, and H. A. Zebker, Radar Polarimetry: Analysis Tools and Applications, *IEEE Trans. Geosci. Remote Sensing*, *26*, 774–789, 1988.

Gaddis, L., P. Mouginis-Mark, R. Singer, and V. Kaupp, Geologic analyses of Shuttle Imaging Radar (SIR-B) data of Kilauea Volcano, Hawaii, *Geol. Soc. Am. Bull.*, *101*, 317–332, 1989.

Glicken, H., *Rockslide-debris avalanche of May 18, 1980, Mount St. Helens Volcano, Washington* (USGS Prof. Paper 1488), 304 pp., 7 plates, 1989.

Huang, J., and D. L. Turcotte, Fractal Mapping of Digitized Images: Application to the Topography of Arizona and Comparisons With Synthetic Images, *J. Geophys. Res.*, *94*, 7491–7495, 1989.

Huang, J., and D. L. Turcotte, Fractal image analysis: application to the topography of Oregon and synthetic images, *J. Opt. Soc. Am. A*, *7*, 1124–1130, 1990.

Mandelbrot, B. B., *The Fractal Geometry of Nature*, 468 pp., W. H. Freeman and Company, New York, 1983).

Sayles, R. S., and T. R. Thomas, Surface topography as a nonstationary random process, *Nature*, *271*, 431–434, 1978.

Thorsos, E. I., and D. R. Jackson, The validity of the perturbation approximation for rough surface scattering using a Gaussian roughness spectrum, *J. Acoust. Soc. Am.*, *86*, 261–277, 1989.

R. T. Austin and A. W. England, Radiation Laboratory, 3228 EECS Bldg., University of Michigan, Ann Arbor, MI 48019-2122.

(Received February 11, 1993;
revised May 14, 1993;
accepted June 3, 1993.)

IV Estimation of Power-Law Spectra

Having measured topography at scales from millimeters to 32 meters on several volcanic flows, our next task was to estimate the roughness spectra of these topographies. We immediately found that simple Fourier-based estimators, like the periodogram, produced greatly distorted spectra. The low frequency leakage of a power-law surface produced an artificial β in equation (1) that tended to lay near 2. Many of the early papers on the spectra of natural surfaces [e.g., 1] have suggested that the β for natural surfaces always lay near 2. We believe that this conclusion may have been the result of the leakage phenomenon that we observed. In fact, while the Mount St. Helens debris flows obeyed a power-lay, their β always lay between 2.31 and 2.51 – which are significantly different from 2. An artificial surface produced with a β of 2 would appear too rough at the higher spatial frequencies when compared to the Mount St. Helen surface profiles.

We presented these findings at the Lunar Science Conference [67] and published the results in the Transactions of Geoscience and Remote Sensing [3]. The TGARS paper is included on the following 12 pages.

Special Problems in the Estimation of Power-Law Spectra as Applied to Topographical Modeling

Richard T. Austin, *Student Member, IEEE*, Anthony W. England, *Senior Member, IEEE*, and Gregory H. Wakefield, *Member, IEEE*

Abstract—**An increasing number of topographical studies find that natural surfaces possess power-law roughness spectra. Power-law spectra introduce unique difficulties in the spectral estimation process. We describe how an improper window choice allows leakage that yields a spectral estimate that is insensitive to the spectral slope. In addition, the commonly used Fourier-based spectral estimates have higher variances than other available estimators. Higher variance is particularly problematic when data records are short, as is often the case in remote-sensing studies. We show that Capon's spectral estimator has less variance than Fourier-based estimators and measures the spectral slope more accurately. We also show how estimates of a 2-D roughness spectrum can be obtained from estimates of the 1-D spectrum for the isotropic power-law case.**

I. Introduction

SPECTRAL analysis is a tool of increasing importance in the characterization of natural surfaces. One- and two-dimensional spectral estimates are useful because they allow surface structure to be interpreted as a sum of sinusoidal components with differing wavelengths. A number of studies have found that spectra computed from one-dimensional surface profiles may be reasonably modeled using a power-law spectrum of the form

$$S_Z(f) = c|f|^{-\beta} \tag{1}$$

over some range of spatial frequencies. $S_Z(f)$ is the power spectral density of the surface height random process; it has units of meters^2/meters^{-1} or meters^2 per unit spatial frequency. The spectral exponent β indicates the relative contribution of different wavelength components. Higher values of β indicate that the surface roughness is mostly due to low-frequency components, while lower values denote significant high-frequency contributions. β is also known as the spectral slope; a power-law spectrum is linear with slope $-\beta$ when plotted on a log–log scale. The roughness amplitude c is a multiplicative factor scaling the roughness at all spatial frequencies. Applications of power-law spectra include studies of regional topography [1]–[5], rock surfaces [6], seafloor morphology [7]–[11], and other surfaces [12], [13].

Rough surfaces that have structure over a wide range of spatial scales may also be described using the concepts of fractal geometry introduced by Mandelbrot [14]. Fractal objects are continuous but not differentiable; the fractal dimension D_f is a real-valued measure of how a line (surface) fills a plane (space). For a one-dimensional (1-D) surface profile, D_f takes on values between 1.0 (smooth and differentiable) and 2.0 (plane-filling). Two-dimensional (2-D) surfaces have D_f between 2.0 and 3.0. Adler [15] shows that the surface profile created by the intersection of a plane and a 2-D fractal surface is itself fractal with a fractal dimension equal to that of the 2-D surface decreased by one [2]. Random rough fractal surfaces have power-law spectra; Mandelbrot and Van Ness [16] and Voss [17] derive the relation between D_f and the spectral slope β of a 1-D profile of a rough fractal surface:

$$D_f = \frac{5 - \beta}{2}. \tag{2}$$

Thus, the spectral exponent satisfies $3 > \beta > 1$ for $1 < D_f < 2$.

Although synthetic topographies appear most realistic with $D_f \approx 2.2$ [14], [17], yielding linear profiles of $D_f \approx 1.2$ and $\beta \approx 2.6$, several studies [1], [4], [7], [8] have reported measured values of $\hat{\beta}$ (the hat denotes an estimate) near 2.0, leading some investigators to suggest that spectral slopes of 2.0 are characteristic of natural topography [1]. One explanation for the discrepancy between measured $\hat{\beta}$ and inferred values of β is that spectral analysis of nonstationary regions tends to result in $\hat{\beta}$ near 2.0 [9], [18]. We show in this paper that leakage in spectral estimators may also yield $\hat{\beta}$ that cluster near 2.0.

While leakage is a well-known problem of classical spectral estimators such as the periodogram, common Fourier-based spectral estimators also suffer from high variance. The usual remedy is to average spectral estimates derived from multiple data sets or multiple segments of a long data set. This is not always possible: in remote-sensing studies, surface profiles are often only one of many "ground-truth" parameters to be collected. As a result, investigators may be faced with the problem of estimating the surface spectrum using a limited data set.[1] In

Manuscript received May 29, 1993; revised March 18, 1994. This work was supported in part by the National Aeronautics and Space Administration under Grant NAGW-2199 and by a shared SIR-C project.

The authors are with the Department of Electrical Engineering and Computer Science, University of Michigan, Ann Arbor, MI 48109.

IEEE Log Number 9402672.

[1] In the case of 1-D surface profiles, we find that a typical record consists of at most 500 points; 2-D profiles are even shorter, rarely exceeding 50 × 50 points. Numbers of this magnitude are considered small from a statistical inference viewpoint, where samples of thousands or hundreds of thousands of points are more common.

this paper, we describe a spectral estimator that reduces the leakage problem and predicts c and β with reduced variance in the case of short data runs.

II. Spectral Estimates from Linear Profiles

Fourier-based spectral estimators (e.g., the periodogram) render an estimate of the power spectral density whose expectation or mean value is a convolution of the spectrum of the sampled profile and the Fourier transform of a window function introduced by the finite extent of the sample profile. Various window functions are used; common windows include rectangular, triangular, and Hanning windows. The selection of a particular window is based on a trade-off between spectral resolution and spectral leakage.

Spectral leakage refers to the inaccuracy of a spectral estimate at a given frequency due to convolution with the transformed window; i.e., spectral power "leaks" from nearby frequencies according to the shape of the transformed window. We show spectral domain window functions corresponding to a periodogram and a modified periodogram with Hanning window in Fig. 1. At each point or frequency at which the spectrum is to be estimated, the true spectrum (the dashed line in Fig. 1) is weighted by the window function centered on that frequency and then averaged over frequency. Contributions from frequencies other than the frequency of interest constitute spectral leakage. We can reduce spectral leakage by choosing an estimator whose window has sidelobes that decay quickly (such as W_H in Fig. 1), but such a window will have a broader main lobe, decreasing the spectral resolution. (See [19] for a discussion.) In the power-law case, leakage from the large peak at low spatial frequencies affects the estimate at upper spatial frequencies (making the slope shallower) unless a window function with very low sidelobe levels is selected. We now show this result for the case of 1-D spectral estimates based on 1-D surface profiles.

Spectral estimates derived from sampled data suffer from *aliasing* if the sampled process has spectral components at frequencies greater than the Nyquist frequency f_c,

$$f_c = \frac{1}{2\Delta} \tag{3}$$

where Δ is the sampling interval. In the sections that follow, we will assume that aliasing is not present. Simulated data sets will be bandlimited to prevent aliasing. Modifications due to aliasing will be presented in a later section.

A. Fourier-Based Estimators

Consider a one-dimensional surface $Z(x)$, where Z, the surface height, is a single-valued function (i.e., there are no overhangs). Suppose that the surface height has been measured at N locations x_i ($i = 0, \cdots, N-1$), which

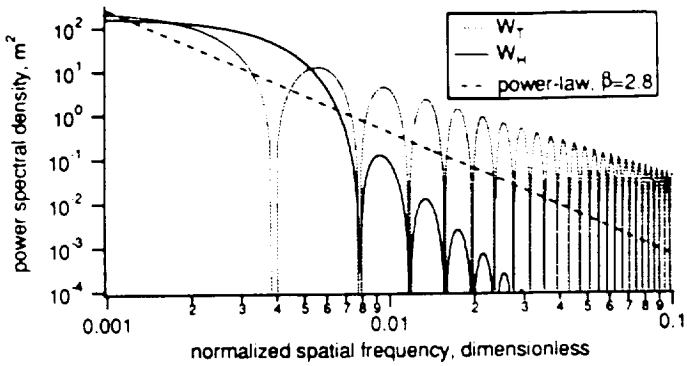

Fig. 1. Spectral domain window functions W_T (10) for the periodogram and W_H (13) for the modified periodogram with Hanning window, both with $N = 256$. The convolution of the window function with the true spectrum (e.g., the power-law spectrum shown as the dashed line) may result in a spectral bias (an inaccuracy in the mean value of the estimate).

are spaced at intervals Δ. The periodogram spectral estimator $\hat{P}_{\text{PER}}(f_\Delta)$ for the sampled surface height is given by Kay [20]:

$$\hat{P}_{\text{PER}}(f_\Delta) = \frac{1}{N}\left|\sum_{n=0}^{N-1} Z[x_n] \exp(-j2\pi f_\Delta n)\right|^2. \tag{4}$$

The frequency is written f_Δ as a reminder that (4) is given in terms of a normalized frequency f_Δ, where

$$f_\Delta = f\Delta \tag{5}$$

and f_Δ satisfies $-\frac{1}{2} \le f_\Delta \le \frac{1}{2}$. (Most spectral estimation texts use normalized frequency; we will follow this convention until a later section when we compare spectra obtained from sampled profiles with differing Δ.)

While the periodogram may be evaluated for any $|f_\Delta|$ less than $\frac{1}{2}$ (the normalized Nyquist frequency), it is often calculated using a fast Fourier transform (FFT) and consequently is evaluated only at discrete frequencies $f_{\Delta i} = i/N$, where $i = -N/2, \cdots, -1, 0, 1, \cdots, N/2$. To evaluate the periodogram using an FFT at additional frequencies, we can "zero-pad" the original data series to length M by adding $M - N$ zeros to the end. The periodogram will then be evaluated at frequencies $f_{\Delta i} = i/M$. Most FFT algorithms require that N be an integer power of two. Series for which N is not an integer power of two must be zero-padded up to the next higher power of two.

The periodogram is an unreliable estimator of the power spectral density because it has a variance that is equal to the square of its expected value, *independent of* N [20]. The usual practice in the field of spectral estimation is to average multiple periodograms to reduce the variance, but this may not be possible if the quantity of data is limited.[2] We show later in this section that $\hat{P}_{\text{PER}}$ is a poor estimator in the power-law case even if the variance problem were absent.

[2]For example, suppose the data record is 1000 points long. To reduce the variance by a factor of eight, we can divide the data record into eight segments of length 125, calculate eight spectral estimates, and average the results. The bias of the estimate will be increased (due to the broader main and side lobes of the window), and the reduction in variance may be less than eightfold if the segments are not uncorrelated. If the entire data record has only 125 points, this procedure is not useful.

A modified periodogram $\hat{P}_{HAN}(f_\Delta)$ may be obtained by multiplying the data series by a Hanning window before calculating the spectral estimate:

$$\hat{P}_{HAN}(f_\Delta) = \frac{1}{NU}\left|\sum_{n=0}^{N-1} Z[x_n]\, w_H[n] \exp(-j2\pi f_\Delta n)\right|^2 \quad (6)$$

where the Hanning window

$$w_H[n] = \frac{1}{2}\left[1 - \cos\left(\frac{2\pi n}{N-1}\right)\right] \quad (7)$$

replaces the rectangular window ($w_R[n] = 1$) implicit in (4), and an extra normalization factor is introduced:

$$U = \frac{1}{N}\sum_{n=0}^{N-1} w_H^2[n]. \quad (8)$$

(Equation (6) follows the formulation of Welch [21] using a single data segment.) The transform of the Hanning window $w_H[n]$ has sidelobes that are lower and a main lobe that is roughly twice as wide as that of the transform of a rectangular window $w_R[n]$ of the same width. Convolution with a transformed Hanning window results in less leakage from low spatial frequencies (because the sidelobes are smaller) at the cost of decreased spectral resolution (smoothing due to the wider main lobe). We must consider the smoothness of the spectrum and how quickly it rolls off and then decide whether the leakage reduction is worth the loss in resolution. In the power-law case, reducing the leakage seems more important.

We now examine the expected values of these two estimators for a power-law surface spectrum. The expectation of the periodogram is given by [20]

$$E[\hat{P}_{PER}(f_\Delta)] = \int_{-1/2}^{1/2} W_T(f_\Delta - \xi)\, S_{Z\Delta}(\xi)\, d\xi \quad (9)$$

where $W_T(f_\Delta)$ is the transform of a triangular window:

$$W_T(f_\Delta) = \frac{1}{N}\left(\frac{\sin \pi f_\Delta N}{\sin \pi f_\Delta}\right)^2 \quad (10)$$

and $S_{Z\Delta}(f_\Delta)$ is the normalized form of the true power spectral density of $Z(x)$ chosen such that $\int S_{Z\Delta}(f_\Delta)\, df_\Delta = \int S_Z(f)\, df$:

$$\begin{aligned} S_{Z\Delta}(f\Delta) &= \frac{1}{\Delta} S_Z(f) \\ &= \frac{1}{\Delta} c f^{-\beta} \\ &= \Delta^{\beta-1} c (f\Delta)^{-\beta} \\ S_{Z\Delta}(f_\Delta) &= c_\Delta f_\Delta^{-\beta}. \end{aligned} \quad (11)$$

The expected value of the modified periodogram estimator $\hat{P}_{HAN}$ has a form similar to (9) [23, p. 553]:

$$E[\hat{P}_{HAN}(f_\Delta)] = \int_{-1/2}^{1/2} W_H(f_\Delta - \xi)\, S_{Z\Delta}(\xi)\, d\xi \quad (12)$$

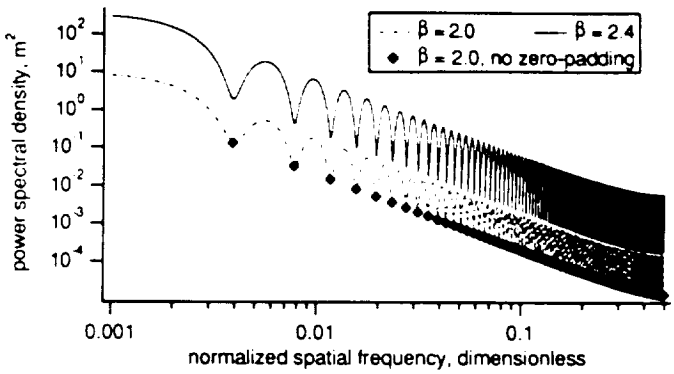

Fig. 2. Expected value of the periodogram spectral estimator for power-law surfaces with $\beta = 2.0$ and 2.4 and $c_\Delta = 1.0 \times 10^{-4}$. The estimates are based on 256-point profiles that were zero-padded to 16 384 points so that the periodogram would be evaluated at many frequencies. Solid dots indicate the expected values of the periodogram when evaluated without zero-padding.

where

$$W_H(f_\Delta) = \frac{1}{4NU}\left(b_1 + \frac{1}{2}b_2 + \frac{1}{2}b_3\right)^2 \quad (13)$$

$$b_1 = \frac{\sin(\pi f_\Delta N)}{\sin(\pi f_\Delta)} \quad (14)$$

$$b_2 = \frac{\sin\left\{\pi\left[f_\Delta - \frac{1}{N-1}\right]N\right\}}{\sin\left\{\pi\left[f_\Delta - \frac{1}{N-1}\right]\right\}} \quad (15)$$

$$b_3 = \frac{\sin\left\{\pi\left[f_\Delta + \frac{1}{N-1}\right]N\right\}}{\sin\left\{\pi\left[f_\Delta + \frac{1}{N-1}\right]\right\}} \quad (16)$$

and U is given by (8).

To show the performance of these Fourier-based estimators, we calculate their expected values using (9) and (12). We avoid the singularity at the low end of a pure power-law spectrum by modeling the exact surface spectrum as a Rayleigh function at low spatial frequencies:

$$S_{Z\Delta}(f_\Delta) = \begin{cases} (\alpha/\sigma^2)|f_\Delta| \exp(-f_\Delta^2/[2\sigma^2]), \\ \qquad |f_\Delta| \le 0.0001 \\ c_\Delta |f_\Delta|^{-\beta} \\ \qquad 0.0001 \le |f_\Delta| \le \frac{1}{2} \\ 0, \quad |f_\Delta| > \frac{1}{2} \end{cases} \quad (17)$$

where the parameters α and σ are chosen by enforcing the continuity of $S_{Z\Delta}$ and its first derivative at $|f_\Delta| = 0.0001$.

Fig. 2 shows the expected value of the periodogram spectral estimator calculated from theoretical spectra with spectral exponents of 2.0 and 2.4. The oscillatory behavior is due to the sidelobes of $W_T(f_\Delta)$. These oscillations are not visible if the periodogram is evaluated only at frequencies $f_i = i/N$ (i.e., without zero-padding) as indicated

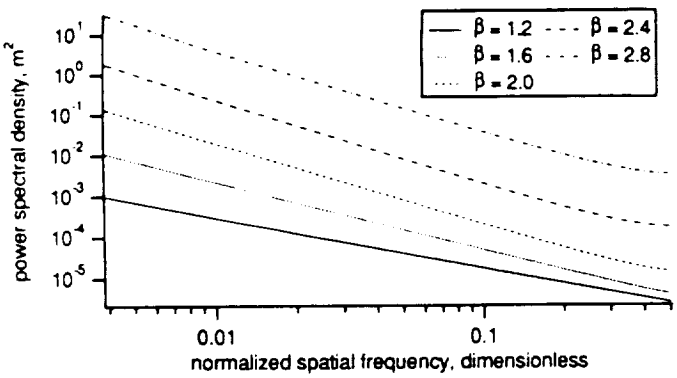

Fig. 3. Expected value of $\hat{P}_{PER}$ for five 256-point power-law profiles evaluated at frequencies corresponding to the case of no zero-padding.

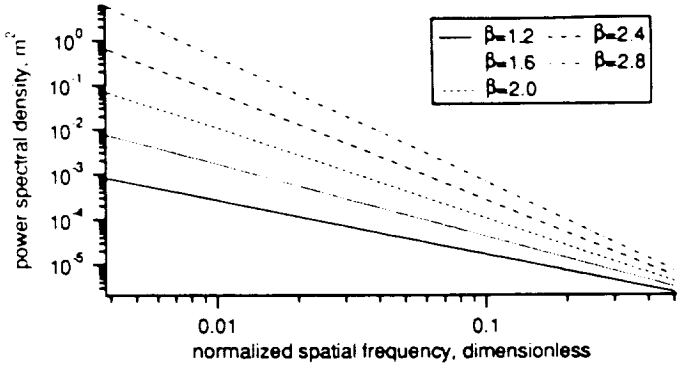

Fig. 4. Exact values of the power-law spectra used in calculations of the expected values of the spectral estimates.

in the figure. Since it is difficult to fit power-law functions to such oscillatory estimates, we sampled the expectations of periodograms of surfaces with five different spectral exponents at frequencies corresponding to the case of no zero-padding (Figure 3).[3] These curves may be compared to the exact spectra in Figure 4.[4] While the exact spectra vary in slope, the periodogram estimates are insensitive to the slope for several values of β. Fitting power-law functions to the linear portions of these estimate expectations ($f_\Delta < 0.2$), we see (Table I) that the estimated spectral exponent $\hat{\beta}$ clusters near 2.0 for $2 < \beta < 3$.[5] These values of β correspond to fractal dimensions that are typical for natural terrains (1.0–1.5 for profiles, 2.0–2.5 for surfaces).

Slope insensitivity is not a problem with $\hat{P}_{HAN}(f_\Delta)$, whose expected value is shown for various β in Fig. 5. The expected values of these estimates closely approximate the exact values for frequencies at which the main lobe and first two sidelobes do not overlap the low-frequency peak ($f_\Delta > 0.015625$). (Power-law fits to the upper regions of these estimates are listed in Table I). While $\hat{P}_{HAN}$ has a mean value that closely approximates the exact spectrum, this estimator suffers from a deficiency that is common to Fourier-based estimators: undesirably high variance. We examine the variance of $\hat{P}_{HAN}(f_\Delta)$ in a later section.[6]

TABLE I
POWER-LAW PARAMETERS DERIVED FROM FITS TO THE EXPECTATIONS OF PERIODOGRAM ($1/N \le f_\Delta < 0.2$), MODIFIED PERIODOGRAM ($4/N < f_\Delta \le 0.5$), PREWHITENED ($1/N < f_\Delta < 0.2$), AND CAPON'S ($1/(2p) \le f_\Delta \le 0.5$) ESTIMATORS

Theoretical	$E[\hat{P}_{PER}]$	$E[\hat{P}_{HAN}]$	$E[\hat{P}_{PW}]$	$E[\hat{P}_{CAP}]$
$c_\Delta = 1.0 \cdot 10^{-6}$	$c_\Delta = 9.71 \cdot 10^{-7}$	$c_\Delta = 9.99 \cdot 10^{-7}$	$c_\Delta = 8.42 \cdot 10^{-7}$	$c_\Delta = 1.01 \cdot 10^{-6}$
$\beta = 1.2$	$\hat{\beta} = 1.231$	$\hat{\beta} = 1.201$	$\hat{\beta} = 1.255$	$\hat{\beta} = 1.198$
$c_\Delta = 1.0 \cdot 10^{-6}$	$c_\Delta = 1.04 \cdot 10^{-6}$	$c_\Delta = 9.99 \cdot 10^{-7}$	$c_\Delta = 8.63 \cdot 10^{-7}$	$c_\Delta = 1.01 \cdot 10^{-6}$
$\beta = 1.6$	$\hat{\beta} = 1.656$	$\hat{\beta} = 1.601$	$\hat{\beta} = 1.643$	$\hat{\beta} = 1.598$
$c_\Delta = 1.0 \cdot 10^{-6}$	$c_\Delta = 2.10 \cdot 10^{-6}$	$c_\Delta = 9.96 \cdot 10^{-7}$	$c_\Delta = 8.66 \cdot 10^{-7}$	$c_\Delta = 1.02 \cdot 10^{-6}$
$\beta = 2.0$	$\hat{\beta} = 1.982$	$\hat{\beta} = 2.001$	$\hat{\beta} = 2.042$	$\hat{\beta} = 1.998$
$c_\Delta = 1.0 \cdot 10^{-6}$	$c_\Delta = 1.87 \cdot 10^{-6}$	$c_\Delta = 9.98 \cdot 10^{-7}$	$c_\Delta = 8.65 \cdot 10^{-7}$	$c_\Delta = 1.02 \cdot 10^{-6}$
$\beta = 2.4$	$\hat{\beta} = 2.032$	$\hat{\beta} = 2.402$	$\hat{\beta} = 2.443$	$\hat{\beta} = 2.397$
$c_\Delta = 1.0 \cdot 10^{-6}$	$c_\Delta = 3.83 \cdot 10^{-4}$	$c_\Delta = 9.96 \cdot 10^{-7}$	$c_\Delta = 8.43 \cdot 10^{-7}$	$c_\Delta = 1.02 \cdot 10^{-6}$
$\beta = 2.8$	$\hat{\beta} = 1.986$	$\hat{\beta} = 2.804$	$\hat{\beta} = 2.859$	$\hat{\beta} = 2.796$

B. Prewhitening

The periodogram (Fig. 2) and, to a lesser degree, the modified periodogram (Fig. 5) suffer from spectral leakage in the power-law case, especially for spectra with $2 \le \beta \le 3$. Fox and Hayes [9] and Gilbert and Malinverno [10] avoid the leakage problem by using prewhitening procedures in which they modify the surface height

[3]We emphasize that Fig. 3 shows *expected values*, $E[\hat{P}_{PER}(f)]$, (i.e., mean values) of the periodogram estimator, calculated using (9) at frequencies corresponding to the case of no zero-padding for random profiles $Z(x)$ having power-law spectra given by (17) with five different values of β. Plots of the estimator $\hat{P}_{PER}$ itself would show wide variance and departures from linearity (similar to the estimates shown in Fig. 8) and would vary for different realizations of the random process, i.e., for different samples of a given surface.

The expected values of the estimator appear linear at the low-frequency end because we have assumed in (17) that the true surface spectrum is power-law (with linear slope) down to a frequency of $f_\Delta = 0.0001$—a frequency too low to be accurately measured by the sampled profile segment. We used this assumption because surface profiles are often too short to show very long wavelength roughness components. (This was certainly true for our field work.)

[4]The expected values of the periodogram estimator in Fig. 3 have a higher total energy level than the corresponding exact spectra in Fig. 4 due to the spectral leakage that is also responsible for the slope insensitivity. Remember that $E[\hat{P}_{PER}]$ is the convolution of the true spectrum $S_{Z\Delta}$ with the transform of a window function introduced by the finite surface sample [W_T in (9)]. If the estimator were perfect, W_T would be a delta function, and the estimate at frequency f would reflect only power in the true spectrum at that frequency. In the periodogram case, however, W_T is given by (10) (a sinc^2 function), so power from many frequencies above and below f affect $\hat{P}_{PER}(f)$. Leakage from lower frequencies is particularly significant in the power-law case.

[5]For a given single periodogram, $\hat{\beta}$ may indeed take values between 2.0 and 3.0, due to the variance of the periodogram. Long data records do not reduce this variance; the variance is independent of N (see [20, p. 422]). One may reduce the variance by segmenting the long data record as described previously, but this process will lead to the expected values shown in Fig. 3. Sampling $\hat{P}_{PER}$ at frequencies other than $f_{\Delta_i} = i/N$ could lead to a variety of incorrect slopes, as can be seen in Fig. 2.

[6]We have also examined the Blackman–Tukey spectral estimator $\hat{P}_{BT}$, as described in Blackman and Tukey [22]. For processes other than white noise, the BT estimator decreases variance but increases bias as compared to the periodogram (Kay [20, p. 80]). We did not include $\hat{P}_{BT}$ in our comparison because it is even more susceptible to spectral leakage (and therefore, slope insensitivity) than $\hat{P}_{PER}$. The expected value of $\hat{P}_{BT}$ is equal to the expected value of $\hat{P}_{PER}$ convolved with another window, as derived in Kay [20, p. 98]:

$$E[\hat{P}_{BT}(f_\Delta)] = \int_{-1/2}^{1/2} W(f_\Delta - \xi) E[\hat{P}_{PER}(\xi)]\, d\xi.$$

Since the BT estimator has an expected value that is the result of the convolution of the true spectrum with *two* window functions, its value at a given frequency can be greatly corrupted by leakage from lower frequencies.

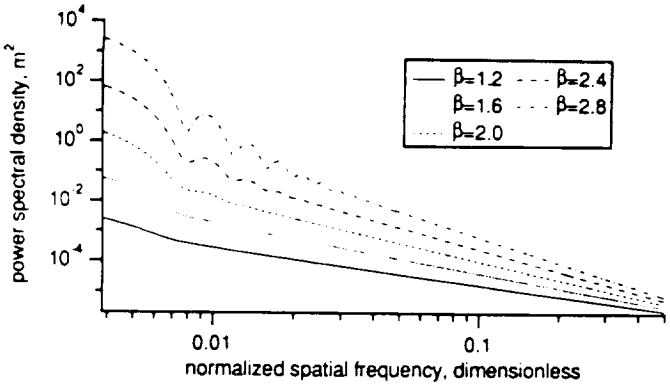

Fig. 5. Expected values of $\hat{P}_{HAN}(f_\Delta)$ for five different 256-point power-law profiles. The profiles were zero-padded to 16 384 points.

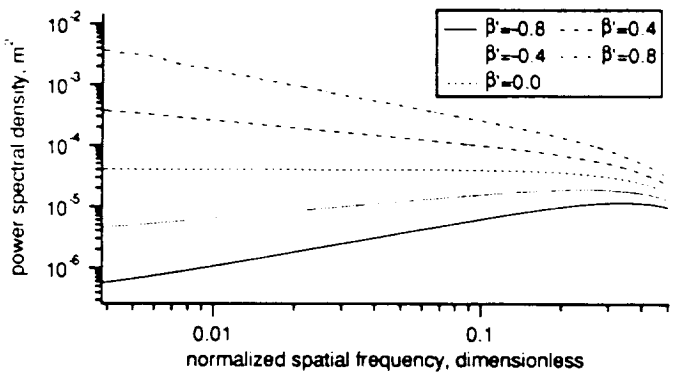

Fig. 6. Expected values of $\hat{P}_{PW}(f_\Delta)$ for five different 257-point power-law profiles. The profiles were zero-padded to 16 384 points.

data to have a relatively flat spectrum, perform spectral estimation, and then correct the estimate according to the original modification.

We will examine here the simplest prewhitening approach similar to that used by Gilbert and Malinverno. If the power spectral density of the surface height is defined as [24, p. 270]

$$S_Z(f) = \lim_{T\to\infty} \frac{1}{T} E\left[\left|\int_{-T/2}^{T/2} Z(x) \exp(-j2\pi fx)\, dx\right|^2\right] \tag{18}$$

then the derivative of the surface height $dZ(x)/dx$ will have a related spectrum:

$$\begin{aligned} S_{Z'}(f) &= \lim_{T\to\infty} \frac{1}{T} E\left[\left|\int_{-T/2}^{T/2} \frac{dZ(x)}{dx} \exp(-j2\pi fx)\, dx\right|^2\right] \\ &= \lim_{T\to\infty} \frac{1}{T} E\left[\left|j2\pi f \int_{-T/2}^{T/2} Z(x) \exp(-j2\pi fx)\, dx\right|^2\right] \\ &= 4\pi^2 f^2 S_Z(f) \\ &= 4\pi^2 c |f|^{-\beta+2} \\ S_{Z'}(f) &= c' |f|^{-\beta'} \end{aligned} \tag{19}$$

and we see that the spectral exponent β' of the derivative process takes on values between -1 and 1 for $1 < \beta < 3$. The spectrum of the derivative process is more nearly flat (it is white noise for $\beta' = 0$). Since there is no pronounced peak at low frequencies, spectral leakage is less of a problem.

Gilbert and Malinverno approximate the derivative by taking first differences of the sampled data: $Z'[x_i] \approx Z[x_{i+1}] - Z[x_i]$. They then apply a Hanning window and use a periodogram to obtain a spectral estimate of $S_{Z'\Delta}(f_\Delta)$. After averaging multiple periodograms, an estimate of the spectral exponent $\hat{\beta}$ is obtained from an estimate of $\hat{\beta}'$:

$$\hat{\beta} = \hat{\beta}' + 2. \tag{20}$$

We now examine this procedure for the limited data case in which multiple periodograms are not available for averaging. We omit the Hanning window for simplicity.

We define a prewhitened spectral estimate $\hat{P}_{PW}(f_\Delta)$ in terms of the first differences of the sampled data:

$$\hat{P}_{PW}(f_\Delta) = \frac{1}{N}\left|\sum_{n=0}^{N-1} \{Z[x_{n+1}] - Z[x_n]\} \exp(-j2\pi f_\Delta n)\right|^2. \tag{21}$$

The expected value of the prewhitened estimator may be derived by a procedure similar to the derivation of (9):

$$E[\hat{P}_{PW}(f_\Delta)] = 2\int_{-1/2}^{1/2} W_T(f_\Delta - \xi) S_{Z\Delta}(\xi) \cdot [1 - \cos(2\pi\xi)]\, d\xi. \tag{22}$$

Using (22) and the modified power-law spectrum defined in (17), the expected values of the prewhitened estimator are calculated and are shown in Fig. 6. These estimates are based on 257-point profiles.

Power-law functions were fit to the linear portions of these estimate expectations ($f_\Delta < 0.2$), and the parameters $\hat{c}'$ and $\hat{\beta}'$ were converted to $\hat{c}$ and $\hat{\beta}$ using (20) and $\hat{c} = \hat{c}'/(4\pi^2)$. The results, given in Table I, show that the expected value of the spectral slope is fairly accurate because the spectral leakage has been largely eliminated. A Hanning window may still be useful in practice (since we do not know *a priori* that a spectrum is power law), but we see that leakage is not a problem for the prewhitened estimator in the power-law case. The variance of $\hat{P}_{PW}(f_\Delta)$ will be examined in a later section.

C. Capon's Estimator

An alternative procedure that is more direct than the prewhitened periodogram is the use of Capon's estimator [25] (the so-called "minimum variance spectral estimator") described in Kay [20, chap. 11]. This estimator was developed originally for geological signal processing problems in which the number of sensors (and therefore the number of spatial samples) were extremely limited and posed restrictions on what could be inferred from standard spectral analysis. Capon's estimator essentially customizes a filter at each frequency of interest to minimize the total power output, subject to the constraint that the gain at the frequency of interest is unity. Therefore, the filter

may be asymmetric in sidelobe level according to the shape of the signal spectrum; in the power-law case, the sidelobes are adjusted to reduce the leakage from low-frequency components.

Capon's estimator $\hat{P}_{CAP}(f_\Delta)$ is obtained by first calculating an estimate of the autocorrelation matrix $\mathbf{R}_{ZZ}$, whose elements are defined as

$$[\mathbf{R}_{ZZ}]_{ij} = E[Z^*[n]Z[n + i - j]]. \tag{23}$$

We can estimate the elements of the autocorrelation matrix using the modified covariance method, described in [20]:

$$[\hat{\mathbf{R}}_{ZZ}]_{ij} = \frac{1}{2(N-p)}\left[\sum_{n=p}^{N-1} Z[n-i]Z[n-j] + \sum_{n=0}^{N-1-p} Z[n+i]Z[n+j]\right]. \tag{24}$$

Capon's estimator is then given by

$$\hat{P}_{CAP}(f_\Delta) = \frac{p}{\mathbf{e}^H \hat{\mathbf{R}}_{ZZ}^{-1}\mathbf{e}} \tag{25}$$

where p is the dimension of the autocorrelation matrix and

$$\mathbf{e} = [1 \quad e^{j2\pi f_\Delta} \quad e^{j4\pi f_\Delta} \quad \cdots \quad e^{j2\pi(p-1)f_\Delta}]^T. \tag{26}$$

Since (24) is an unbiased[7] and consistent estimator of the covariance matrix, we can evaluate the expected value of Capon's estimator by substituting the exact covariance matrix (obtained from the exact theoretical spectrum) into (25). This procedure was used to calculate the expected values of $\hat{P}_{CAP}(f_\Delta)$ for five values of β using a covariance matrix of dimension $p = 70$. The expected values of these estimates (Fig. 7) have good agreement with the exact spectra over a wide range of spectral slopes. Parameters of power-law functions fit to the expected values of $\hat{P}_{CAP}(f_\Delta)$ for $f_\Delta \geq 1/(2p)$ are compared with the exact spectral parameters in Table I.

The bias of Capon's estimator is independent of N because (24) is an unbiased estimator of $\hat{\mathbf{R}}_{ZZ}$. However, the bias does depend on p ($p\Delta$ is the longest lag for which the covariance is estimated). For a given data set, an increase in p will result in reduced bias at the cost of increased variance. Thus, N indirectly influences the bias because the range of p is constrained by N. We generally found $p \approx 0.3N$ to be a good compromise between variance and bias.

In the power-law case, the bias of Capon's estimator was found to increase noticeably for spatial frequencies corresponding to wavelengths much longer than $p\Delta$. We therefore discard calculated values of $\hat{P}_{CAP}(f_\Delta)$ for spatial frequencies below $1/(2p)$.

[7]Equation (24) is approximately but not strictly unbiased because all lags are not weighted equally and overlapping lags are used. A variety of covariance estimators have been examined, and (24) was found to be the preferred estimator for short data records. See Kay [20] or other texts for more information.

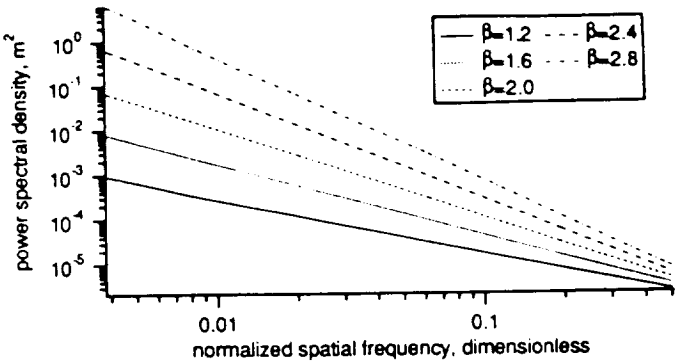

Fig. 7. Expected values of $\hat{P}_{CAP}(f_\Delta)$ for synthetic profiles with various β using an autocorrelation matrix of dimension $p = 70$. Estimates are evaluated at the same 16 384 frequencies used in Figs. 2, 5, and 6.

D. Variance Comparison

Capon's estimator, the modified periodogram with Hanning window, and the prewhitened periodogram all produce parameter estimates whose expected values closely approximate the exact values for a power-law spectrum. We now compare the estimators in terms of variance. The exact expression for the variance of the modified periodogram involves higher order moments and is usually evaluated only for a Gaussian white-noise case [21]. The statistical properties of Capon's estimator for time series data are not known [20], although some results have been derived for array data. To avoid these problems and test these estimators under actual-use conditions, we generated short synthetic topographic profiles of known statistics using a spectral synthesis algorithm. We then compare parameters obtained from Capon's, the modified periodogram, and the prewhitened periodogram estimates with those of the spectra used to create the profiles.

Our spectral synthesis algorithm closely follows [26] and consists of the following steps. 1) Generate a set of discrete Fourier amplitudes that, when squared and multiplied by $1/N$, satisfy the desired power law. While [26] used a pure power-law spectrum, we use the modified spectrum (17) to assure a zero-mean surface height. 2) Multiply the amplitudes by a Gaussian random variable such that the mean value of the amplitude satisfies the power law. 3) Generate a set of complex discrete Fourier coefficients (i.e., the FFT of a real surface) using the randomized amplitudes and a uniformly distributed random phase, enforcing symmetry conditions such that the inverse FFT will be real-valued. 4) Calculate the inverse FFT of the coefficients, resulting in a synthetic surface profile.

Using this algorithm, we generated 10 synthetic 64-point surface profiles with $\beta = 2.4$ and c_Δ, α, and σ chosen as before. We then calculated 1) Capon's estimates using a covariance matrix of dimension $p = 20$, 2) modified periodogram estimates using a full-width Hanning window, and 3) periodogram estimates based on the first differences of the surface profiles. We see in Fig. 8 that the modified periodogram and prewhitened periodogram estimates have noticeably greater variance.

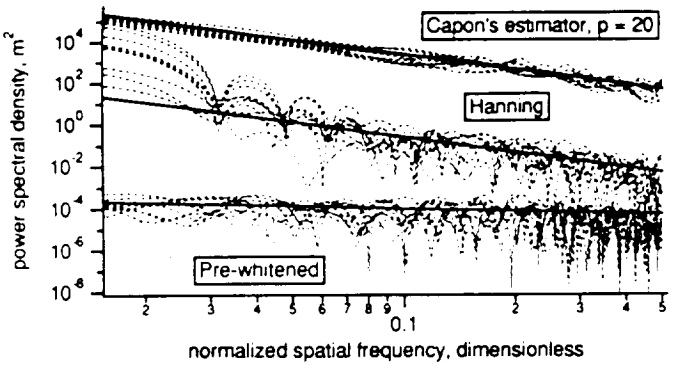

Fig. 8. Capon's, modified periodogram, and prewhitened periodogram spectral estimates for 10 different power-law profiles. The profiles were 64 points long. The modified periodogram and Capon's estimates have been offset for clarity. The solid lines represent the exact spectrum.

TABLE II
SPECTRAL STATISTICS DERIVED FROM FITS TO MODIFIED PERIODOGRAMS, PERIODOGRAMS BASED ON PREWHITENED DATA, AND CAPON'S ESTIMATORS OF TEN SYNTHETIC 64-POINT PROFILES WITH $c_\Delta = 1.0 \cdot 10^{-6}$ AND $\beta = 2.4$

Estimator	mean $\hat{c}_\Delta$	std. dev. $\hat{c}_\Delta$	mean $\hat{\beta}$	std. dev. $\hat{\beta}$
$\hat{P}_{HAN}$	$0.724 \cdot 10^{-6}$	$0.819 \cdot 10^{-6}$	2.767	0.631
$\hat{P}_{PW}$	$1.310 \cdot 10^{-6}$	$1.690 \cdot 10^{-6}$	2.469	0.567
$\hat{P}_{CAP}$	$0.891 \cdot 10^{-6}$	$0.433 \cdot 10^{-6}$	2.371	0.313

Estimation of power-law parameters from the spectral estimates is an independent problem. In this analysis, we estimate c and β by performing a minimum absolute deviation fit of a power-law function to the estimated values of the power density spectrum. The minimum absolute deviation fit, which is performed in log–log space, is more robust than a least-squares fit. To make the power-law fit independent of the frequency sampling of the spectral estimates, we evaluated the estimates at frequencies spaced very closely together so that the estimator would be a smooth curve between the sampled points. While it may be possible to design a parameter estimate based on fewer samples of the spectral estimate, such a method would require additional assumptions in the spectral model which are outside the scope of this study.

Values of the spectral estimates outside their regions of high accuracy ($4/N < f_\Delta \le 0.5$ for $\hat{P}_{HAN}$, $1/N < f_\Delta < 0.2$ for $\hat{P}_{PW}$, and $1/(2p) \le f_\Delta \le 0.5$ for $\hat{P}_{CAP}$) were discarded as before. The mean and standard deviation of the estimated roughness amplitude $\hat{c}_\Delta$ and spectral slope $\hat{\beta}$ are given in Table II. We see that the spectral parameters predicted using Capon's estimator have roughly half the variance of estimates derived from either the modified periodogram with the Hanning window or the periodogram based on prewhitened data. We therefore select Capon's estimator as the preferred estimation algorithm for use with short data records in the power-law spectrum case.

E. Formulas for Real Frequency

Expressions for the spectral estimators listed in the preceding sections were given as functions of the normalized frequency f_Δ that is dependent on the sampling interval of a measured surface profile. In remote sensing studies, estimates of the surface spectrum in terms of real spatial frequency f (in meters^{-1}) are necessary so that 1) surface features may be compared to the electromagnetic wavelength and 2) spectral estimates derived from profiles with different sampling intervals Δ may be compared or combined into a composite spectrum.

The following expressions correspond to (4), (9), (10), (6), (12), (13), (14), (15), (16), (21), (22), (25), and (26), respectively, for the case of real (nonnormalized) frequency f, where f satisfies $-1/(2\Delta) \le f \le 1/(2\Delta)$:

$$\hat{P}_{PER}(f) = \frac{\Delta}{N}\left|\sum_{n=0}^{N-1} Z[x_n]\exp(-j2\pi f\Delta n)\right|^2 \tag{27}$$

$$E[\hat{P}_{PER}(f)] = \Delta\int_{-1/2\Delta}^{1/2\Delta} W_T(f-\xi)S_Z(\xi)\,d\xi \tag{28}$$

$$W_T(f) = \frac{1}{N}\left(\frac{\sin\pi f\Delta N}{\sin\pi f\Delta}\right)^2 \tag{29}$$

$$\hat{P}_{HAN}(f) = \frac{\Delta}{NU}\left|\sum_{n=0}^{N-1} Z[x_n]w_H[n]\exp(-j2\pi f\Delta n)\right|^2 \tag{30}$$

$$E[\hat{P}_{HAN}(f)] = \Delta\int_{-1/2\Delta}^{1/2\Delta} W_H(f-\xi)S_Z(\xi)\,d\xi \tag{31}$$

$$W_H(f) = \frac{1}{4NU}\left(b_1 + \frac{1}{2}b_2 + \frac{1}{2}b_3\right)^2 \tag{32}$$

$$b_1 = \frac{\sin(\pi f\Delta N)}{\sin(\pi f\Delta)} \tag{33}$$

$$b_2 = \frac{\sin\left\{\pi\left[f - \frac{1}{(N-1)\Delta}\right]\Delta N\right\}}{\sin\left\{\pi\left[f - \frac{1}{(N-1)\Delta}\right]\Delta\right\}} \tag{34}$$

$$b_3 = \frac{\sin\left\{\pi\left[f + \frac{1}{(N-1)\Delta}\right]\Delta N\right\}}{\sin\left\{\pi\left[f + \frac{1}{(N-1)\Delta}\right]\Delta\right\}} \tag{35}$$

$$\hat{P}_{PW}(f) = \frac{\Delta}{N}\left|\sum_{n=0}^{N-1}\left\{\frac{Z[x_{n+1}] - Z[x_n]}{\Delta}\right\}\cdot\exp(-j2\pi f\Delta n)\right|^2 \tag{36}$$

$$E[\hat{P}_{PW}(f)] = 2\Delta\int_{-1/2\Delta}^{1/2\Delta} W_T(f-\xi)S_Z(\xi)\cdot[1-\cos(2\pi\xi)]\,d\xi \tag{37}$$

$$\hat{P}_{CAP}(f) = \frac{p\Delta}{\mathbf{e}^H\hat{\mathbf{R}}_{ZZ}^{-1}\mathbf{e}} \tag{38}$$

$$\mathbf{e} = [1 \quad e^{j2\pi f\Delta} \quad e^{j4\pi f\Delta} \quad \cdots \quad e^{j2\pi(p-1)f\Delta}]^T. \tag{39}$$

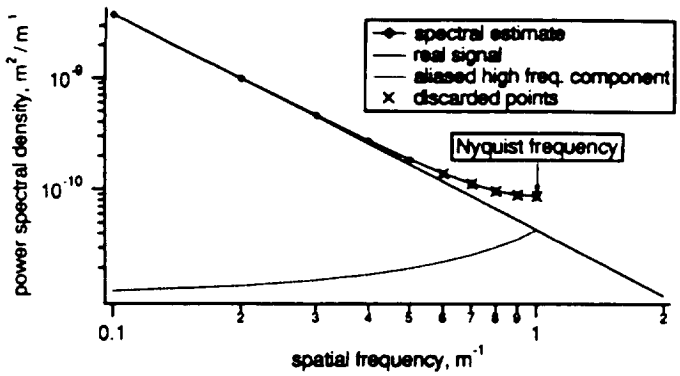

Fig. 9. Aliasing in the power-law spectrum case. Points marked (×) are discarded to reduce errors due to aliasing.

F. Aliasing

The estimates presented in the previous sections assumed that aliasing was not present, and the synthetic surface profiles were constructed to be bandlimited; i.e., they had no spatial frequency components above the Nyquist frequency $f_c = 1/(2\Delta)$. Real surfaces will generally have frequency components at spatial frequencies above f_c. As a result of a necessarily insufficient sampling rate, power at frequencies higher than f_c will be aliased into the range $-f_c \le f \le f_c$. We can derive an equation showing this result in terms of real frequency by extending the derivation of Oppenheim and Schafer [23, pp. 26–28], obtaining

$$S_{Z_{\text{aliased}}}(f) = \sum_{n=-\infty}^{\infty} S_Z\left(f + \frac{n}{\Delta}\right). \tag{40}$$

In the power-law case, the power spectral density falls off quickly with increasing frequency. The $n = 0$ (exact) and $n = 1$ (first alias) terms and their sum are plotted for a sample power-law case in Fig. 9. We see that the effects of aliasing are most significant at the high-frequency end of the spectral estimate. As a first-order correction to avoid the aliasing problem, we discard values of the spectral estimate computed for frequencies greater than $f_c/2$, as indicated in the figure.

G. Applicability to Real Data

Real geological data possess a variety of irregularities and surface statistics. Spectra of natural topography clearly cannot conform to a power-law model at all spatial frequencies—roughness features on the scale of millions of meters are unphysical, as are those at subatomic scales. However, in the studies cited in Section I as well as in our own investigations, measured spectra of topography are well modeled by a power-law spectrum in the form of (1) over some range of spatial frequencies. We have based our comparison of spectral estimators on an idealized spectrum with constant slope (except for the very-low-frequency roll-off introduced in (17) to avoid an unphysical singularity) in order to have an easy reference for comparison. Because both the Fourier estimators with windowing and Capon's estimator are local-neighborhood estimators, our comparison also illustrates the relative performance of these estimators for spectra that have variations in slope with frequency or local perturbations in level that violate monotonicity.

III. Estimation of Two-Dimensional Spectra

While the previous techniques allow the estimation of the spectrum of a linear profile, we would in general prefer a two-dimensional spectrum of surface topography. Such a spectrum might show hidden anisotropy or may indicate that the surface is isotropic in the statistical sense. In either case, the full 2-D spectrum provides valuable additional information.

Two-dimensional spectral analyses are precluded when 2-D data are not available. Spectral studies of seafloor morphology, for example, usually utilize profiles collected by bathymetric instruments that are towed by a ship, producing a seafloor profile along the ship's path. Some directional insight can be obtained by obtaining profiles in orthogonal directions.

On land, 2-D data are somewhat more accessible. Huang and Turcotte [1], [4] and England [5] use digital elevation models to estimate surface spectra, but their methods average over azimuth angle in the spectral domain. Two-dimensional data at scales of centimeters to tens of meters can be tedious and costly to obtain, necessitating smaller dimensions of a sampling grid, i.e., fewer than 100 × 100 measured points per 2-D profile.

A. Estimator Selection

Two-dimensional Fourier-based spectral estimators such as the 2-D periodogram suffer from the same problems as the corresponding 1-D estimators: leakage in the power-law case and high variance. A 2-D Capon's estimator is one solution to these problems. The 1-D Capon's estimator is readily extended to the two-dimensional case [20, sect. 15.8], at the cost of increased complexity. Inversion of the covariance matrix may become problematic because the matrix is now of dimensions $p^2 \times p^2$ rather than $p \times p$. For a similar level of resolution, the 2-D Capon's estimator will require a much greater volume of data (as will the other 2-D estimators). If such high quantities of data are not available, as is often the case for 2-D data sets, the variance of the Capon's estimate will be correspondingly higher.

B. Two-Dimensional Spectral Estimation of Isotropic Surfaces

If a surface area is known to have or can be assumed to have isotropic statistics (from knowledge of the origin of the surface, or perhaps from measured 1-D spectra in several directions), then an estimate of the 2-D roughness spectrum can be obtained from estimates of the 1-D spectrum. These 1-D spectral estimates may be obtained from individual rows of the 2-D surface height grid; we can calculate a spectral estimate for several or all rows and then average the estimates together. The resulting esti-

mate will have a variance that is much lower than that of a single row estimate in spite of the fact that the grid rows are not completely independent.

Suppose that an isotropic surface has a 2-D power spectral density $S_Z(f_x, f_y)$ that has the form of a power law down to some low spatial frequency f_{low} and some unspecified finite form below that:

$$S_Z(f_x, f_y) = S_Z(f_r) = \begin{cases} af_r^{-\gamma} & f_r \geq f_{low} \\ \text{finite} & f_r \leq f_{low} \end{cases} \quad (41)$$

where the radial spatial frequency $f_r = (f_x^2 + f_y^2)^{1/2}$. We now need to relate the parameters a and γ to the parameters of the 1-D spectrum of surface heights measured along a straight line on the same surface. This 1-D spectrum will also have the form of a power law for $f \geq f_{low}$ and can therefore be described by the parameters c and β.

To obtain this relation, we begin with the general expression for the Wiener–Khintchine relation in terms of the Fourier transform and write the correlation $E[Z(x, y)Z(x + \delta_x, y + \delta_y)]$ as $R_Z(\delta_x, \delta_y)$:

$$R_Z(\delta_x, \delta_y) = \int_{-\infty}^{\infty} \int_{-\infty}^{\infty} S_Z(f_x, f_y) \cdot \exp(j2\pi[f_x\delta_x + f_y\delta_y])\, df_x\, df_y. \quad (42)$$

Changing to radial coordinates ($\delta_x = \delta_r \cos\delta_\theta$, $\delta_y = \delta_r \sin\delta_\theta$) and noting that $S_Z(f_r, f_\theta)$ is independent of f_θ, we obtain

$$R_Z(\delta_r, \delta_\theta) = \int_0^{\infty} S_Z(f_r) f_r \int_0^{2\pi} \exp(j2\pi f_r \delta_r \cos\zeta)\, d\zeta\, df_r \quad (43)$$

where $\zeta = f_\theta - \delta_\theta$, leading to

$$R_Z(\delta_r) = 2\pi \int_0^{\infty} S_Z(f_r) J_0(2\pi f_r \delta_r) f_r\, df_r \quad (44)$$

where J_0 is the zero-order Bessel function. This expression differs from a similar (but incorrect) expression given by Voss [17, eq. (1.52)].

The 1-D and 2-D roughness spectra of an isotropic random field are related by an Abel transform [2]. This relation is more easily visualized using the surface autocorrelation functions (the inverse Fourier transforms of the 1-D and 2-D surface spectra). The 1-D autocorrelation function is a slice of the 2-D autocorrelation function:

$$S_{Z1D}(f_x) = \int_{-\infty}^{\infty} \int_{-\infty}^{\infty} R_Z(\delta_x, \delta_y)\delta(\delta_y) \cdot \exp(-j2\pi[f_x\delta_x + f_y\delta_y])\, d\delta_x\, d\delta_y. \quad (45)$$

Using Fourier transform properties:

$$S_{Z1D}(f_x) = S_Z(f_x, f_y) * \delta(f_x) = \int_{-\infty}^{\infty} S_Z(f_x, f_y')\, df_y'. \quad (46)$$

Let $S_{Z1D}(f_x, f_y)$ be given by (41), and let f_x be restricted to the power-law region, i.e., $f_x \geq f_{low}$:

$$S_{Z1D}(f_x) = 2a \int_0^{\infty} [(f_x)^2 + (f_y')^2]^{-\gamma/2}\, df_y'. \quad (47)$$

Changing variables, we have

$$S_{Z1D}(f_x) = 2a \int_{f_x}^{\infty} f_r^{-\gamma} \frac{f_r}{\sqrt{f_r^2 - f_x^2}}\, df_r \quad (48)$$

which can be integrated analytically [27, p. 201]:

$$S_{Z1D}(f_x) = \frac{a\sqrt{\pi}\,\Gamma\left(\frac{\gamma - 1}{2}\right)}{\Gamma(\gamma/2)} |f_x|^{-(\gamma-1)} \quad (49)$$

where $\Gamma(x)$ is the gamma function.

Therefore, if $S_{Z1D}(f_x) = cf_x^{-\beta}$ for $f_x \geq f_{low}$, the 1-D and 2-D spectral parameters are related by

$$\gamma = \beta + 1 \quad (50)$$

$$a = \frac{\Gamma(\gamma/2)}{\sqrt{\pi}\,\Gamma\left(\frac{\gamma - 1}{2}\right)} c. \quad (51)$$

Equation (50) agrees with the result derived by Voss; he does not give an expression comparable to (51).

As previously discussed, 1-D profiles of a fractal surface with $1 < D_f < 2$ have power-law spectra with exponent β given by $\beta = 5 - 2D_f$, so that $3 > \beta > 1$. From (50), the 2-D power-law exponent γ satisfies $4 > \gamma > 2$, corresponding to 2-D surfaces with $2 < D_f < 3$, where $D_f = (8 - \gamma)/2$.

We next investigate the performance of the linear, averaged Capon's estimator in the determination of the 2-D power-law parameters a and γ. A variation of the 2-D spectral synthesis algorithm described by [26] was used to generate 2048 × 2048-point synthetic topographic surfaces with spectral exponents of 3.0, 3.4, and 3.6 with sampling intervals Δ of 1 cm. The exact surface spectrum was modeled as isotropic, with a form similar to (17):

$$S_Z(f_r) = \begin{cases} (\alpha/\sigma^2)|f_r| \exp(-f_r^2/[2\sigma^2]) & f_r \leq f_{low} \\ af_r^{-\gamma} & f_{low} \leq f_r \leq f_c \\ 0 & f_r \geq f_c \end{cases} \quad (52)$$

where f_r is the radial spatial frequency, $a = 2.384 \cdot 10^{-11}$, $f_{low} = 0.01\ \text{m}^{-1}$, and α and σ are chosen as before. The cut-off frequency $f_c = 1/2\Delta$ is equal to the Nyquist frequency along the f_x and f_y axes.

As noted previously, arrays of data containing over a million points are often unavailable. In practice, *in situ* surface height measurements may yield data sets that are much smaller, say, 40 × 40 points. Since such a data set is useful over a relatively narrow band of frequencies, several sparse grids may be collected at different scales,

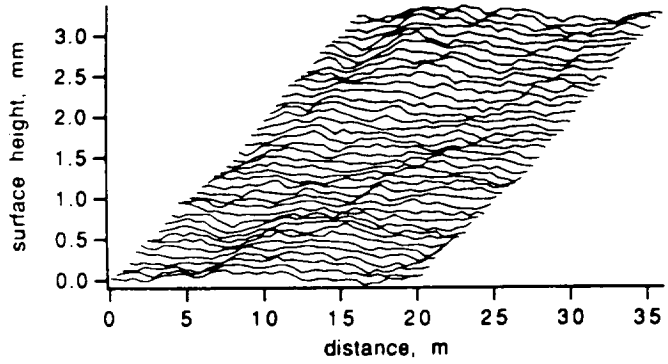

Fig. 10. 41 × 41-point sample of a 2048 × 2048-point synthetic power-law surface with $a = 2.384 \cdot 10^{-11}$ and $\gamma = 3.0$. The sampling interval is 50 cm.

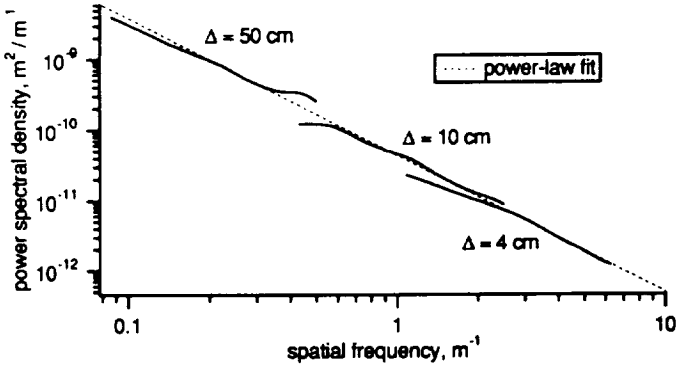

Fig. 11. Averaged Capon's estimates from 2-D synthetic surface height data at three scales with power-law fit.

TABLE III
POWER-LAW PARAMETERS DERIVED FROM FITS TO AVERAGED CAPON'S ESTIMATES AT THREE SCALES

Surface (exact)		Estimated parameters			
a	γ	mean $\hat{a}$	std. dev. $\hat{a}$	mean $\hat{\gamma}$	std. dev. $\hat{\gamma}$
$2.384 \cdot 10^{-11}$	3.0	$2.34 \cdot 10^{-11}$	$2.83 \cdot 10^{-12}$	2.971	0.041
$2.384 \cdot 10^{-11}$	3.4	$2.28 \cdot 10^{-11}$	$1.55 \cdot 10^{-12}$	3.386	0.041
$2.384 \cdot 10^{-11}$	3.6	$2.17 \cdot 10^{-11}$	$1.14 \cdot 10^{-12}$	3.555	0.061

a spectral estimate calculated for each, and a function fit to the composite of the individual spectra. Scale factors are particularly important in the calculation of these multiscale spectra.

In our investigation, we sample each 2048 × 2048-point synthetic surface at sampling intervals of 50, 10, and 4 cm, obtaining three 41 × 41-point data grids. (A sample data grid is shown in Fig. 10.) At each scale, a 1-D Capon's estimate (with $p = 12$) is calculated for each grid row at frequencies $1/(2p\Delta) < f < 1/(4\Delta)$, and the estimates are averaged over the rows. A power-law function is then fit to the averaged spectral estimates at the three scales. (A sample fit is shown in Fig. 11.) The upper frequency limit of $1/(4\Delta)$ was chosen to reduce the effect of aliasing. Estimates of 1-D power-law parameters c and β are then converted into estimates of a and γ using (50) and (51).

This process was performed on 10 synthetic surfaces at each of three spectral exponents. The mean and standard deviation of $\hat{a}$ and $\hat{\gamma}$ are listed in Table III.

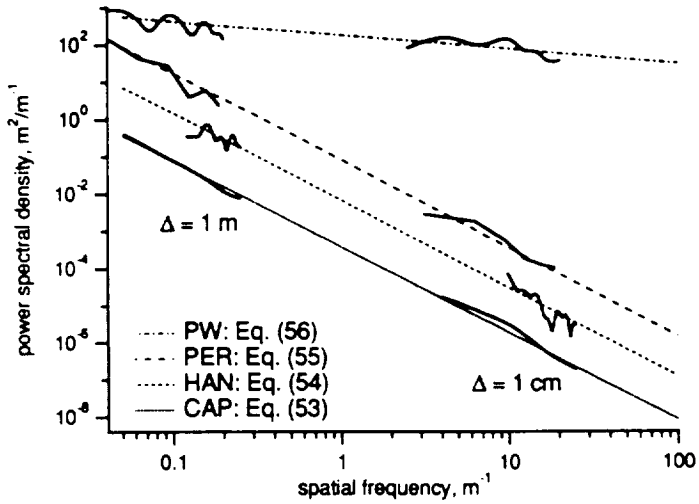

Fig. 12. Spectral estimates calculated with (from bottom to top) $\hat{P}_{CAP}$, $\hat{P}_{HAN}$, $\hat{P}_{PER}$ (with no zero-padding), and $\hat{P}_{PW}$ from surface profiles of a debris flow near Johnston Ridge at Mount St. Helens. (Spectral estimates derived from techniques other than Capon's estimator have been offset for clarity.) The dashed lines are power-law fits to the estimates; the equations of these fits are (53), (54), (55), and (56), respectively. (This and the other measured spectra from Mount St. Helens debris flows are presented in [28].).

C. Application to Measured Data

Surface roughness measurements were performed on several debris flows near Mount St. Helens in support of a study of electromagnetic scattering by volcanic terrains. The surface profiles, which were collected using several different sampling rates and profile lengths, were used to obtain estimates of the roughness spectra of the measured debris flows using the techniques described in the present report. The resulting spectra are reported elsewhere [28]. One of the spectral fits calculated from measurements of a primary debris flow near Johnston Ridge is shown in Fig. 12. This composite spectrum was derived from two surface profile grids, one with $\Delta = 1$ m, the other with $\Delta = 1$ cm. The equation of the power-law fit to the two Capon's estimates is

$$\hat{S}_Z(f) = (3.57 \cdot 10^{-4})|f|^{-2.31}. \quad (53)$$

Spectral estimates based on $\hat{P}_{HAN}$, $\hat{P}_{PER}$ (with no zero-padding), and $\hat{P}_{PW}$ were calculated from the same data for comparison with (53) and are shown in Fig. 12. Equations of the power-law fits derived from these estimators are

$$\hat{S}_{Z,HAN}(f) = (6.28 \cdot 10^{-4})|f|^{-2.36} \quad (54)$$

$$\hat{S}_{Z,PER}(f) = (7.50 \cdot 10^{-4})|f|^{-2.36} \quad (55)$$

$$\hat{S}_{Z,PW}(f) = (4.20 \cdot 10^{-4})|f|^{-2.40}. \quad (56)$$

The spectral exponents in (53)–(56) seem acceptably similar, but this is principally due to the combination of spectral estimates at different scales into a single composite spectrum. If we fit power-law functions to spectral estimates based on the $\Delta = 1$ cm data alone, we obtain the following:

$$\hat{P}_{CAP}(f) = (1.15 \cdot 10^{-3})|f|^{-2.73} \quad (57)$$

$$\hat{P}_{HAN}(f) = (3.95 \cdot 10^{-3})|f|^{-3.00} \quad (58)$$

$$\hat{P}_{PER}(f) = (2.12 \cdot 10^{-4})|f|^{-1.85} \quad (59)$$

$$\hat{P}_{PW}(f) = (9.92 \cdot 10^{-4})|f|^{-2.75} \quad (60)$$

The Capon's, modified periodogram with Hanning window, and prewhitened spectral estimators give spectral slopes between 2.73 and 3.0, but the periodogram (with no zero-padding) gives a significantly different slope $\beta = 1.85$, illustrating the effects of spectral leakage.

IV. Conclusions

Spectral analysis is a tool of increasing importance in the characterization of topography and other natural surfaces. Numerous studies indicate that such surfaces have power-law spectra in the form of (1) over some range of spatial frequencies. This spectral form introduces unique difficulties in the spectral estimation process.

In the present work, we have shown how leakage causes some Fourier-based estimators to yield an estimated spectral exponent of 2.0 for surface profiles having spectral exponents between 2 and 3. This may explain the number of studies reporting power-law exponents of 2.0 for natural terrains. We show how Capon's estimator may be used to avoid the leakage problem and measure the surface spectrum more accurately. We also show that Capon's estimator has reduced variance, which is useful when surface data records are short, as is often the case in remote-sensing studies.

The two-dimensional Capon's estimator may be employed to compute 2-D spectra of rough surfaces. However, two-dimensional data are often unavailable or too sparse. For surfaces that are known or can be assumed to be isotropic, we show how a linear, averaged Capon's estimator can be used to estimate the 2-D power-law parameters.

Acknowledgment

The authors wish to thank several anonymous reviewers for their helpful comments and suggestions.

References

[1] J. Huang and D. L. Turcotte, "Fractal mapping of digitized images: Application to the topography of Arizona and comparisons with synthetic images," *J. Geophys. Res.*, vol. 94, pp. 7491-7495, June 10, 1989.

[2] J. A. Goff, "Comment on 'Fractal mapping of digitized images: Application to the topography of Arizona and comparison with synthetic images,'" *J. Geophys. Res.*, vol. 95, p. 5159, Apr. 10, 1990.

[3] J. Huang and D. L. Turcotte, "Reply," *J. Geophys. Res.*, vol. 95, p. 5161, Apr. 10, 1990.

[4] ——, "Fractal image analysis: Application to the topography of Oregon and synthetic images," *J. Opt. Soc. Amer.: A*, vol. 7, pp. 1124-1130, June 1990.

[5] A. W. England, "The fractal dimension of diverse topographies and the effect of spatial windowing," *Geolog. Surv. Can.*, Paper 90-4: Ground Penetrating Radar, J. A. Pilon, Ed., pp. 57-61, 1992.

[6] S. R. Brown and C. H. Scholz, "Broad bandwidth study of the topography of natural rock surfaces," *J. Geophys. Res.*, vol. 90, pp. 12 575-12 582, 1985.

[7] T. H. Bell, Jr., "Statistical features of sea-floor topography," *Deep-Sea Res.*, vol. 22, pp. 883-892, 1975.

[8] ——, "Mesoscale sea floor roughness," *Deep-Sea Res.*, vol. 26A, pp. 65-76, 1979.

[9] C. G. Fox and D. E. Hayes, "Quantitative methods for analyzing the roughness of the seafloor," *Rev. Geophys.*, vol. 23, pp. 1-48, Feb. 1985.

[10] L. E. Gilbert and A. Malinverno, "A characterization of the spectral density of residual ocean floor topography," *Geophys. Res. Lett.*, vol. 15, pp. 1401-1404, Nov. 1988.

[11] A. Malinverno, "Segmentation of topographic profiles of the seafloor based on a self-affine model," *IEEE J. Ocean. Engineer.*, vol. 14, pp. 348-359, Oct. 1989.

[12] R. S. Sayles and T. R. Thomas, "Surface topography as a nonstationary random process," *Nature*, vol. 271, pp. 431-434, Feb. 2, 1978.

[13] M. V. Berry and J. H. Hannay, "Topography of random surfaces," *Nature*, vol. 273, p. 573, June 15, 1978.

[14] B. B. Mandelbrot, *The Fractal Geometry of Nature*. New York: Freeman, 1983.

[15] R. J. Adler, *The Geometry of Random Fields*. New York: Wiley, 1981.

[16] B. B. Mandelbrot and J. W. Van Ness, "Fractional Brownian motions, fractional noises, and applications," *SIAM Rev.*, vol. 10, pp. 422-437, 1968.

[17] R. F. Voss, "Fractals in nature: From characterization to simulation," in *The Science of Fractal Images*, H.-O. Peitgen and D. Saupe, Eds. New York: Springer-Verlag, 1988, pp. 21-70.

[18] S. E. Hough, "On the use of spectral methods for the determination of fractal dimension," *Geophys. Res. Lett.*, vol. 16, pp. 673-676, July 1989.

[19] W. H. Press, B. P. Flannery, S. A. Teukolsky, and W. T. Vetterling, *Numerical Recipes (FORTRAN Version)*. Cambridge: Cambridge Univ., 1989.

[20] S. M. Kay, *Modern Spectral Estimation*. Englewood Cliffs, NJ: Prentice Hall, 1988.

[21] P. D. Welch, "The use of fast Fourier transform for the estimation of power spectra: A method based on time averaging over short, modified periodograms," *IEEE Trans. Audio Electroacoust.*, vol. AU-15, pp. 70-73, June 1967.

[22] R. B. Blackman and J. W. Tukey, *The Measurement of Power Spectra from the Point of View of Communications Engineering*. New York: Dover, 1958.

[23] A. V. Oppenheim and R. W. Schafer, *Digital Signal Processing*. Englewood Cliffs, NJ: Prentice Hall, 1975.

[24] R. E. Ziemer and W. H. Tranter, *Principles of Communications: Systems, Modulation, and Noise*, 2nd ed. Boston, MA: Houghton Mifflin, 1985.

[25] J. Capon, "High-resolution frequency-wavenumber spectrum analysis," *Proc. IEEE*, vol. 57, pp. 1408-1418, Aug. 1969.

[26] D. Saupe, "Algorithms for random fractals," in *The Science of Fractal Images*, H.-O. Peitgen and D. Saupe, Eds. New York: Springer-Verlag, 1988, pp. 71-136.

[27] Bateman Manuscript Project, *Tables of Integral Transforms*, vol. 2, A. Erdélyi, Ed. New York: McGraw-Hill, 1954.

[28] R. T. Austin and A. W. England, "Multi-scale roughness spectra of Mount St. Helens debris flows," *Geophys. Res. Lett.*, vol. 20, pp. 1603-1606, Aug. 6, 1993.

Richard T. Austin (S'84) was born in Maryville, TN, on September 2, 1964. He received the B.S. degree in electrical engineering from the University of Kentucky, Lexington, in 1986 and the M.S.E. degree in electrical engineering from the University of Michigan, Ann Arbor, in 1987.

He is presently pursuing the Ph.D. degree in electrical engineering at the Radiation Laboratory at the University of Michigan. During his studies, he has held a National Science Foundation Graduate Fellowship and a Michigan Space Grant Fellowship. His research interests including scattering and emission from natural surfaces and radiometric studies of the atmosphere.

Mr. Austin is a member of Tau Beta Pi and the American Geophysical Union.

Anthony W. England (M'87-SM'89) received the B.S. degree in earth sciences (1965), the M.S. degree in geology and geophysics (1965), and the Ph.D. degree in geophysics (1970) from the Massachusetts Institute of Technology, Cambridge, MA.

His research interests have included terrestrial heat flow; geomagnetic and gravimetric studies in the northern Rockies and in Antarctica; radar studies of temperate and polar glac... ; and the microwave radiometric signatures of snow, ice, frozen and thawed soils, and planetary regoliths. He was Deputy Chief of the Office of Geochemistry and Geophysics of the U.S. Geological Survey, and was an Associate Editor for the *Journal of Geophysical Research*. He served on several federal committees concerned with Antarctic policy, nuclear waste containment, and federal science and technology. He was appointed as a NASA Scientist-Astronaut in 1967, acted as Mission Scientist for Apollo's 13 and 16, and flew as a Mission Specialist on Space Shuttle Challenger's Spacelab 2 Mission in 1985—a solar astronomy and plasma physics mission. He has been a Program Scientist for NASA's Space Station. He is currently a member of the NAS/NRC's Space Studies Board and a member of several NASA advisory committees. He has been an Adjunct Professor at William Marsh Rice University, Houston, TX, and is now a Professor of Electrical Engineering and Computer Science at the University of Michigan, Ann Arbor, MI.

Dr. England is a member of the American Geophysical Union.

Gregory H. Wakefield (S'84-M'84) received the B.A. degree *summa cum laude* in mathematics and psychology, the M.S. degree in electrical engineering, the Ph.D. degree in electrical engineering, and the Ph.D. degree in psychology, all from the University of Minnesota, Minneapolis, in 1978, 1982, 1985, and 1988, respectively.

From 1978 to 1985, he was with the Psychoacoustics Laboratory, University of Minnesota. From 1983 to 1985, he was with the Communications Laboratory and the St. Anthony Falls Hydraulics Laboratory, University of Minnesota. From 1982 to 1983, he was a consultant to the Technology Strategy Center, Honeywell, Minneapolis. From 1982 to 1985, he was consultant to the Bioscience Laboratory, Life Science Sector, 3M, St. Paul. Since 1986, he has been on the faculty of the University of Michigan, Ann Arbor, where he is currently an Associate Professor with the Department of Electrical Engineering and Computer Science. His research interests are in statistical signal processing, signal analysis and synthesis, image processing, spectral estimation, sensory systems modeling, psychoacoustics, sensory prosthetics, speech processing, and music processing. He has been involved in teaching and research in these areas and has led in the development of the educational laboratories in signal processing (SPEL) and in image processing (IPEL) at the University of Michigan.

Dr. Wakefield received the Presidential Young Investigator Award (1987), the University of Minnesota Doctoral Dissertation Fellowship (1982), and the USPHS Traineeship with the Center for Research in Human Learning (1979-1982). He is a member of Phi Beta Kappa and Sigma Xi and his professional affiliations include the Acoustical Society of America.

V Empirical Model

There are no reliable scattering models for surfaces whose roughness spans the spatial frequencies of the radar's wavenumber. In fact, a comparison between an empirical model and the predictions of several candidate theories is one of the tasks of the study. The empirical model was based upon scattering measurements of milled surfaces that were carefully produced to exhibit power-law roughness for 3 values of β (2.29, 2.55, and 2.80). The process for manufacturing the scattering surfaces became Chapter V in R.T. Austin's Ph.D. dissertation [69]. The process of measuring the radar backscatter from these surfaces became Chapter VI of the dissertation. His results were presented at an International Geoscience and Remote Sensing Seminar (IGARSS'94) in Pasadena, CA [68]. They will also appear in a TGARS paper. Chapters V and VI of Dr. Austin's thesis appears on the following 41 pages.

CHAPTER V

DESIGN AND MANUFACTURE OF ARTIFICIAL POWER-LAW SURFACES

The spectral estimates in the previous chapter show that certain volcanic debris flow surfaces at Mount St. Helens belong to the class of power-law surfaces discussed in Chapter II. The cited references and the present study show that power-law surfaces are common and often of interest in remote sensing. A better understanding of electromagnetic scattering by these surfaces may be obtained through scattering measurements and application of rough surface scattering models.

In situ scattering measurements of natural power-law surfaces are difficult to perform and even more difficult to interpret for purposes of model verification. Aside from common logistical problems (e.g., operation of radars in dusty environments, cost and time constraints for on-site work), there are several measurement uncertainties which interfere with model verification. Natural rough surfaces rarely conform to a single statistical description over extended areas due to the variety of processes that contribute to their formation. For land surfaces, volume scattering by subsurface inhomogeneities is usually present. Both of these factors yield effects that are difficult to decouple from those due to surface roughness. More important, interpretation of scattering measurements is hindered by the difficulty of obtaining an

accurate statistical description of surface roughness. As discussed in Chapters III and IV, estimation of the surface roughness spectrum is particularly problematic for power-law surfaces, requiring a large quantity of surface height data and specialized spectral estimation algorithms.

The uncertainties just discussed may be largely avoided through the use of manufactured surface analogues. The analogues are homogeneous, conforming to a single specified statistical model. They are constructed from a homogeneous material to eliminate subsurface scattering, and their surface statistics are well known. Because the surface roughness is specified by the investigator, particular cases of roughness may be studied, or a single roughness parameter may be varied in order to study its effect on surface scattering. Finally, the scattering measurements may be performed under more controlled conditions, typically indoors, allowing greater accuracy and repeated measurements if necessary.

This chapter describes the design and manufacture of artificial power-law surfaces. The design history, material selection, and surface generation algorithm are discussed, and the milling system is described. The milling procedure is explained, including time and disk space requirements, and difficulties in milling complex surfaces are discussed. The chapter ends with a description of surface verification efforts.

5.1 Analogue design history

The original project plan called for the manufacture of power-law surfaces measuring one meter square. The surfaces were to be composed of a dielectric material with permittivity near that of soil. Scattering by the surfaces was to be measured using an X-band (9.75 GHz) radar and radars of other frequencies if available.

Surface construction was planned to be similar to that used by Nance [44], who

presented scattering results from artificial Gaussian conducting surfaces [45]. As in his study, the surface fabrication was to be performed by a contractor; however, requirements for the present study were more sophisticated due to the more complex surface roughness (power-law instead of Gaussian) and the use of a homogeneous dielectric rather than structural foam that was to be coated with conducting paint.

After an extensive search of machining companies in southeast Michigan, I was unable to find a contractor who was able to fabricate the surfaces for a manageable cost. One obstacle was the desired surface size: one meter square was too large for several companies' equipment. A more significant impediment was insufficient data capacity. The design specification for the artificial surfaces called for the replication of surface features on the scale of one-tenth or one-twentieth of the radar wavelength. A high number of surface points were therefore required to represent the surface for fabrication (the surfaces eventually required 1318 × 1318 points). This quantity of data was quite beyond the capabilities of numerous machining firms, several of whom specified their data capacities in feet of paper tape.

One company was found in Brighton which would probably have been able to fabricate the surfaces. However, the eventual cost per surface and inconvenience of working with an out-of-town company, as well as the likelihood of needing several attempts to get a usable surface, led to the decision to purchase milling equipment and manufacture the surfaces at the Radiation Laboratory.

5.2 Dielectric materials

Although a dielectric surface introduces greater complexity in construction and in backscatter modeling, the greater similarity to natural terrains led to the selection of a dielectric surface rather than a conducting surface. There were multiple conflicting

requirements for the dielectric material:

- homogeneous (to avoid volume scattering)
- high permittivity (to assure a measurable return signal)
- lossy (to eliminate reflections from the bottom surface of the dielectric)
- machinable using standard milling equipment
- inexpensive
- low density (to eliminate need for elaborate target mount or special handling)

A variety of candidate materials were examined [55]. Machinable wax and mixtures of machinable wax and graphite were rejected as too expensive and insufficiently strong to support their weight (a one meter square slab might crack when being moved). A mixture of graphite, titanium dioxide, and silicone resin suggested by engineers at Texas Instruments was attempted but was never made to solidify. A mixture of plaster and conductive paint was rejected due to concerns about homogeneity and durability (cracking under tension). The material ultimately selected, ultra-high molecular weight polyethylene (UHMW), was chosen for its good machinability, homogeneity, and reasonable cost.

The search for dielectric materials led to a change in the dimensions of the artificial surfaces. This change was principally due to mass and cost constraints. A 1 m $\times$ 1 m $\times$ 15 cm slab of these materials could measure from 130 to 260 kg, requiring a very strong (and probably highly scattering) surface mount and special support to prevent the material from cracking under its own weight. By changing the surface scale by a factor of 3.538, the X-band measurement could be simulated using a 35 GHz radar with a smaller and shallower target surface. Surface strength was less

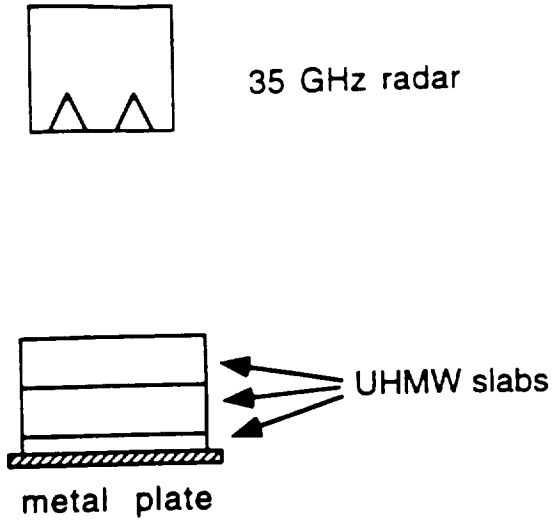

Figure 5.1: Configuration for measuring UHMW dielectric constant.

critical at the new scale, and obtaining a measurable return was less a problem at 35 GHz than at X-band. The decision to reduce the surface scale was fortuitous in view of problems with the milling table that will be described later. A surface size of 18 inches (45.72 cm) square was selected based on availability of UHMW slabs. This size corresponds to an X-band surface measuring 63.7 in. (161.8 cm) square and is sufficiently large to allow two radar looks with minimal footprint overlap.

Because UHMW polyethylene is not lossy, elimination of reflections from the bottom surface of the slabs was accomplished using the time-gating feature of the network analyzer that processes the radar signals. Several 6-inch slabs of UHMW were placed beneath the milled slab to move the bottom interface away from the milled surface. This configuration is described and illustrated in Chapter VI.

The dielectric constant of the UHMW slabs was measured using the 35 GHz radar as shown in Figure 5.1. The radar was pointed vertically downward at a stack of UHMW slabs (two 6-inch and one 2-inch) and the radar bandwidth set to 3 GHz for maximum resolution. A metal plate was inserted at various levels in the stack to

identify the reflections from the top, bottom, and internal interfaces. Removing the plate, the time interval between the returns from the top and bottom was found to be 3.397 ns. The round-trip time for travel through free space at the same distance (0.355 m) is 2.37 ns; the ratio of these times gives the index of refraction, $n = 1.433$. The dielectric constant is then obtained directly:

$$\epsilon_r = n^2 = 2.05. \tag{5.1}$$

Polyethylene has extremely low loss in tabulated values below and above 35 GHz; it was believed that the loss tangent would be too small to measure at 35 GHz using techniques available in the Radiation Laboratory. The dielectric constant was therefore assumed to be completely real.

5.3 Surface Design Algorithm

The surface height was specified over a 1318 × 1318-point grid with a point spacing of 1.23 mm (0.04843 in.) at the X-band scale or 0.3477 mm (0.01369 in.) at the 35 GHz (milling) scale. The surface profile was generated using a variation of the two-dimensional spectral synthesis technique described by Saupe [51] and explained as follows: The desired surface spectrum is the two-dimensional power-law spectrum:

$$S_Z(f_r) = a f_r^{-\gamma}, \tag{5.2}$$

where $f_r = (f_x^2 + f_y^2)^{1/2}$ is the radial spatial frequency. First, a set of 2048 × 2048 discrete Fourier amplitudes $\tilde{Z}_1(f_x, f_y)$ is generated such that

$$\frac{1}{N^2\Delta^2}|\Delta^2 \tilde{Z}_1(f_x, f_y)|^2 = S_Z(f_x, f_y) \tag{5.3}$$

for all points within the circle $f_r < f_c$, where f_c, the maximum spatial frequency, was $(2\Delta)^{-1} = 406.5\ \mathrm{m}^{-1}$. Point spacing in the frequency domain was $\Delta_f = (N\Delta)^{-1} =$

$0.39698\ \mathrm{m}^{-1}$. In other words,

$$\tilde{Z}_1(f_x, f_y) = \frac{N}{\Delta}\sqrt{a}(f_r)^{-\gamma/2}. \tag{5.4}$$

A dimension of 2048 is chosen because the FFT algorithm requires N to be an integer power of two, and 1024 is not large enough. The amplitudes $\tilde{Z}_1$ are then multiplied by a randomness factor and a phase factor:

$$\tilde{Z}(f_x, f_y) = \tilde{Z}_1(f_x, f_y)\mathcal{G}e^{i\Phi}, \tag{5.5}$$

where $\mathcal{G}$ is a Gaussian random variable with zero mean and unity variance, and Φ is a phase random variable uniformly distributed over $[0, 2\pi]$. In this way, the mean value of the normalized square of the spectral amplitudes still satisfies (5.3). To ensure that the surfac heights are real-valued, the above procedure is used to generate half the surface amplitudes, and the other half are obtained by enforcing Hermitian symmetry:

$$\tilde{Z}(f_x, f_y) = \tilde{Z}^*(-f_x, -f_y), \tag{5.6}$$

The randomized coefficien s $\tilde{Z}(f_{xm}, f_{yn})$ constitute the fast Fourier transform (FFT) of one realization of a rough surface random process having a roughness spectrum given by (5.2). To obtain the two-dimensional surface profile, an inverse FFT is performed on the coefficient array:

$$Z(x_k, y_l) = \frac{1}{N^2}\sum_{m=0}^{N-1}\sum_{n=0}^{N-1}\tilde{Z}(f_{xm}, f_{yn})\exp(-i2\pi[km + ln]/N). \tag{5.7}$$

The resultant synthetic surface array has 2048×2048 points; profiles were truncated to 1318×1318 points for surfaces in the present study.

The surface roughness parameters, a and γ in (5.2), were selected to be similar to those measured at Mount St. Helens and to be physically realizable on UHMW slabs using the milling machine. At the time the first artificial surface was designed,

the estimated two-dimensional roughness spectrum based upon survey site 1 and profilometer scans 3a and 3b had $\hat{a} = 1.52 \times 10^{-4}$ and $\hat{\gamma} = 3.29$. (The surface spectral estimate was subsequently changed to $a = 1.7672 \times 10^{-4}$ and $\gamma = 3.345$.) The UHMW slabs were 2 inches thick; reserving a minimum thickness of one-half inch for stability left a possible total relief of 1.5 inches. In order to obtain a surface profile having this amount of relief after scale reduction by a factor of 3.538, it was necessary to reduce the roughness amplitude, a, by a factor of 7. The final roughness spectrum used for the first surface analogue, UHMW1, had the mixed form of (4.50):

$$S_Z(f_r) = \begin{cases} (\alpha/\sigma^2) f_r \exp(-f_r^2/[2\sigma^2]), & f_r \le 0.01 \text{ m}^{-1} \\ a f_r^{-\gamma}, & 0.01 \text{ m}^{-1} \le f_r \le f_c \\ 0, & f_r \ge f_c \end{cases}, \qquad (5.8)$$

where

$$a = 2.17143 \times 10^{-5}$$

$$\gamma = 3.29$$

$$\alpha = 1.6438$$

$$\sigma = 0.00482805$$

$$f_c = 406.5 \text{ m}^{-1}$$

The parameters α and σ were chosen as in Chapter IV by enforcing continuity of the spectrum and its first derivative. In effect, however, these parameters had no effect (except at frequency zero) due to the limited resolution of the spectral synthesis technique; the lowest non-zero frequency (equal to $1/N\Delta$) was 0.39698 m^{-1}, which fell outside the Rayleigh region of the mixed spectrum.

Spectral parameters for the second and third surface analogues were selected to span the range of spectral slopes (or alternatively, fractal dimensions) that natural

Surface	UHMW1	UHMW2	UHMW3
a	2.17143×10^{-5}	2.17143×10^{-5}	2.17143×10^{-5}
γ	3.29	3.8	3.545
α	1.6438	19.8523	5.70356
σ	0.00482805	0.00456435	0.00469065
D_f	2.355	2.1	2.2275

Table 5.1: Spectral parameters (a, γ, α, and σ in (5.8)) used and fractal dimension D_f of the surface analogues.

terrains reasonably assume. The roughness amplitude, a, was held constant; the spectral slope, γ, was set to 3.8 for UHMW2 and to an intermediate value of 3.545 for UHMW3. The values of the four spectral parameters and the associated fractal dimensions are summarized in Table 5.1.

5.4 Milling System

The milling system was ordered in November 1991 and arrived in early 1992. The system has existed in two forms: the original configuration, as supplied by Techno, and the upgraded configuration made necessary due to reliability problems with the Techno components.

5.4.1 Origi al Milling System n

The system as originally purchased (see Figure 5.2) consisted of a Techno three-axis gantry positioning table, a Kress variable-speed electronic grinder, and a Techno MAC 100 programmable position controller, all purchased from Techno, New Hyde Park, New York; CNC Software's Mastercam CAD/CAM software, purchased from

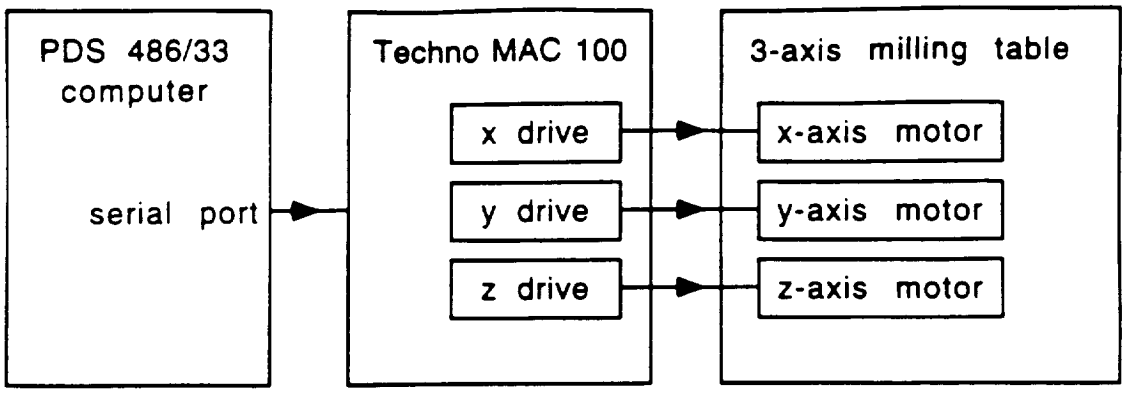

Figure 5.2: The original milling system supplied by Techno.

CIM Solutions of Canton, Michigan; and a Peer Data Systems 486/33 MHz DOS-compatible computer, purchased from Peer Data Systems of Ann Arbor, Michigan. The components of the system are described in this section.

The three-axis gantry positioning table holds the construction material in place and allows the milling tool to be moved to designated xyz coordinates. The table and x- and z-axis supports were constructed from extruded aluminum section. Precise motion in the x, y, and z directions was obtained via the rotation of ball screw assemblies by stepper motors. The ball screw mechanisms were covered by expanding vinyl bellows to protect them from dust and shavings. Limit switches at one end of each axis's range of motion provided a mechanism for zeroing the table. Table positioning was theoretically accurate to 0.01 mm (0.0004 inch), which was the linear motion obtained by rotating a stepper motor one step. This precision far exceeded the requirements for this project. The table was ordered in a special size, 48 × 49 inches, and with extra clearance (8 inches) for the z axis to allow milling a fairly thick slab measuring one meter square in a single piece.

One problem that became apparent soon after starting work with the table was that the table sagged somewhat under its own weight due to support beams that were

insufficient for the table size. A test load of 227 kg (500 pounds) distributed over a 1 m^2 area in the center caused a sag of 4.3 mm. To reduce the sag to acceptable levels, Techno provided an iron L-beam that was attached to table surface. The L-beam corrected the sag problem but reduced the usable table area. Fortunately, the desired surface size had been reduced by this time.

The Kress electronic grinder rotates the milling tool, removing surface material as it travels along a programmed path. The grinder was attached to the z-axis and held an endmill (milling tool) in a collet of 3/8, 1/4, or 1/8-inch diameter. The rotation speed was adjustable from 8,000–20,000 rpm.

The MAC 100 programmable position controller accepts toolpath coordinates from a post-processing program running on the 486 computer and translates these into properly timed currents in the windings of the stepper motors on the three axes. The MAC 100 controller was built by Techno, using some Techno-designed boards and other components built by Compumotor. The controller operated as an open-loop system; i.e., there was no position feedback from the axes to the controller, so the controller had no way to verify that the stepper motors and axes had moved to specified positions. Open-loop control is not uncommon in stepper motor systems, but it is less reliable than closed-loop control, as will be discussed later.

The CNC Software Mastercam Mill package is an extensive program for designing complex objects, producing machine toolpaths for the fabrication of these objects, and controlling the machining equipment while executing the machine toolpath instructions. (However, the Techno controller must be operated by a Techno post-processor program and not from within Mastercam.) Because the surfaces in this study were extremely large and complex, and because they were produced by an external program on another computing platform, many of the features of the Mas-

tercam package were not used. The principal use of the Mastercam package was to read a file of surface height coordinates and write files of toolpath coordinates for different milling tools. (Several sizes of tools were used in different stages of the milling process.) Techno sells a version of Mastercam designed for 286 computers; the faster and more sophisticated 386 version was needed in this study, so it was purchased from CIM Solutions.

Both Mastercam and the post-processor program were run on the Peer Data Systems 486/33 MHz DOS-compatible computer. The computer had 16 megabytes of random access memory and a 210 megabyte hard disk drive, and was augmented with an Ethernet board to allow file transfer with the Unix workstations on campus. The communications link was necessary because Mastercam could process only a section of the artificial surface at a time. In the process, very large disk files were generated; it was not possible to retain all the surface files on the hard disk.

5.4.2 Failure of the Techno System

The Techno system began having problems in October 1992. The z-axis motor either slipped or rotated in the wrong direction and seemed to be overheating during some test runs on wood surfaces. Upon inspection, the solder joints on the connector card inside the motor housing had heated up enough to melt the solder. Engineers at Techno were unable to determine a cause for the failure.

In January 1993, it was proposed that the z-axis motor might be overheating due to excess weight on the z axis. The z axis was reverse-mounted on the Techno table to allow the full 8 inches of clearance; i.e., it was installed so that the movable carrier stayed fixed while the rest of the z-axis assembly moved up and down. To relieve part of the load on the z-axis motor, an 11.5-inch tension spring and support rod

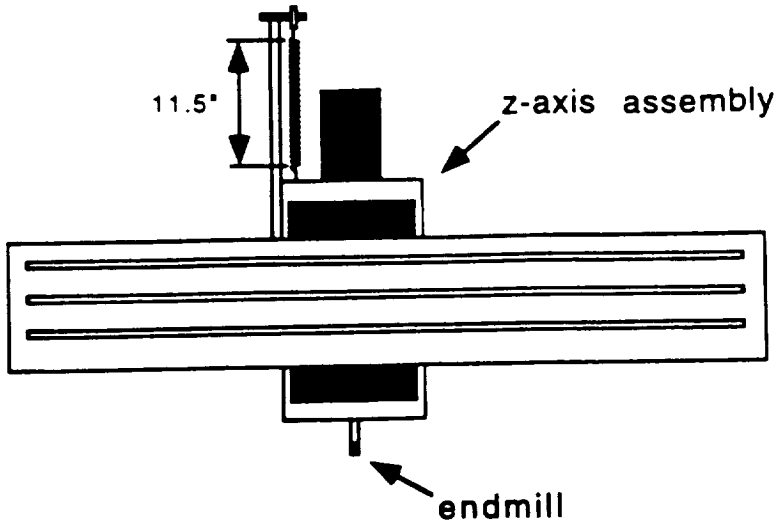

Figure 5.3: A load-bearing spring was installed on the z-axis to help support its weight.

were installed as illustrated in Figure 5.3. The spring constant and position were selected such that the spring force balanced the weight of the z-axis assembly in its mid-position. The spring seemed to solve the slippage problems. Milling on the first UHMW slab commenced in February 1993.

By early March, the machine seemed sufficiently reliable to leave it operating overnight, which was a great advantage, considering the very lengthy milling times. However, the machine began to malfunction again in late March: this time, the y axis became confused during a finishing run, resulting in a deep gouge in the slab. Manual commands to the mill were sporadically executed incorrectly. At this point, AC line noise was suspected, so an isolation transformer was installed. Machine operation was then normal again.

In mid-April, the problem recurred. Both the y and z axes malfunctioned during an overnight roughing operation. The 1/4-inch endmill had milled down through the slab and through part of the table itself. The simultaneous failures of two axes led

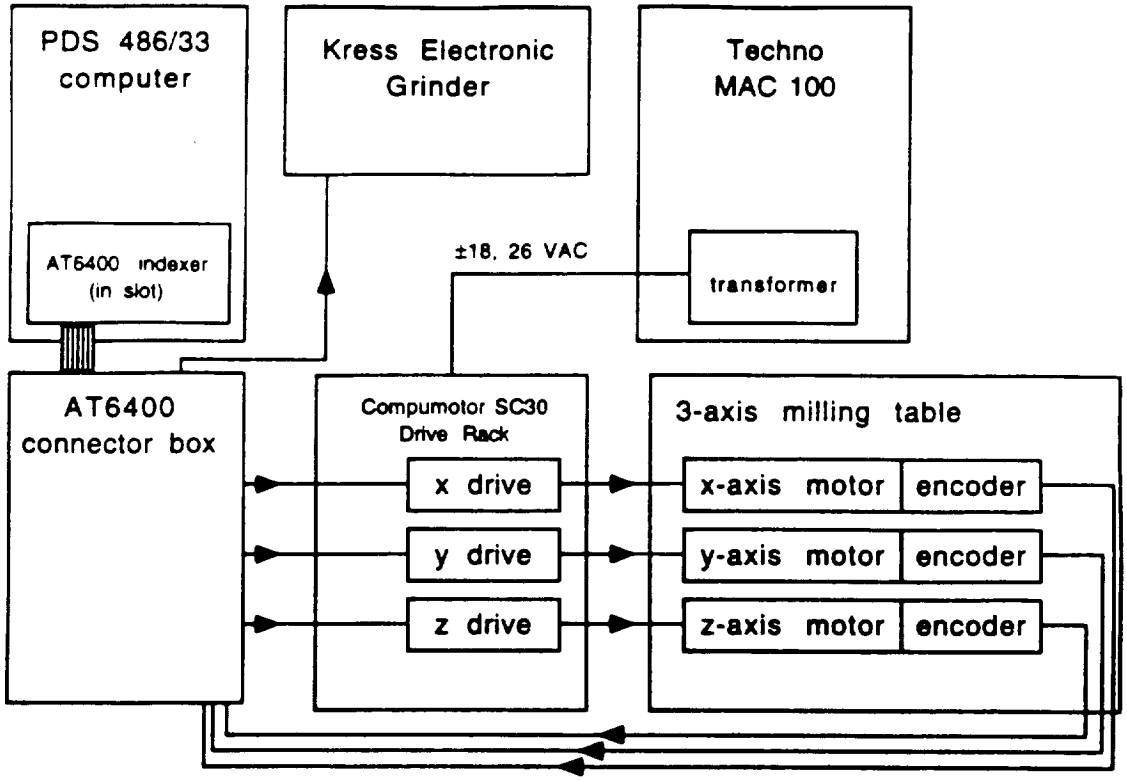

Figure 5.4: The upgraded mill configuration.

to the conclusion that the Techno MAC 100 controller was not reliable. This was a reasonable assumption in view of the other engineering problems with the Techno equipment.

5.4.3 Upgraded Milling System

The upgraded milling system is shown in Figure 5.4. The Techno MAC 100 was replaced by a Compumotor AT6400 Indexer and a Compumotor SC30 Motherboard Rack, purchased from Amerinetics of Novi, Michigan. Optical encoders (part number MOD5641-25-100-L) were purchased from BEI Motion Systems of Plymouth, Michigan. Motion Architect software, included with the AT6400 from Compumotor, was used with Microsoft Visual Basic to write new control software. The indexer,

drive rack, and encoders arrived in late July 1993.

The AT6400 indexer is the central controller of the upgraded system. The indexer receives ASCII-format move instructions from the control software, for example, "move x axis 100 steps right." The indexer then converts these instructions to step pulses and direction signals that are sent to the stepper motor drive card for each axis. These drive cards were removed from the MAC 100 but were manufactured by Compumotor; they were installed in the Compumotor SC30 Motherboard Rack for use in the upgraded system. The three stepper motor drivers use the step pulses and direction signals to drive the windings in the stepper motors in sequence, producing rotation in the specified direction.

The optical encoders were installed to provide feedback to the indexer. They were mounted on the stepper motor cases using epoxy such that the motor shafts projected through the encoders. The encoders consist of two LED's and a rotating glass disc with 100 equally spaced lines. As the encoder turns, light from an LED is alternately blocked and then transmitted through the glass disc. The two detectors are in quadrature, resulting in 400 encoder pulses per revolution. The encoders are relative sensors—they do not provide absolute coordinates, so the indexer must keep a count of encoder pulses. The control software was written so that after each mill move, the encoder step count was compared to the stepper motor step count. If the counts disagreed by more than two steps, the program stopped, and the mill was deactivated.

In addition to the encoder inputs, the indexer also had inputs from a home limit switch on each axis and a limit switch on the z axis that stopped the mill if the z axis went too low. Additional inputs from jog switches allowed manual control of the mill position. The indexer also had programmable outputs, one of which was used

to operate a relay that activated and deactivated the grinder motor.

One other component of the MAC 100 was retained: the large transformer that converted 115 VAC down to 18 and 26 VAC to supply the motherboard rack and stepper motor drives. A transformer malfunction seemed unlikely.

5.5 Milling procedure

5.5.1 Generation of Toolpath Files

Surface fabrication begins with the spectral synthesis procedure, described earlier in this chapter, which results in an 22.6 MB ASCII file of surface elevations arranged in a 1318 × 1318-point grid. Because the Mastercam software cannot accept input of more than 100 lines of ASCII surface elevations, the surface must be segmented into thirteen sections of 99 lines plus a fourteenth section of 31 lines. The FORTRAN program `ds2mcinv.f` performs this segmentation and applies the scale factor converting the surface from the X-band scale down to the 35 GHz scale. The program writes the surface sections as long lists of xyz coordinates. The resultant files measure about 5 MB each.

The edges of the surface analogues were rounded by subtracting the random scaled height from a 1/4-inch radius along each edge, as shown in Figure 5.5. The rounding was performed so that no non-random sharp edges would be illuminated by the radar. Most rays striking the rounded edges should be scattered away from the radar. The FORTRAN program `edgemax.f` reads the surface file and writes a 3.8 MB file of edge coordinates.

A couple of sections at a time are downloaded to the 486 computer. Mastercam is then used to convert the surface elevation files into toolpath files at two resolutions. Roughing files contain toolpaths for a 1/4-inch ball-end endmill. This tool is used to

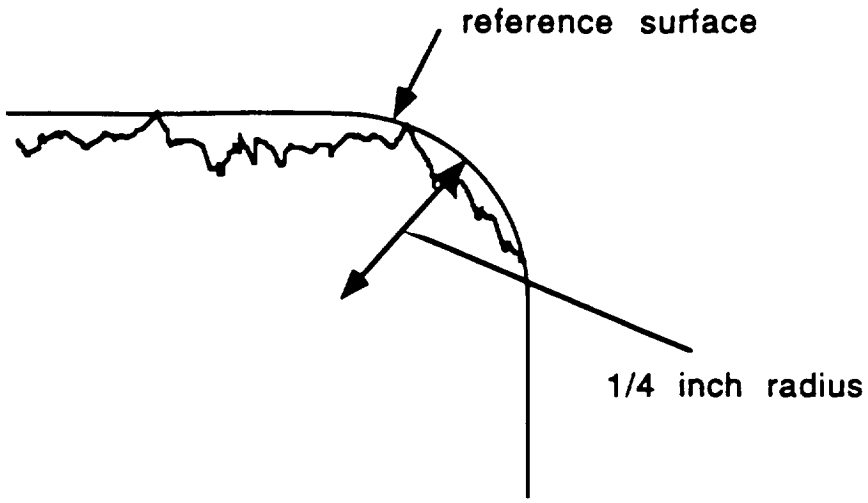

Figure 5.5: Edges of the artificial surface are rounded by subtracting the surface elevation from a rounded reference surface with a 1/4-inch radius of curvature.

remove the bulk of material at a rate much faster than the smaller tools. Finishing toolpaths are much more detailed (and much larger) and are used for the passes using the 1/16-inch and 1/32-inch ball-end endmills. Cross toolpaths are for the orthogonal finishing pass with the 1/32-inch endmill.

The toolpath (`.NCI`) files are produced in several steps [54]. An ASCII file is input, and the resultant surface description is saved in Mastercam format as a geometry (`.GE3`) file. The next step is to chain the surface, i.e., to define the contours to be milled. This creates a chaining (`.NCS`) file. After chaining, which need be done only once per section, the tool parameters and desired resolution are entered, and Mastercam writes surface (`.CDB`), offset surface (`P.CDB`), and toolpath (`.NCI`) files, in addition to some miscellaneous small intermediate files. When all three toolpaths have been written, the roughing toolpath is filtered by removing points within a specified distance from the splines used to define the surface. This significantly

File type	extension	roughing	finishing	cross
geometry	*.GE3	12		
chaining	*.NCS	12.5	12.5	12.5
surface	*.CDB	0.4	3.2	3.2
offset	*P.CDB	0.4	3.2	3.2
toolpath	*.NCI	0.02	4.6	4.6

Table 5.2: Types and sizes (in MB) of Mastercam files.

decreases the size and execution time of the roughing toolpath.

Entering, processing, and transferring the generated files for a single section takes about 3 hours. The sizes of the various Mastercam files are given in Table 5.2. Some of these may be deleted (the offset surface and all but one of the chaining files), but the rest are uploaded to a Unix workstation and saved on magnetic tape, to avoid lengthy re-processing if a toolpath file is lost.

5.5.2 Milling machine operation

The surface slab, which has been milled flat using a flat-end endmill, is mounted on the milling table after aligning its edges with the x and y table directions. It is held in place using aluminum angles tightened against each side of the slab. The mounting brackets are tightened carefully because re-aligning the slab would be extremely difficult if it came loose. In several instances, it was necessary to mill the aluminum brackets down a few millimeters in places where the surface was low near its edge.

A Visual Basic program called `mill` controlled the entire milling process. Visual Basic was quite useful because it allowed easy construction of virtual control

panels and readouts describing the milling machine status. During operation, the program displays the current position of the mill (in steps and in inches), the encoder-determined position (in steps and in inches), and an estimate of time remaining until completion.

To begin roughing, a 1/4-inch ball-end endmill is placed in the grinder collet and tightened firmly. After homing the mill to zero using the limit switches on the three axes, the endmill is positioned over the starting corner of the surface. It is lowered carefully until a sheet of paper can no longer slide between the endmill and the surface. This position is recorded as the reference level. Next, the endmill is moved over a small block of metal attached to the table near the slab, and the process is repeated. The z coordinate is recorded and is used later to verify the endmill position. For example, the indexer and program have no way to detect when an endmill slips within the collet, but the metal block test will show the slippage. The block also provides a way to determine the starting position after changing tools.

The first roughing pass is offset above the reference plane so that the maximum depth milled is 0.2 inches. Subsequent passes remove 0.2-inch layers; roughing is continued until only 0.1 inch of material to be removed remains. The electronic grinder is set to speed 2 for roughing. Roughing takes about 45 minutes per section per pass.

An intermediate pass is next made using the finishing toolpath and a 1/16-inch ball-end endmill. The intermediate pass is offset 0.025 inches above the final surface. The grinder is set to speed 1 for the intermediate and finishing passes. The slower speed is necessary due to the reduced rate at which shavings are cleared from the flutes in the smaller endmills. (Shaving buildup causes the endmill to become hot.) The intermediate passes last about 5 hours per section.

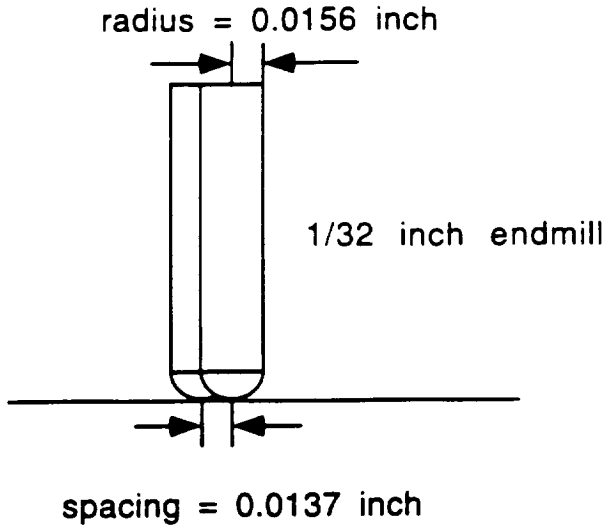

Figure 5.6: The spacing between adjacent finishing rows (0.0137 inch) was slightly less than the radius of the 1/32-inch ball-end endmill (0.0156 inches).

The edges are milled after the intermediate pass using the 1/16-inch endmill and the toolpath written for the edges. Two edge passes are completed: one with offset 0.1 inch, and another with an offset of 0.025 inches.

The finishing passes are run using a 1/32-inch ball-end endmill. The miniature endmills were purchased from R & F Micro Tool Co. of Pembroke, Massachusetts. Finishing passes last 5 hours as well. In milling test wood surfaces and the first UHMW surface, it was determined that often the surface material was not completely removed in the finishing passes. This was partially due to the limited overlap between adjacent rows when using the 1/32-inch ball-end tools (as shown in Figure 5.6), and partially due to the endmills becoming less sharp with use. The residue remaining could sometimes be pulled off in strips, but often it formed individual fibers that could be described as plastic "peach fuzz." Sanding, singeing, and brushing were tried in attempts to remove the fibers, but the procedure found to produce the fewest fibers was to make the initial 1/32-inch finishing pass in the cross direction (i.e., orthogonal

to the section's long dimension) using zero offset, followed by a lengthwise finishing pass (i.e., along the section) with a positive offset of 0.002 inches. This procedure reduced the fibers to acceptable levels.

Keeping the tools sharp was a constant task. The endmills tended to become dull quickly due either to the material or to the high rotation speed. Tool dullness was particularly troublesome with the 1/32-inch endmills, which have very little cutting area, and which need to be the most sharp. Some of these endmills seemed dull when new. After consulting with R & F Micro Tool, endmills coated with titanium nitride (TiN) were found to keep a sharp edge longer.

The finishing process was quite lengthy, with 28 section passes at 5 hours each. The mill ran unattended, but was checked by an operator every few hours. Three sections per day was the effective maximum rate of completion.

5.6 Surface Completion and Temperature Sensitivity

Programming and testing of the upgraded system continued through September 1993. Improvements during this period included the addition of a blower fan to keep the z-axis motor cool and optimization of mill travel speeds for roughing, intermediate, and finishing passes. In late September, work was started on the first artificial surface, UHMW1.

A new problem appeared during the intermediate-scale milling on UHMW1. After noticing that the slab was slightly loose within the holding clamps early in the morning, a heat gun was used to heat the surface slightly. The slab soon became immobile, having expanded due to the increase in temperature. The thermal expansion and contraction became a significant problem in the milling process. When the temperature dropped, the slab became loose; when the temperature rose too high,

the slab bowed upward because the mounting brackets prevented lateral expansion. Either of these changes left visible ridges in the milled surface. The thermal contraction and expansion tended to lag behind the room temperature by several hours. A heat lamp and space heater were tried as means of keeping the surface warm, but neither could keep the slab at a constant temperature. In October, the steam supply to the room heater was turned on, but the radiator was unable to keep the room above 20 °C at night even at its maximum setting. (The milling machine was located in room 422-4 in the Aerospace Engineering Building; this room is quite large with a 20-foot ceiling and has windows on three sides which are poorly sealed.)

The ambient temperature had been 24–27 °C when the surface was first mounted; maintaining this temperature became more difficult as outside temperatures fell through October. After repeated maintenance work on the room heater and improved sealing on the windows failed to help, a cubical enclosure ("the Greenhouse") was constructed from light wood and plastic sheeting around the milling machine. A compact electric heater with thermostat and a blower fan were placed inside in an attempt to stabilize the the temperature. The electric heater could not maintain an 80 °F air temperature around the clock, but it did provide sufficient heat during the day to allow UHMW1 to be completed on 19 November. A verification scan was performed on the surface before removing it from the mounting clamps. The scan is described in the next section.

Milling on UHMW2 began on 11 March 1994 and was completed on 14 April. Temperature stability was less problematic because the milling was started at a lower temperature that was maintainable by the electric heater.

The milling machine was moved to room 422-15 before starting UHMW3 on 14 June. Room 422-15 had an air conditioner, which was necessary to avoid slab

expansion due to overheating. UHMW3 was completed on 9 July.

5.7 Surface Verification

After each surface was completed, the electronic grinder was removed and a small ranging laser mounted on the milling machine. The new laser, which was purchased to replace the surveying laser used in Chapter III, produced elevation measurements over a limited range at a very rapid rate. The laser generated an output voltage proportional to the measured distance; this voltage was read by a sampling multimeter and relayed to the 486 computer through an HP-IB link. The surface scanning program, `millscan`, was written in Visual Basic and was quite similar to the milling program.

The laser beam was carefully adjusted to be vertical and was aligned as closely as possible to the origin of the milled surface. The surface scan consisted of 264 $\times$ 264 points with a point spacing equal to five times the point spacing used in the original surface specification. The elevation at each point was based on the average of 100 samples measured at two-millisecond intervals.

An error estimate was calculated by subtracting the scanned elevations from the elevations specified in the original surface file. The error estimate from UHMW1 is shown in grayscale in Figure 5.7. No systematic features are visible in the file. The surface in the figure is actually a subset of the error estimate; several rows around the edge were removed because the laser range estimates were visibly wrong near the mounting brackets. The corrupted readings were most likely due to the angled orientation of the detector which senses the reflected laser light. This configuration seemed to decrease the laser accuracy on sloped surfaces, suggesting that the width of the error distribution (shown in Figure 5.8) was inaccurately large. The repeatability

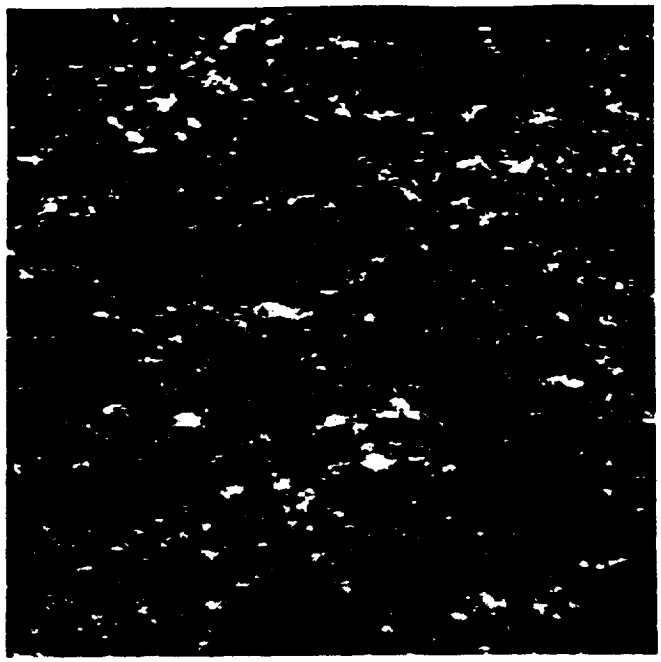

Figure 5.7: Grayscale file of estimated error in UHMW1, calculated by subtracting the scanned height from the specified height in the original surface file.

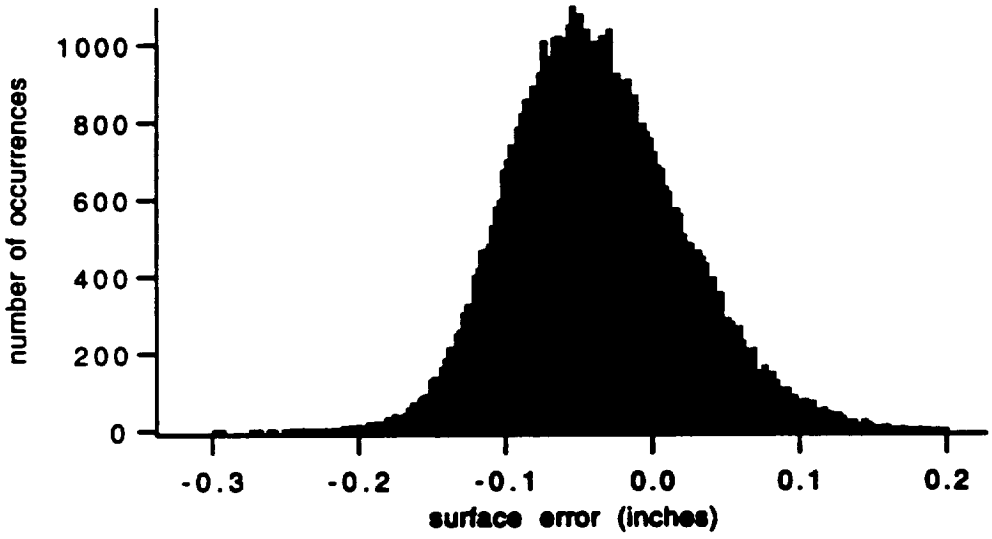

Figure 5.8: A histogram of differences between the specified surface elevations and the scanned surface height.

of the endmill position on the metal block position to within 3–6 steps (0.03–0.06 mm) after numerous milling sessions supports the hypothesis that errors in the milled surface elevations are below the resolution of the scanning laser.

Fabrication of the surface analogues was by far the most time-consuming part of this study. Measurements of radar backscatter from these surfaces is described in the next chapter.

CHAPTER VI

RADAR MEASUREMENTS

Backscatter from the artificial power-law surfaces was measured at 35 GHz using the Radiation Laboratory Millimeter-wave Polarimeter. Measured values of the scattering coefficients of the scaled surfaces were then interpreted as X-band scattering coefficients of equivalent larger-scale surfaces. (The scale factor turns out to be unity.)

In this chapter, the radar components and measurement configuration are described. The calibration and measurement algorithms are discussed, and final post-processing and data reduction steps are detailed.

6.1 35 GHz Radar

The Radiation Laboratory Millimeter-wave Polarimeter (MMP) was first assembled in 1986 [62] and was most recently rebuilt in 1994. The MMP is a dual-antenna, network-analyzer-based scatterometer designed for operation at 35 GHz. A phase-locked on-board local oscillator signal is mixed with the 2–4 GHz IF sweep received through cables from the network analyzer to produce a transmitted wave sweep from 34 to 36 GHz. The received signal is downconverted by mixing with the signal from a second local oscillator, resulting in a 2–4 GHz IF signal that is transmitted to the

network analyzer through coaxial cables. The transmit and receive local oscillators are phase-locked by split signals produced by an on-board X-band oscillator that are multiplied up to the LO frequency. Motorized rotating wave plates in the transmit channel allow the transmission of arbitrary polarizations, and separate horizontal (H) and vertical (V) receive channels allow the simultaneous measurement of H and V return signals when using a network analyzer with dual-channel reception capability. The transmit and receive assemblies may be separated for use as a bistatic radar. In addition, the removable transmitter module may be installed in the receiver assembly allowing monostatic operation using a single antenna. A block diagram of the radar is shown in Figure 6.1.

For this study, the radar was configured as a dual-antenna, quasi-monostatic instrument operating at the near edge of the far-field region. The transmit and receive antennas were installed adjacent to each other and offset by 4.8° so that the transmit and receive antenna boresights converge at the target range. The 3 dB product beamwidth was 3° and the 6 dB product beamwidth measured 4.2°. While the original radar specifications called for components with a bandwidth of 2 GHz, a slightly wider bandwidth of 2.4 GHz (33.6–36 GHz) was used for the measurements in this study.

An HP 8720 network analyzer was used to process the returned signals and translate them for output to a Gateway 2000 DOS-compatible computer. The HP 8720 was preferred over an HP 8753 because its frequency range allows input and output of signals up to 4 GHz, making IF sweeps of 2–4 GHz (or 1.6–4 GHz) possible. This advantage was offset by the test set of the HP 8720, which has only two ports, precluding reception of both V and H channels simultaneously. An external microwave switch was used to connect either the V or H receive channel to the network analyzer.

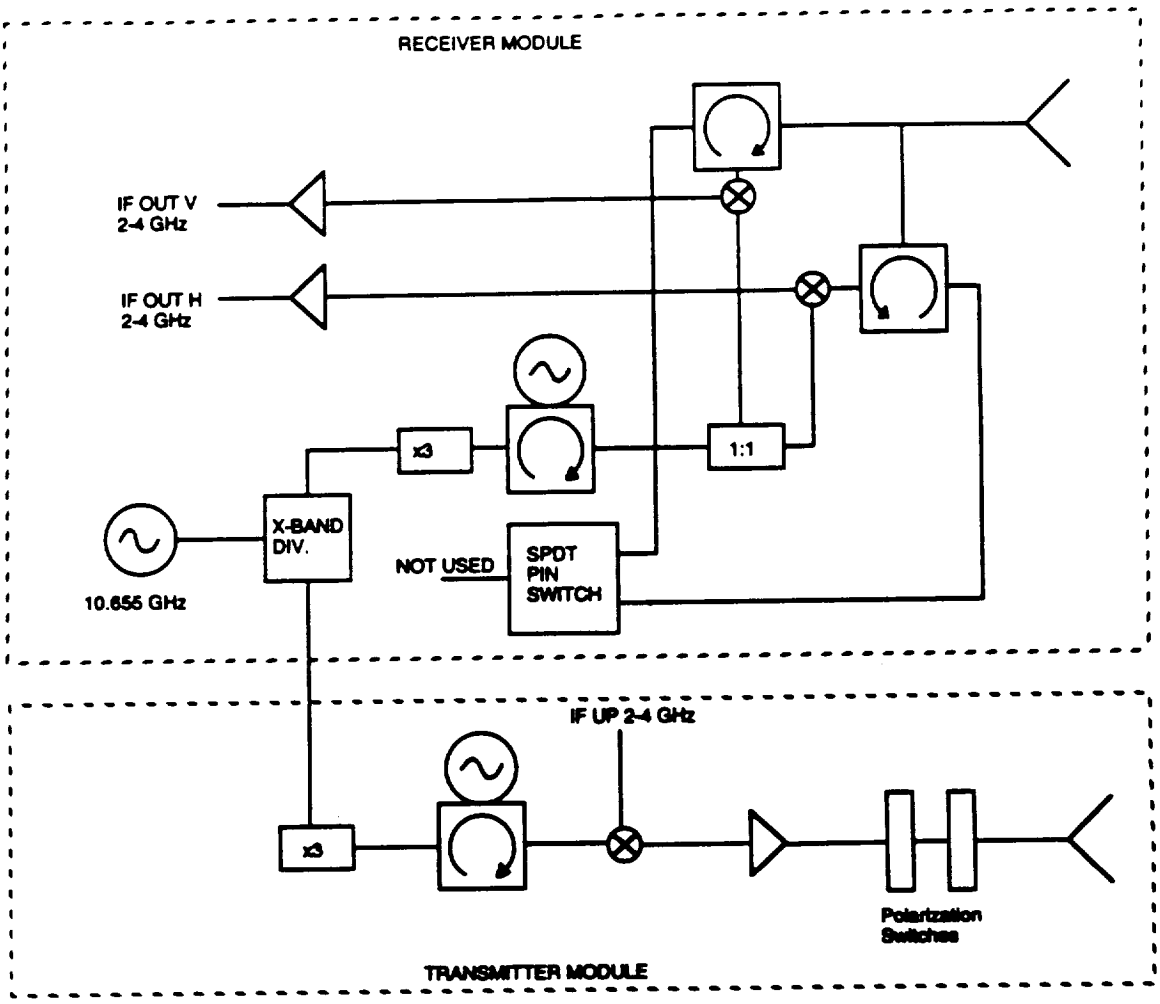

Figure 6.1: Block diagram of the 35 GHz radar.

This switch was operated by the computer using an HP 3488A switch/control unit.

The time-gating capability of the network analyzer allows the operator to isolate the response from a selected range interval in the time domain. This feature was used in the present study to mask out reflected signals from the bottom of the UHMW stack, the turntable, the wall behind the target, and other objects in the room, making accurate cross section measurements possible without an anechoic chamber.

The network analyzer, transmit polarization switches, receive channel switch, and target turntable were all controlled by a Gateway 2000 4DX2-66V DOS-compatible computer using control software written in Visual Basic. Raw and time-gated trace data were stored on the computer's hard disk drive. The radar and measurement control system is shown in Figure 6.2.

6.2 Measurement Configuration

The scattering measurements were performed in a side area of the Radiation Laboratory Bistatic Scattering Facility, Room 422-4, Aerospace Engineering Building. Figure 6.3 shows a measurement schematic.

The milled surface was placed atop an 18-inch stack of UHMW slabs (two 6-inch slabs on top of three 2-inch slabs) in order to increase the delay between the reflections from the top and bottom surfaces, allowing use of a time gate to isolate the upper surface reflection. The slabs were flat except for a small air gap around the edges of the two 6-inch slabs and a slightly larger air gap (maximum thickness: 1 mm) between the milled surface slab and the top of the UHMW stack. This larger air gap was due to a slight warping of the milled slab caused by the release of internal stresses during the milling process. A dielectric filler (Vaseline petroleum jelly, $\epsilon_r = 2.16 - j0.0022$ at 10 GHz [29]) was used to fill the air gaps. Plots of

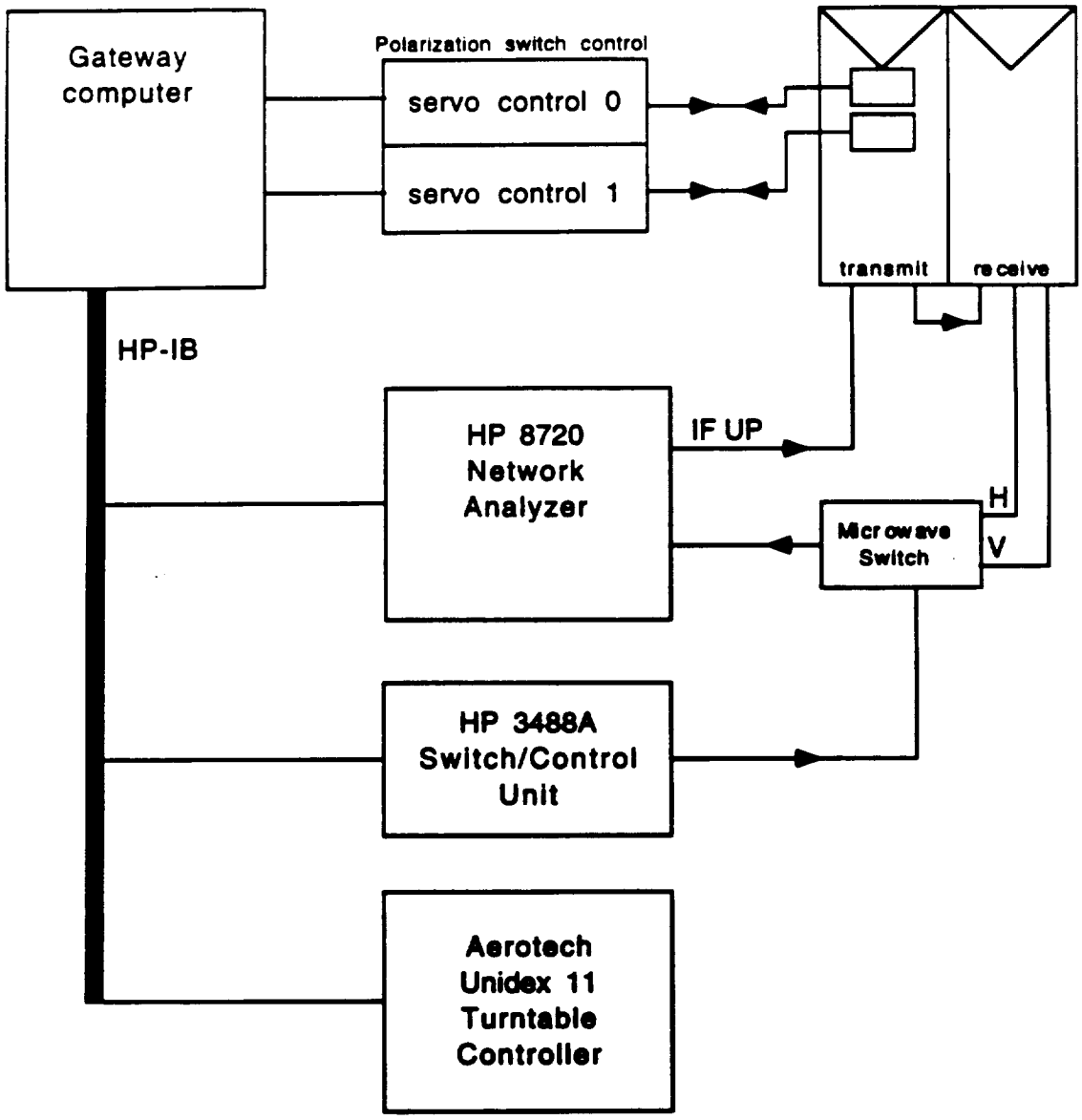

Figure 6.2: Components of the radar measurement system.

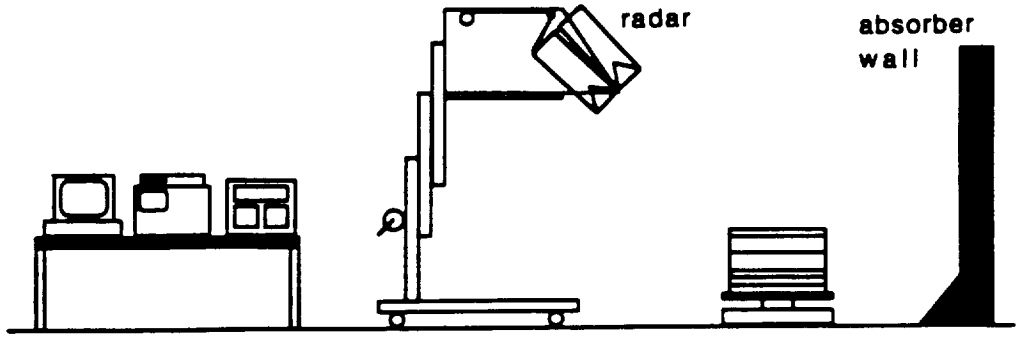

Figure 6.3: Schematic of measurement setup.

the time-domain response before and after applying the filler showed a reduction in reflections from the internal interfaces.

The UHMW stack was placed on a square piece of Eccosorb AN-PXP-74 foam absorber. Surfaces UHMW1 and UHMW2 were measured with the slab stack and absorber placed on the large turntable used for the sandbox in the bistatic system. A much smaller turntable was used for the UHMW3 measurement; a square of 1/4-inch plexiglass was placed between the turntable and absorber to increase stack stability.

The target turntable was placed about a meter in front of an absorber wall to eliminate reflections from the corner of the room. Other objects were removed so that the artificial surface was the sole object at target range near the main beam of the antenna. A large section of absorber was placed in possible sidelobe directions, but no significant reflections due to sidelobes were detectable.

The radar transmitter and receiver assemblies rotated about a front axis that was mounted on the front of a large steel frame. The incidence angle was adjusted by pivoting the radar around the front axis, using a small electric motor to reel in a cable attached to the rear plate of the receiver. The steel frame was attached to a manually operated, mechanically telescoping lift (a Genie Superlift, manufactured by Genie Industries of Redmond, Washington). The lift was used to raise the radar to

heights up to 3.5 m, making measurements at near-normal incidence angles possible.

The system had a high signal-to-noise ratio. The signal peak corresponding to a 1.75-inch sphere was about 58 dB above the noise level before calibration. Isolation between the co- and cross-polarized channels was about 25 dB before calibration and about 42 dB after calibration over most of the bandwidth.

6.3 Calibration

The radar was calibrated using a recent technique for polarimetric coherent-on-receive radar systems [46]. The technique uses two calibration targets (a metallic sphere and a depolarizing target) for the initial system calibration and a sphere alone for subsequent gain corrections. A 1.75-inch (4.445 cm) diameter steel sphere and a pair of 0.028 cm diameter × 5.4 cm lengths of wire mounted in styrofoam were used as the calibration targets for these measurements. The calibration technique is described in Appendix B.

The radar system stability needed to be established before measurements of scattering by the artificial surfaces could begin. Repeated calibrations using a sphere and depolarizing target were used to test system stability as reflected in the calibration coefficients. Several problems were fixed in order to get repeatable values for the time-invariant calibration constants c_1, c_2, c_3, τ_1, and τ_2:

- The use of trace subtraction to remove the response from the calibration target mount was discontinued because the mount position changed when placing or removing the calibration target. Fortunately, the scattering cross sections of the calibration targets were much higher than that of the styrofoam mount.

- A sturdier styrofoam column was used. The steel sphere used as a calibration target was heavy enough to compress and give a slight tilt to the original

styrofoam mount.

- A phase-lock problem was fixed by slightly changing the frequency of the X-band oscillator used to phase lock the two local oscillators.

- The radar temperature was stabilized, first by installing sheets of clear plastic to make the radar assembly near-airtight, and later by installing a heater inside the enclosure.

- The calibration target was allowed to settle for at least 15 minutes after placing it on the styrofoam target mount. Repeated tests indicated a non-visible sway introduced by placing the target (especially the heavy sphere) on even the sturdier styrofoam column. Target stability is particularly important while measuring c_1, c_2, c_3, τ_1, and τ_2; the settling period increased the repeatability of these factors.

- A minimum warm-up period of one hour was selected for both the radar and network analyzer.

These measures, together with more mundane practices like avoiding contact with the radar cables or mount, brought the system to a sufficient level of stability, as reflected in the time-invariant constants and the channel gains R_1 and R_2.

Test measurements of the calibration sphere (Figure 6.4) and a smaller sphere measuring 1.188 inches in diameter(Figure 6.5) showed that deviations from theoretical scattering cross sections were less than 0.5 dB (usually less than 0.3 dB) and that cross-polarized isolation was good, usually 40–45 dB or more. Although the system stability seemed good over fairly short periods, it was suspected that longer-term variations would be greater. A conservative approach of calibrating before and after

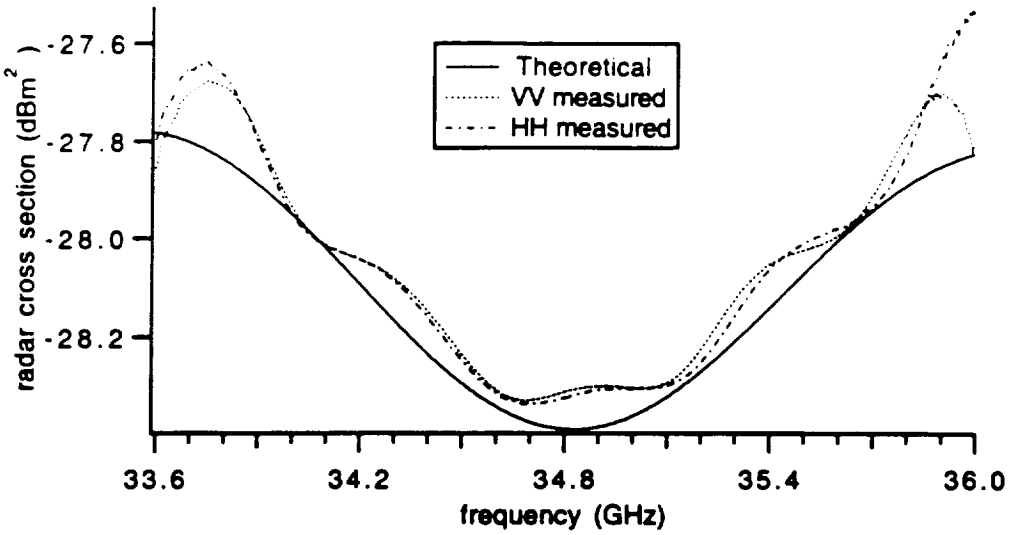

Figure 6.4: Test measurement of calibration sphere (1.75 inches in diameter).

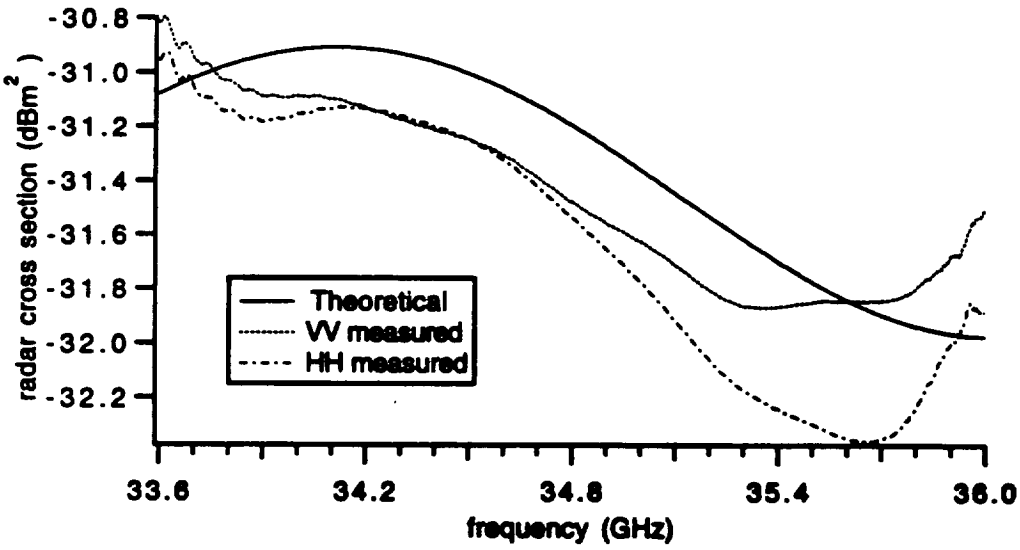

Figure 6.5: Test measurement of 1.188-inch diameter sphere.

each rough surface data set was adopted. During the processing of the measured data from UHMW1 and UHMW2, it was noticed that the magnitudes of R_1 and R_2 computed after a measurement run were slightly different from those measured before the run. The relative phases also varied as a function of frequency. Linear interpolation of the magnitudes and phases of R_1 and R_2 with time was used as a first-order correction to minimize the effect of the changing R parameters. Values of R_1 and R_2 for a given trace are based on linear interpolations computed with respect to the actual times of the previous and subsequent calibrations and the start and stop times of the measurement set. Test measurements in which the phases of R_1 and R_2 were 180° off showed that errors in σ were only about 0.6 dB; the linear-interpolation-based values should be considerably more accurate in phase.

6.4 Measurement Procedure

After characterizing the system by performing a full calibration to determine the time-invariant calibration coefficients, the UHMW stack was placed upon the turntable, and the surface to be measured was placed on the stack, as discussed in Section 6.2. Dielectric gel was used to fill in air gaps under the edges of the surface to be measured.

Before beginning measurement, the calibration sphere (1.75 inches in diameter) was placed on its mount. The radar was moved to the operating range for this study, 2.7 m. (The range was measured using a 2.7-meter length of wire attached to the radar faceplate.) After carefully peaking the sphere signal by adjusting the radar azimuth and elevation angles, a red targeting laser (attached below the receiver antenna) was adjusted to point at the center of the antenna beam at the operating range. The laser made later pointing much simpler.

The artificial surfaces were measured at incidence angles ranging from 15° to 60° at 5° increments. The measurement sequence at each incidence angle consisted of the following steps:

- with radar lowered, set incidence angle, θ
- set h, radar height, and d, distance from lift base to target surface
- raise radar in elevation to point at sphere and calibrate
- reset incidence angle, θ
- raise back to height h and position using target laser and range wires
- measure 60 samples of surface backscatter using VV, HV, VH, and HH polarizations, rotating the target 5° between measurements
- raise radar in elevation to point at sphere and recalibrate

A few additional sphere measurements were inserted between calibration sets.

6.5 Post-Processing and Data Reduction

During the measurement runs, raw trace data is saved to disk files in binary form for reasons of speed (it is much faster than saving gated data) and flexibility (the data may be gated later in various ways).

Gating refers to the process of transforming a frequency-domain data trace to the time domain; applying a time gate (i.e., a bandpass filter of specified width that is used to eliminate signals from objects at ranges outside the gate), and transforming the result back to the frequency domain. The network analyzer was set to its standard gate shape; the gate width was set to 5 ns in order to include reflections from both

near and far parts of the illuminated surface while excluding reflections from the bottom of the stack. The gate width was reduced to 4 ns for incidence angles of 25°, 20°, and 15° due to the smaller range difference between the closest and most distant surface points. The gate center was set at the mean target range, usually 18.01 ns.

After the surface and calibration target files have been gated, they are uploaded to a Unix workstation for further processing. Measurements of the calibration target are first converted into values of R_1 and R_2 as a function of frequency (i.e., for each of the 401 discrete frequencies that make up a data trace). Next, files of gated surface data are converted into average radar cross sections, σ, for each polarization as if the targets were point targets (rather than distributed targets) using

$$\sigma_{rt}(f_i) = \langle |2\sqrt{\pi} S_{rt}(f_i)|^2 \rangle, \tag{6.1}$$

where r and t indicate the receive and transmit polarizations and may be either V or H, and S_{rt} is an element of the scattering matrix given by (B.43). The angle brackets $\langle \cdot \rangle$ in (6.1) denote averaging over all traces in a set (i.e., over all surface measurements at various azimuth angles). Averaging is done separately for each of the 401 trace frequencies.

6.5.1 Scattering Coefficients

Values of the scattering coefficient $\sigma^0(f_i)$ are obtained by applying an illumination integral correction to $\sigma(f_i)$. The correction may be derived from the forms of the radar equation used for point and distributed targets. The point target form for a target at boresight is [62]

$$P_r(\theta) = \frac{P_t G_{0t} G_{0r} \lambda^2}{(4\pi)^3} \frac{1}{R^4} \sigma(\theta), \tag{6.2}$$

and the distributed target form is

$$P_r(\theta) = \frac{P_t G_{0t} G_{0r} \lambda^2}{(4\pi)^3} I(h,\theta)\sigma^0(\theta), \tag{6.3}$$

where $I(h,\theta)$ is called the illumination integral:

$$I(h,\theta) = \int_{\text{Illum. area}} g_t(\theta_t,\phi_t) g_r(\theta_r,\phi_r) \frac{1}{R^4(\theta,\phi)} dA. \tag{6.4}$$

The illumination integral accounts for the variation in antenna gain and range across the distributed target. The illumination integral correction is obtained by setting the ratio $P_r(\theta)/P_t$ equal in (6.2) and (6.3) and solving for σ^0 in terms of σ:

$$\sigma^0(f_i) = \frac{1}{R^4 I(h,\theta)} \sigma(f_i). \tag{6.5}$$

The program `measillum.f` was used to convert values of $\sigma(f_i)$ to values of $\sigma^0(f_i)$ for four polarizations at 401 frequencies per data set based upon the range and incidence angle for each measurement. Normalized antenna patterns were based upon data supplied by the manufacturer.

Final values of σ^0 were obtained by averaging over frequency. Errors in the measured cross section of test spheres were greatest at the upper and lower ends of the frequency band; frequencies outside the range 33.8–35.8 GHz were therefore omitted from the frequency averaging.

The values of the scattering coefficient were obtained using a surface model scaled for use with a 35 GHz radar instead of an X-band radar. Using Table 11-6 of Ruck [50], we see that the scaled quantities (denoted by primes) of length, conductivity, frequency, wavelength, permittivity, permeability, and radar cross section are related to the unscaled quantities as follows:

$$l' = l/p, \tag{6.6}$$

$$\sigma' = p\sigma, \quad \text{(conductivity)} \tag{6.7}$$

$$f' = pf, \tag{6.8}$$

$$\lambda' = \lambda/p, \tag{6.9}$$

$$\epsilon' = \epsilon, \tag{6.10}$$

$$\mu' = \mu, \tag{6.11}$$

$$\sigma' = \sigma/p^2, \quad \text{(radar cross section)} \tag{6.12}$$

where p is the scale factor (3.538 in this study). The conductivity scaling is not a problem because UHMW has negligible conductivity.

The scale relation for the scattering coefficient of a distributed target, σ^0, is obtained by noting that the surface area, A, scales as length squared:

$$A' = (l')^2 = \left(\frac{l}{p}\right)^2 = \frac{A}{p^2}. \tag{6.13}$$

Writing the scattering coefficient as the average radar cross section normalized by area, we obtain

$$(\sigma^0)' = \frac{\langle\sigma'\rangle}{A'} = \frac{\langle\sigma/p^2\rangle}{A/p^2} = \frac{\langle\sigma\rangle}{A} = \sigma^0. \tag{6.14}$$

Because σ^0 is a normalized quantity, it is independent of the model scale.

6.5.2 Independent Samples

Independent samples of the surface scattering were obtained through a combination of target rotation, spatial sampling, and frequency averaging. The radar 6-dB footprint was positioned as close to the surface edge as possible to minimize overlap between footprints (Figure 6.6). Overlap of the 3-dB footprints was smaller still. The surface was rotated 5° between measurements. A few measurement runs were executed using smaller angular increments, $\Delta\phi$, in order to study the decorrelation as a function of target rotation. Based on limited angular decorrelation sets,

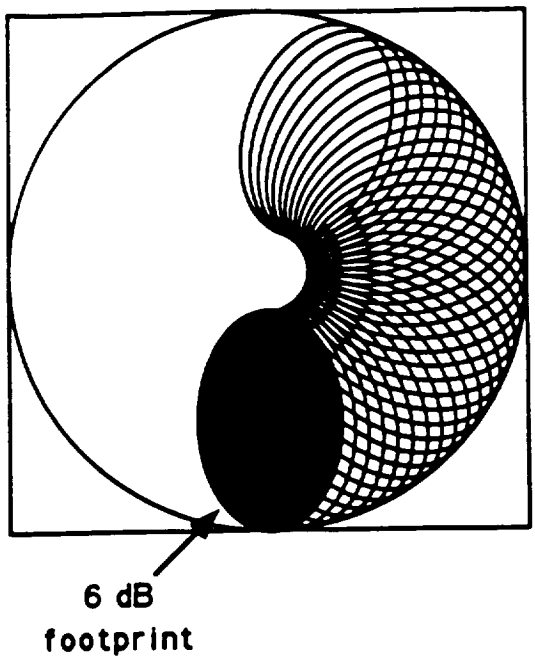

Figure 6.6: Arrangement of footprints on slab

decorrelation angles for UHMW3 are approximately 1.1° for 60° incidence and 4.5° for 15° incidence (based on 60-sample traces with $\Delta\phi = 0.5°$). For UHMW1, the decorrelation angle is approximately 1.5° for 60° incidence (based on a 90-sample trace with $\Delta\phi = 2°$). A data set with fine angular increments was not taken on UHMW1 at 15° incidence, but estimates based on the regular data sets indicate a higher decorrelation angle, though probably still less than 10°. No decorrelation sets were collected on UHMW2. The number of independent samples obtained through surface sampling N_{ss} therefore varied from 300°/7.5° = 40 (estimate for UHMW1 at 15°) to 60 (the number of samples collected) for UHMW1 at 60° and UHMW3 at all incidence angles.

Values of σ^0 were averaged over a 2 GHz bandwidth, increasing the effective number of independent samples by a factor dependent on the footprint's extent in range. Ulaby et al. [57] give an expression for the effective number of independent samples obtained through continuous integration over a swept-frequency bandwidth

surface	θ	N_{ss}	N_{favg}	N_{total}
UHMW1	15°	40 (est.)	1.3	52
	60°	60	5.1	306
UHMW3	15°	60	1.3	78
	60°	60	5.1	306

Table 6.1: Estimated number of independent samples

B:

$$N_{favg} = \frac{B}{2}\left[\int_0^B \left(1 - \frac{\xi}{B}\right)\left(\frac{\sin \alpha\xi}{\alpha\xi}\right)^2 d\xi\right]^{-1}, \tag{6.15}$$

where $\alpha = 2\pi D/c$ and D is the difference in range between the nearest and most distant points in the radar footprint. Using the dimensions and bandwidth from the present study, N_{favg} can be shown to vary from 1.3 at 15° incidence to 5.1 at 60° incidence.

The total number of independent samples, N_{total}, is calculated by multiplying the numbers gained by spatial sampling and frequency averaging:

$$N_{total} = N_{ss} N_{favg} \tag{6.16}$$

The resulting numbers are listed in Table 6.1. Values of N_{total} for UHMW2 were probably slightly lower than those of UHMW3 due to decreased roughness.

Values of the backscattering coefficient measured for the three surfaces are given in Chapter VII.

VI A Comparison with Various Scattering Models

There are no theoretical scattering models for random surfaces which have significant surface roughness at spatial scales that are near to the wavenumber of the scattered signal. The Phased Wiener-Hermite (PWH) model had never been tested and there was reason to believe that it might yield better approximations to scattering by power-law surfaces. In fact, the PWH model did not do well. Of the common theories that were tested under this investigation, the Small Perturbation Model performed best.

The comparison among theories and experimental scattering results became Chapter VII in R.T. Austin's Ph.D. dissertation [69]. These results will also appear in a TGARS paper. Chapter VII of Dr. Austin's thesis appears on the following 14 pages.

CHAPTER VII

ROUGH SURFACE SCATTERING MODELS AND COMPARISONS TO EXPERIMENT

The surface scattering measurements described in the previous chapter were performed in May and July of 1994. In this chapter, results of those measurements are shown and compared to predicted values of σ^0 resulting from several rough surface scattering models.

7.1 Experimental Results

Measured values of σ^0_{vv} and σ^0_{hh} for the three artificial surfaces are shown in Figure 7.1. The open symbols represent VV polarization and the filled symbols represent HH. Backscatter dependence on the surface roughness behaves as expected, with the roughest surface (UHMW1) having the highest backscatter, followed by the intermediate surface (UHMW3) and the smoothest surface (UHMW2). The backscattering coefficient decreases with increasing incidence angle for all three surfaces, as expected, although there is a small upturn in σ^0 values for both polarizations at 5.5° for the two smoother surfaces. There is little difference between the σ^0_{vv} and σ^0_{hh} for a given surface—σ^0_{vv} is usually slightly higher, but never more than a couple of decibels. The difference becomes small at small incidence angles, as it should.

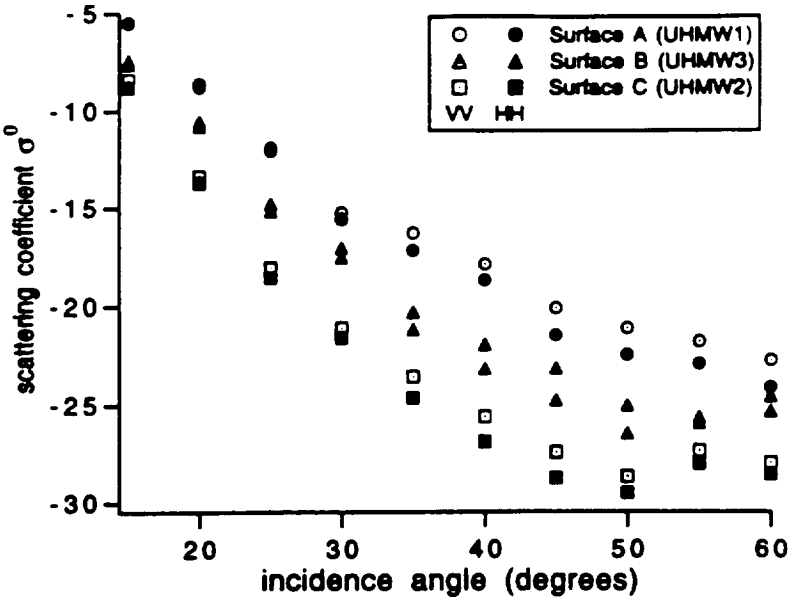

Figure 7.1: Measured co-polarized backscattering coefficients, σ^0_{vv} and σ^0_{hh}, of the three artificial surfaces: Surface A (UHMW1), $D_f = 2.355$; Surface B (UHMW3), $D_f = 2.2275$; and Surface C (UHMW2), $D_f = 2.1$.

Measured values of the cross-polarized backscatter, σ^0_{vh} and σ^0_{hv}, are shown in Figure 7.2. The measured σ^0_{hv} and σ^0_{vh} also follow expected trends, decreasing with increasing incidence angle, and decreasing for smoother surfaces. The measured values are generally 20–23 dB lower than the co-polarized backscattering coefficients. Values of σ^0_{vh} and σ^0_{hv} are roughly equal, with the exception of a couple of anomalous points for surface UHMW1 (the roughest surface) at low incidence angles. The backscattering coefficients seem somewhat noisier in the cross-polarized case. Because there was no test target that allowed easy and direct verification of measurement accuracy for cross-polarized returns, it is difficult to state probable measurement errors for σ^0_{vh} and σ^0_{hv}.

7.2 Comparison to Physical Optics Model

The Kirchhoff or physical optics model is one of the most widely used surface scattering models [59]. The Kirchhoff model represents the scattered field in terms

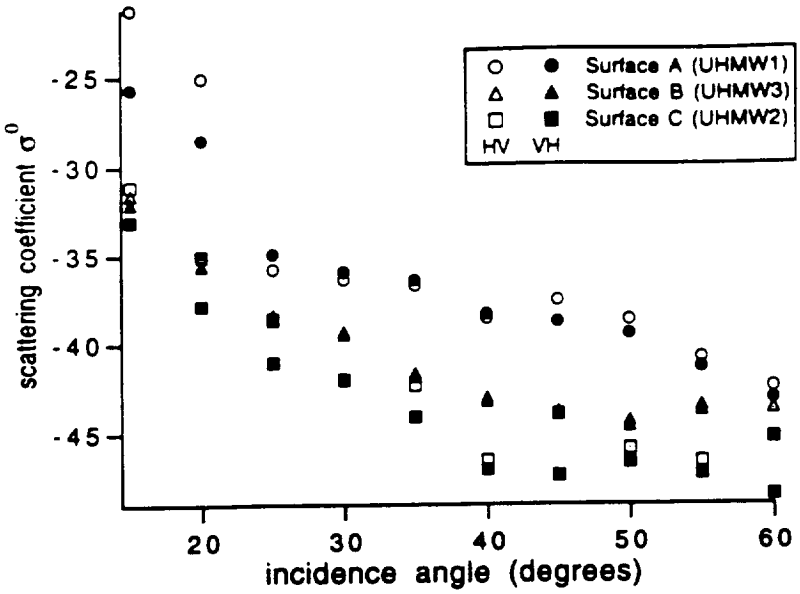

Figure 7.2: Measured cross-polarized backscattering coefficients, σ^0_{vh} and σ^0_{hv}, of the three artificial surfaces: Surface A (UHMW1), $D_f = 2.355$; Surface B (UHMW3), $D_f = 2.2275$; and Surface C (UHMW2), $D_f = 2.1$.

of the tangential field on the rough surface. It makes use of the tangent plane approximation to the surface field, in which the surface field at a point is approximated by the field which would be present if the rough surface were replaced by a planar surface tangential to the surface at that point [56]. The tangential plane approximation is valid if the radius of curvature at every point on the surface is large with respect to the radar wavelength. Use of the Kirchhoff model is usually limited to small incidence angles [14].

An additional simplification usually performed to make the physical optics solution more tractable is obtained by expanding the integrand of the scattered field integral into a series in terms of the surface slope and keeping only the lowest-order terms. This simplification is called the scalar approximation because it reduces to the scalar formulation of Beckmann and Spizzichino [5]; it requires that the radius of curvature be larger than the radar wavelength and that the rms surface slope be

small. Commonly cited constraints are [56]:

$$kl > 6 \tag{7.1}$$

$$R_c > \lambda \tag{7.2}$$

$$m < 0.25 \tag{7.3}$$

where k is the wavenumber of the incident field, l is the surface correlation length, R_c is the average radius of curvature of the surface, and m is the rms slope.

The scattering coefficient under the scalar approximation is given by [59]

$$\sigma^0_{pq} = \sigma^0_{pqc} + \sigma^0_{pqn} + \sigma^0_{pqs} \tag{7.4}$$

where the subscripts p and q indicate the scattered and incident polarizations and the subscripts c, n, and s indicate the coherent, non-coherent, and slope terms. For backscatter at non-normal incidence, we omit the coherent term.

The non-coherent term is given for the backscatter case by

$$\sigma^0_{ppn} = \frac{k^2}{\pi} \left\{ \begin{array}{c} |R_{\perp 0}|^2 \\ |R_{\parallel 0}|^2 \end{array} \right\} \cos^2\theta e^{-4k^2\cos^2\theta\sigma^2} \cdot \sum_{n=1}^{\infty} \frac{(4k^2\cos^2\theta\sigma^2)^n}{n!} I^{(n)}_{nc}(-2k\sin\theta, 0) \tag{7.5}$$

$$\sigma^0_{pqn} = 0 \tag{7.6}$$

where $R_{\perp 0}$ and $R_{\parallel 0}$ are the Fresnel reflection coefficients for horizontal and vertical polarization, respectively, and

$$I^{(n)}_{nc}(q_x, q_y) = \int_{-\infty}^{\infty}\int_{-\infty}^{\infty} \left(\frac{R_Z(u,v)}{\sigma^2}\right)^n e^{i(q_x u + q_y v)} du dv \tag{7.7}$$

For the power-law case, $R_Z(u,v)$ was calculated numerically from the modified roughness spectrum given by (5.8) using an inverse fast Fourier transform (FFT). The result was raised to the power n and then re-transformed to obtain $I^{(n)}_{nc}$.

The slope term σ^0_{pqs} was omitted for the power-law case because the non-analytical correlation function prevented the direct evaluation of the slope terms. The σ^0_{pqs} is much smaller than σ^0_{pqn} in the Gaussian case, so it is assumed that the term is of little consequence.

The physical optics results are compared with the measured σ^0 in Figure 7.3. The model values underestimate the measured backscatter by about 5 dB in the HH case, although they do follow the trend of the measured values out to about 45° or so.

The VV predictions start about 5 dB low at 15°, but rapidly grow worse due to the Brewster angle effect which the model has but which is not found in the measured data. The first-order physical optics formulation does not predict cross-polarized backscatter.

The roughness spectra used in the physical optics power-law solution had a low-frequency cutoff of $f_{lc} = (10\lambda)^{-1}$, where λ is the radar wavelength. The low-frequency cutoff was imposed due to programming constraints in the calculation of the $I^{(n)}_{nc}$ terms. Letting f_{lc} vary from $(5\lambda)^{-1}$ to $(25\lambda)^{-1}$ resulted in a change in σ^0 of less than 1 dB at 15° and still less at higher incidence angles.

7.3 Comparison to Geometric Optics Model

An alternative simplification to the Kirchhoff formulation involves the use of the stationary phase approximation, which means that scattering can occur only along directions for which there are specular points on the surface [59]. This high-frequency solution is valid when the average radius of curvature and the surface standard deviation are large compared to the radar wavelength. Commonly cited

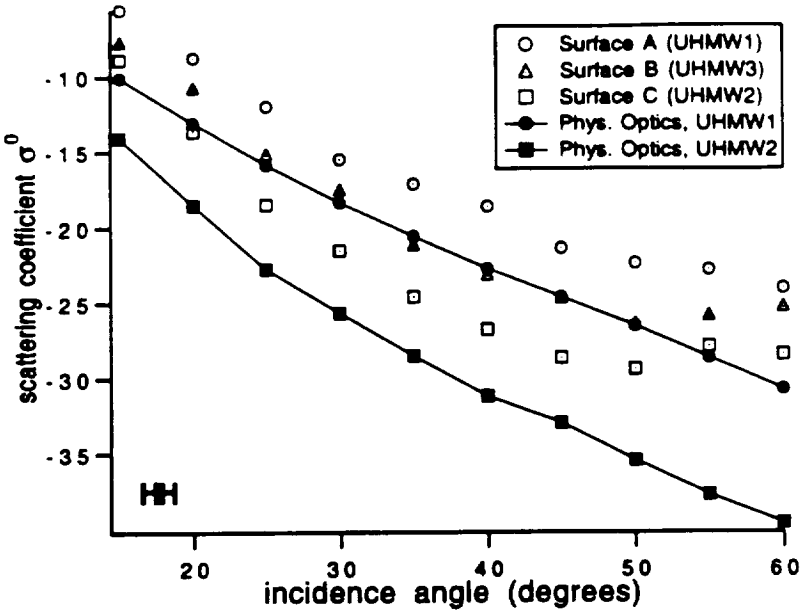

(a)

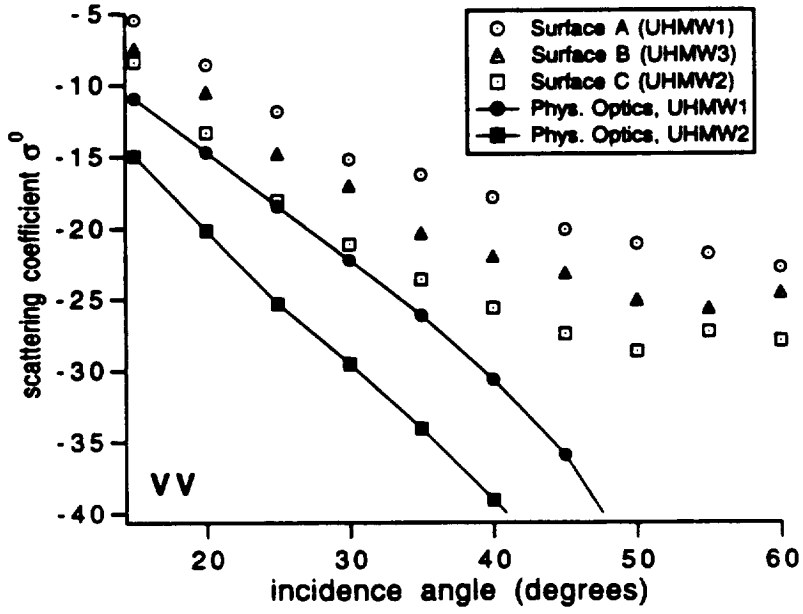

(b)

Figure 7.3: Physical optics results for (a) HH and (b) VV backscatter compared to the measured values for the three artificial surfaces.

criteria for this solution are [56]

$$kl > 6 \tag{7.8}$$

$$R_c > \lambda \tag{7.9}$$

$$k\sigma > \frac{\sqrt{10}}{\cos\theta_i - \cos\theta_s} \tag{7.10}$$

where σ is the standard deviation of surface height, θ_i and θ_s are the incident and scattered angles, and k, l, R_c, and λ are defined as before.

The geometrical optics solution is given by Ulaby et al. [59]:

$$\sigma^0_{pp} = \frac{|R(0)|^2}{2\cos^4\theta\sigma^2|\rho''(0)|} \tag{7.11}$$

$$\sigma^0_{pq} = 0 \tag{7.12}$$

where R is the Fresnel reflection coefficient and $\rho''(0)$ is the second derivative of the normalized correlation function, $\rho(\tau)$,

$$\rho(\tau) = \frac{R_Z(\tau)}{\sigma^2}, \tag{7.13}$$

evaluated at zero.

It is the $\rho''(0)$ term that provides the main difficulty in applying (7.11) to the power-law case. Because the power-law correlation function has no analytical form, it must be evaluated numerically at discrete points. A discrete approximation was used to evaluate $\rho''(0)$:

$$\begin{aligned} \rho''_0 &\approx \frac{\rho'_1 - \rho'_0}{\tau_1 - \tau_0} \\ &= \frac{1}{\Delta}\left(\frac{\rho_2 - \rho_1}{\Delta} - \frac{\rho_1 - \rho_0}{\Delta}\right) \\ &= \frac{1}{\Delta^2}(\rho_2 - 2\rho_1 + \rho_0) \end{aligned} \tag{7.14}$$

where the first three correlation values ρ_0, ρ_1, and ρ_2 are numerically calculated using the same bandlimited spectrum used for the physical optics case. For the three

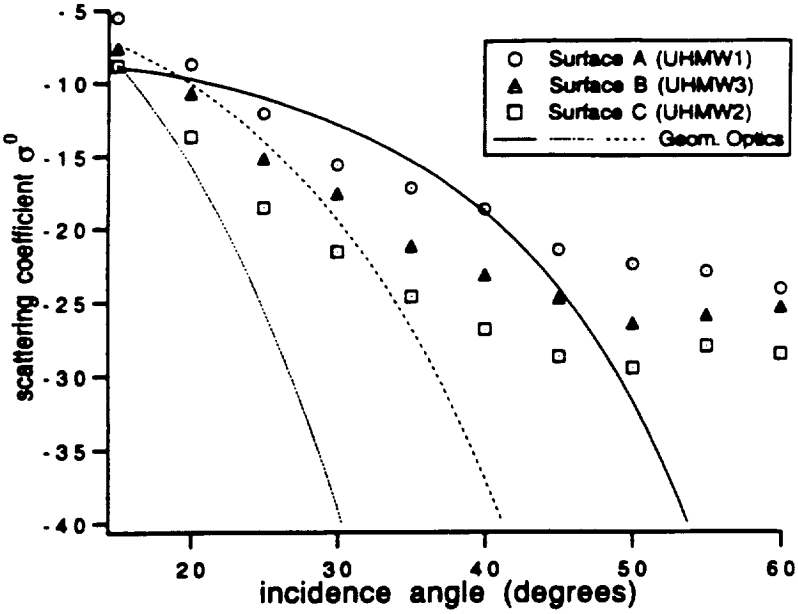

Figure 7.4: Geometrical optics results for backscattering compared to the measured values for the three artificial surfaces.

artificial surfaces, $\Delta = 1.23$ mm, and estimates of the rms slope, $m = \sqrt{\sigma^2|\rho''(0)|}$, were 0.31, 0.13, and 0.20.

The geometrical optics results are compared with the measured backscatter in Figure 7.4. The model performs quite poorly for the power-law surfaces.

7.4 Comparison to Small Perturbation Model

The small perturbation model was first applied to electromagnetic scattering by Rice [49], who used the Rayleigh hypothesis to represent the scattered and transmitted fields near a rough surface in terms of waves traveling away from the surface only. These fields are expanded in a power series about some small parameter such as surface height or slope. The fields are then calculated to some low order, usually first order, by neglecting series terms of higher order [56]. Validity limits on the small perturbation model are

$$k\sigma < 0.3, \tag{7.15}$$

$$m < 0.3, \tag{7.16}$$

where σ, the standard deviation of surface elevation, is computed "from frequency components of the surface responsible for scattering at a given electromagnetic wavelength" [59]. The small perturbation model is usually used for larger incidence angles ($\theta_i > 20°$) [14]. In a study of non-Gaussian surfaces by Chen et al. [15], the authors found that the small perturbation model has a wider range of validity when applied to a surface with a non-Gaussian (in their case, exponential) correlation function for large angles of incidence.

The first-order small perturbation model solution for the backscatter case is given by

$$\sigma^0_{pq} = 8k^4\sigma^2\cos^4\theta|\alpha_{pq}|^2 W(2k\sin\theta, 0), \tag{7.17}$$

where

$$\begin{aligned}
\alpha_{hh} &= R_\perp(\theta), \\
\alpha_{vv} &= (\epsilon_r - 1)\frac{\sin^2\theta - \epsilon_r(1+\sin^2\theta)}{[\epsilon_r\cos\theta + (\epsilon_r - \sin^2\theta)^{1/2}]^2}, \\
\alpha_{vh} &= \alpha_{hv} = 0,
\end{aligned}$$

and $W(k_x, k_y)$ is the normalized roughness spectrum,

$$W(k_x, k_y) = \frac{1}{2\pi}\int_{-\infty}^{\infty}\int_{-\infty}^{\infty}\rho(u,v)\exp[-j(k_x u + k_y v)]dudv \tag{7.18}$$

which is written in terms of the normalized surface correlation, $\rho(u,v)$. The Fourier transform in (7.18) uses a different form than that used elsewhere in this dissertation, where the non-normalized correlation function, $R_Z(\tau_x, \tau_y)$, is defined as

$$R_Z(\tau_x, \tau_y) = \int_{-\infty}^{\infty}\int_{-\infty}^{\infty} S_Z(f_x, f_y)\exp[j2\pi(f_x\tau_x + f_y\tau_y)]df_x df_y. \tag{7.19}$$

The normalized spectrum $W(k_x, k_y)$ with k_x and k_y in rad/m is therefore

$$W(k_x, k_y) = \frac{1}{2\pi\sigma^2}S_Z\left(\frac{k_x}{2\pi}, \frac{k_y}{2\pi}\right), \tag{7.20}$$

and we see that

$$W(2k\sin\theta, 0) = \frac{1}{2\pi\sigma^2} S_Z\left(\frac{k\sin\theta}{\pi}, 0\right), \tag{7.21}$$

and therefore

$$\sigma^0_{pq} = 8k^4\cos^4\theta|\alpha_{pq}|^2\frac{1}{2\pi}S_Z\left(\frac{k\sin\theta}{\pi}, 0\right), \tag{7.22}$$

where the spectrum, S_Z, is given by (5.8) or an equivalent expression. Note that the σ^2 term drops out of the final SPM equation.

The SPM results are shown in Figure 7.5 along with the measured backscatter. The SPM values track the measured data trends fairly well but have a negative offset of about 5 dB. In spite of this offset, the SPM results are the most useful of any of the models examined thus far. Because the SPM values are calculated based on a single frequency of the roughness spectrum, the offset cannot be attributed to an incorrect bandwidth choice. Because an error in the dielectric measurement was possible, different values of ϵ_r were tried. Changing ϵ_r from 2.05 to 2.3 raised σ^0 by about 1 dB. Errors in the ϵ_r measurement of more than 0.3 are considered extremely unlikely. Adding an imaginary component of $\epsilon''_r = 2$ raises σ^2 by about 5 dB, but it is difficult to believe that the UHMW or the dielectric filler has a lossy part that is so radically different from tabulated values. In the absence of other explanations, the offset in the SPM predictions is viewed as a limitation of the model in the power-law case.

7.5 Comparison to PWH model

The last model examined is the Phased Wiener-Hermite (PWH) model for dielectric interfaces by Eftimiu [16], which is an extension of earlier work by Eftimiu [17, 18, 19] and Eftimiu and Pan [20]. The model, which is relatively recent and which had no experimental verification, is based on an expansion of the surface

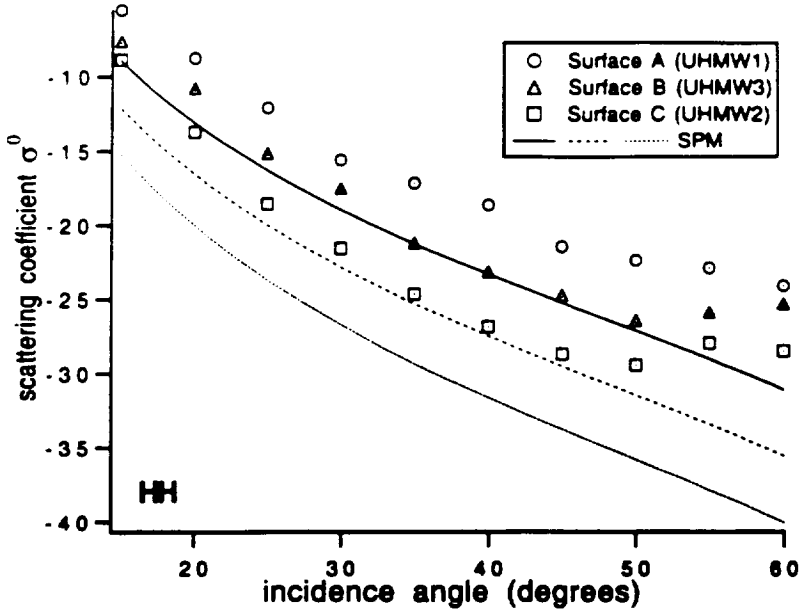

(a)

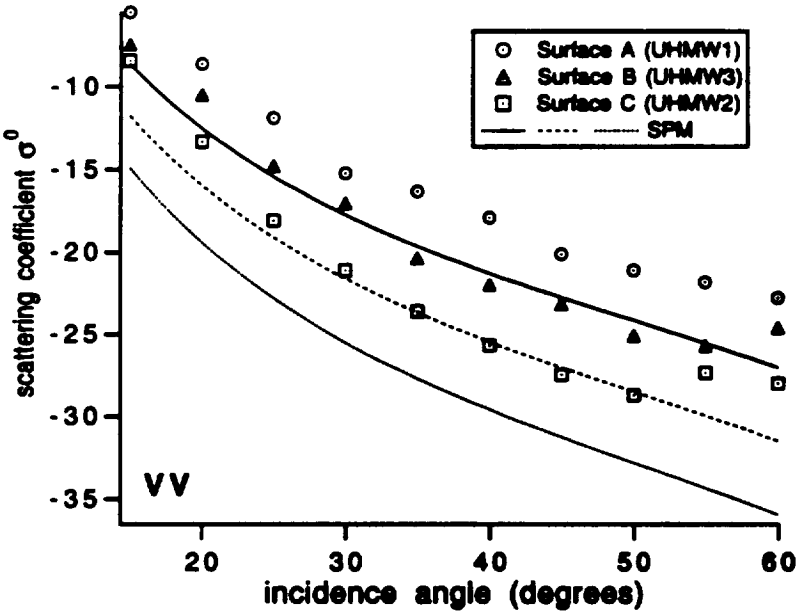

(b)

Figure 7.5: Small perturbation model results for (a) HH and (b) VV backscatter compared to the measured values.

current in a series of orthogonal Wiener-Hermite functionals. Earlier uses of Wiener-Hermite functional expansions in the study of turbulence led to their application to the problem of rough surface scattering by Nakayama et al. [41, 42, 43] and Meecham and Lin [38], among others. The expansion is attractive because it represents the surface current in terms of functionals based on the rough surface random process, $\zeta(x,y)$, and because lower-order terms in the expansion contain reflections of all orders [38]. An overview of the PWH model is the subject of Appendix C.

The PWH formulation is algebraically intensive in comparison with the other models in this chapter, perhaps because it relies on few simplifying assumptions. Aside from use of the Wiener-Hermite functional expansion (and the assumption that a first-order expansion is adequate), Eftimiu's formulation uses the extinction theorem and the tangentiality of surface currents. The formulation is shown to reduce to the physical optics and small perturbation solutions in the appropriate limits. The PWH expression for σ^0 is rather lengthy and involves a number of intermediate terms, and is therefore left in the Appendix.

The PWH solutions for σ^0 of the three surface analogues are shown for HH and VV polarizations in Figure 7.6. The modeled σ^0_{hh}, which were calculated using the bandlimited roughness spectrum truncated at $f_{lc} = (10\lambda)^{-1}$, display a more-or-less linear dependence on incidence angle and predict higher backscattering for the rougher surfaces. However, the theoretical curves do not match the measured values very well, either in magnitude, difference between the rougher and smoother surfaces, or in angular trends. Recalculations in which a wider roughness spectrum (down to $(25\lambda)^{-1}$) was used resulted in rough and smooth σ^0 values that were closer together in magnitude, but the values overestimated the measured values worse than in the narrower spectrum case. Values of σ^0_{vv} were closer, differing from the measured

values by 6 dB or less. The trends of σ^0_{vv} vs. θ are closer than those of σ^0_{hh}, but still not as close as those predicted by the small perturbation method.

While there are no obvious flaws in the PWH approach, one can imagine several possible reasons why the model performs poorly in the power-law case. The algebraic complexity of the model is quite high, increasing the probability of mathematical or programming errors. (The cited articles by Eftimiu contained numerous typographical errors; the author was supplied with a copy of Eftimiu's derivation notes to aid in reproducing the derivations.) The model requires the evaluation of a number of double integrals. These may be analytically reduced to one dimension in the Gaussian case but not in the power-law case, where the dynamic range (several orders of magnitude) may introduce problems in numerical precision. Finally, the power-law surface may simply be too complex to represent by a first-order Wiener-Hermite expansion, due to the presence of surface structure over a wide range of spatial scales.

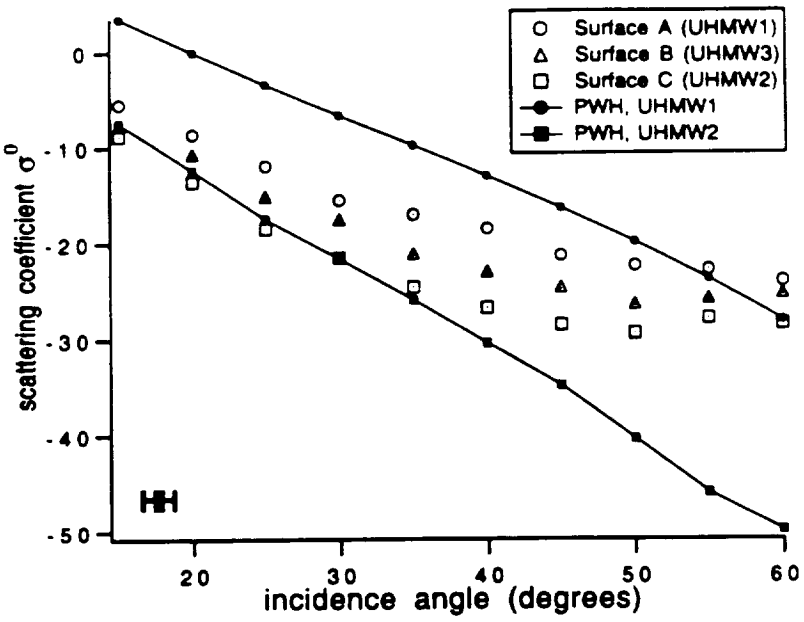

(a)

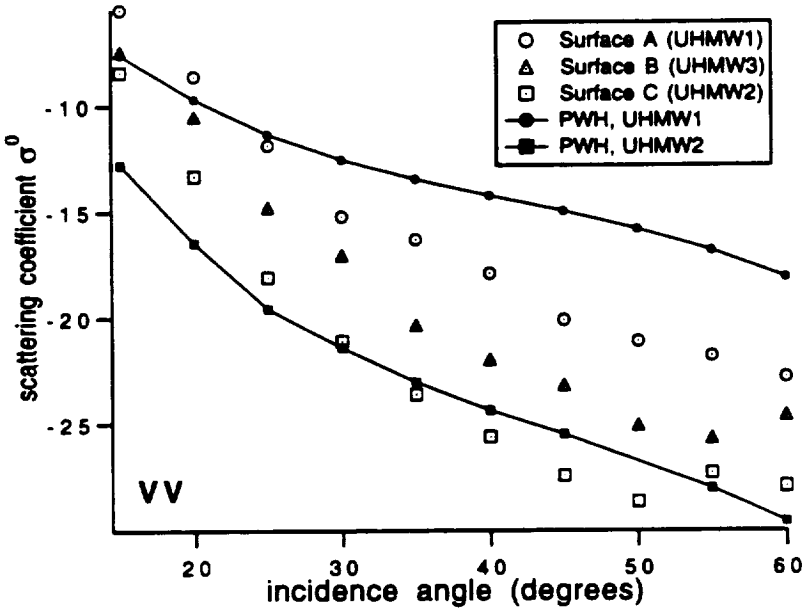

(b)

Figure 7.6: Phased Wiener-Hermite model results for (a) HH and (b) VV backscatter for the roughest and smoothest surfaces compared to the measured values.

VII Continuing Work

Empirical laws or, to a limited extent, small perturbation theory can be used to relate β and c in equation (1) to scattering cross section. We are currently testing this approach by developing a classification algorithm from the empirical laws discussed in Section V. Using this algorithm, we will attempt to classify Andean Volcanics according to their roughness. This application is funded by a SIR-C project and was not a part of our Mars investigation.

VIII Acknowledgement

Dr. Austin and I wish to thank the NASA Planetary Science Program for its support of our work. While the issues are not exhausted, we believe that we have made significant progress toward a quantitative examination of the diffuse component of Mars radar backscatter.

IX References.

[1] R.J. Adler. *The Geometry of Random Fields*, New York: Wiley, 1981.

[2] Richard T. Austin and Anthony W. England, "Multi-Scale Roughness Spectra of Mount St. Helens Debris Flows," *Geophysical Research Letters*, vol. 20, pp. 1603-1606, 1993.

[3] Richard T. Austin, Anthony W. England, and Gregory H. Wakefield, "Special Problems in the Estimation of Power-Law Spectra as Applied to Topographical Modeling," *IEEE Transactions on Geoscience and Remote Sensing*, vol. 32, pp. 928-939, 1994.

[4] Bateman Manuscript Project, *Tables of Integral Transforms*, vol. 2, A. Erdèlyi, Ed. New York: McGraw-Hill, 1954.

[5] P. Beckmann and A. Spizzichino, *The Scattering of Electromagnetic Waves from Rough Surfaces*. Oxford: Pergamon Press, 1963.

[6] T.H. Bell, Jr., "Statistical features of seal-floor topography," *Deep-Sea Research*, vol. 22, pp. 883-892, 1975.

[7] T.H. Bell, Jr., "Mesoscale sea floor roughness," *Deep-Sea Research*, vol. 26A, pp. 65-76, 1979.

[8] M.V. Berry and J.H. Hannay, "Topography of Random Surfaces," *Nature*, vol. 273, p. 573, 1978.

[9] R.B. Blackman and J.W. Tukey," The *Measurement of Power Spectra from the Point of View of Communications Engineering*. New York: Dover, 1958.

[10] S.R. Brown and C.H. Scholz, "Broad bandwidth study of the topography of natural rock surfaces," *Journal of Geophysical Research*, vol. 90, pp. 12 575- 12 582, 1985.

[11] Fred M. Bullard, *Volcanoes of the Earth*, 2nd edition. Austin: University of Texas Press, 1984.

[12] R.H. Cameron and W.T. Martin, "The Orthogonal Development of Non-linear Functionals in Series of Fourier-Hermite Functionals," *Annals of Mathematics*, vol. 48, pp. 385-392, 1947.

[13] J. Capon, "High-Resolution Frequency-Wavenumber Spectrum Analysis," *Proceedings of the IEEE*, vol. 57, pp. 1408-1418, August 1969.

[14] M.F. Chen and A.K. Fung, "A numerical study of the regions of validity of the Kirchhoff and small-perturbation rough surface scattering models," *Radio Science*, vol. 23, pp. 163-170, 1988.

[15] M.F. Chen, S.C. Wu, and A.K. Fung, "Regions of Validity of Common Scattering Models Applied to non-Gaussian Rough Surfaces," *Journal of Wave-Material Interaction*, vol. 2, pp. 9-25, 1987.

[16] Cornel Eftimiu, "Scattering by a rough dielectric interface: A modified Wiener-Hermite expansion approach," *Journal of the Optical Society of American A*, vol. 7, pp. 875-884, May 1990.

[17] Cornel Eftimiu, "First-order Wiener-Hermite expansion in the electromagnetic scattering by conduction rough surfaces," *Radio Science*, vol. 23, pp. 769-779, September/October 1988.

[18] Cornel Eftimiu, "Second-order Wiener-Hermite expansion in the electromagnetic scattering by conducting rough surfaces," *Radio Science*, vol. 23, pp. 1075-1084, November/December 1988.

[19] Cornel Eftimiu, "Modified Wiener-Hermite expansion in rough-surface scattering," *Journal of the Optical Society of America A*, vol. 6, pp. 1584-1594, October 1989.

[20] Cornel Eftimiu and G.W. Pan, "First-order Wiener-Hermite expansion in the electromagnetic scattering by dielectric rough interfaces," *Radio Science*, vol. 25, pp. 1-8, January/February 1990.

[21] A.W. England, "The fractal dimension of diverse topographies and the effect of spatial windowing," *Geological Survey of Canada paper 90-4: Ground Penetrating Radar*, J.A. Pilon, Ed., pp. 57-61, 1992.

[22] C.G. Fox and D.E. Hayes, "Quantitative Methods for Analyzing the Roughness of the Seafloor," *Reviews of Geophysics*, vol. 23, pp. 1-48, February 1985.

[23] Bruce L. Foxworthy and Mary Hill, *Volcanic eruptions of 1980 at Mount St. Helens: The First 100 Days. U.S. Geological Survey Professional Paper 1249*, 1982.

[24] Adrian K. Fung, "*Microwave Scattering and Emission Models and Their Applications*. Boston: Artech House, 1994.

[25] A.K. Fung and K.K. Lee, "A semi-empirical sea-spectrum model for scattering coefficient estimation," *IEEE Journal of Oceanic Engineering*, vol. OE-7, pp. 166-176, 1982.

[26] L.E. Gilbert and A. Malinverno, "A Characterization of the Spectral Density of Residual Ocean Floor Topography," *Geophysical Research Letters*, vol. 15, pp. 1401-1404, November 1988.

[27] Harry Glicken, *Rockslide-debris avalanche of may 18, 1980, Mount St. Helens Volcano, Washington. U.S. Geological Survey Professional Paper 1488*, 304 pp., 7 plates, 1989.

[28] J.A. Goff, "Comment of 'Fractal Mapping of Digital Images: Application to the Topography of Arizona and Comparison With Synthetic Images' by J. Huang and D.L. Turcotte," *Journal of Geophysical Research*, vol. 95, p. 5159, 10 April 1990.

[29] Roger F. Harrington, *Time-Harmonic Electromagnetic Fields*. New York: McGraw-Hill, 1961.

[30] J. Huang and D.L. Turcotte, "Fractal Mapping of Digitized Images: Application to the Topography of Arizona and Comparisons With Synthetic Images," *Journal of Geophysical Research*, vol. 94, pp. 7491-7495, 10 June 1989.

[31] J. Huang and D.L. Turcotte, "Fractal image analysis: Application to the topography of Oregon and synthetic images, *Journal of the Optical Society of American: A*, vol. 7, pp. 1124-1130, June 1990.

[32] S.M. Kay, *Modern Spectral Estimation*. Englewood Cliffs, NJ: Prentice Hall, 1988.

[33] Z. Li and A.K. Fung, "Scattering from a Finitely Conducting Random Surface," in *Proceedings of the Progress in Electromagnetics Research Symposium (PIERS)*, Boston, 1989, p. 144.

[34] B.B. Mandelbrot, *The Fractal Geometry of Nature*. New York: W.H. Freeman and Company, 1983.

[35] B.B. Mandelbrot and J.W. Van Ness, "Fractional Brownian motions, fractional noises, and applications," *SIAM Review*, vol. 10, pp. 422-437, 1968.

[36] S.L. Marple, Jr., *Digital Spectral Analysis*. Englewood Cliffs, NJ: Prentice Hall, 1987.

[37] W.C. Meecham and W.C. Clever, "Use of C-M-W Representations for Nonlinear Random Process Applications," in *Statistical Models and Turbulence*, J. Ehlers, K. Hepp, and H.A. Weidenmüller, Eds. Berlin: Springer-Verlag, 1972.

[38] W.C. Meecham, and W.W. Lin, "Reflections from random rough surfaces," *Journal of Wave-Material Interactions*, vol. 1, pp. 4-15, 1986.

[39] William C. Meecham and Wuu-Wen Lin, "Radiation Reflected from Random Rough Surfaces," *IEEE Journal of Oceanic Engineering*, vol. OE-12, pp. 357-161, 1987.

[40] William, C. Meecham and Armand Siegel, "Wiener-Hermite Expansion in Model Turbulence at Large Reynolds Numbers," *Physics of Fluids*, vol. 7, pp. 1178-1190, 1964.

[41] J. Nakayama, H. Ogura, and B. Matsumoto, "A probabilistic theory of scattering from a random rough surface," *Radio Science*, vol. 15, pp. 1049-1057, 1980.

[42] J. Nakayama, H. Ogura, and M. Sakata, "A probabilistic theory of electromagnetic wave scattering from a slightly random surface, 1, Horizontal polarization," *Radio Science*, vol. 16, pp. 831-845, 1981.

[43] J. Nakayama, M. Sakata, and H. Ogura, A probabilistic theory of electromagnetic wave scattering from a slightly random surface, 2, Vertical polarization," *Radio Science*, vol. 16, pp. 847-853, 1981.

[44] C. Eric Nance, "Scattering and Image Analysis of Conducting Rough

Surfaces," Doctoral Dissertation, University of Texas at Arlington, May 1992.

[45] C.E. Nance, A.K. Fung, and J.W. Bredow, "Comparison of Integral Equation Predictions and Experimental Backscatter Measurements from Random Conducting Rough Surfaces," *Proceedings of the International Geoscience and Remote Sensing Symposium (IGARSS '90)*, College Park, Maryland, 1990, pp. 477-480.

[46] A. Nashashibi, K. Sarabandi, and F.T. Ulaby, "A Calibration Technique for Polarimetric Coherent-on-Receiver Radar Systems," submitted to *IEEE Transactions on Antennas and Propagation*, 1994.

[47] A.V. Oppenheim and R.W. Schafer, *Digital Signal Processing*. Englewood Cliffs, NJ: Prentice Hall, 1975.

[48] W.H. Press, B.P. Flannery, S.A. Teukolsky, and W.T. Vetterling, *Numerical Recipes (FORTRAN Version)*. Cambridge: Cambridge University Press, 1989.

[49] S.O. Rice, "Reflection of Electromagnetic Waves from Slightly Rough Surfaces," *Communications in Pure and Applied Mathematics*, vol. 4, pp. 361-378, 1951.

[50] George T. Ruck, Donald E. Barrick, William D. Stuart, and Clarence K. Krichbaum, *Radar Cross Section Handbook*, 2 volumes. New York: Plenum Press, 1970.

[51] D. Saupe, "Algorithms for random fractals," in *The Science of Fractal Images*, H.-O. Peitgen and D. Saupe, Eds. New York: Springer-Verlag, 1988, pp. 71-136.

[52] R.S. Sayles and T.R. Thomas, "Surface topography as a nonstationary random process," *Nature*, vol. 271, pp. 431-434, 1978.

[53] Thomas B.A. Senior, *Mathematical Methods in Electrical Engineering*. Cambridge: Cambridge University Press, 1986.

[54] Alexander Slingeland, "Creating Surfaces with Mastercam Mill & the Techno Computer Controlled Milling Machine," EECS 499 Directed Study, University of Michigan, May 1993.

[55] Steven R. Thiel, "Determination of a Lossy Dielectric Material That Can Be Used in the Casting/Molding Process," EECS 499 Directed Study, University of Michigan, December 1991.

[56] F.T. Ulaby and C. Elachi, Editors, *Radar Polarimetry for Geoscience Applications*. Norwood, MA: Artech House, 1990.

[57] Fawwaz T. Ulaby, Thomas F. Haddock, and Richard T. Austin, "Fluctuation Statistics of Millimeter-Wave Scattering From Distributed Targets," *IEEE Transactions on Geoscience and Remote Sensing*, vol. 26, pp. 268-181, May 1988.

[58] Fawwaz T. Ulaby, Thomas F. Haddock, Richard T. Austin, and Yasuo Kuga, "Millimeter-wave radar scattering from snow: 2. Comparison of theory with experimental observations," *Radio Science*, vol. 26, pp. 343-351, 1991.

[59] F.T. Ulaby, R.K. Moore, and A.K. Fung, *Microwave Remote Sensing: Active and Passive*, vol. II. Reading, MA: Addison-Wesley, 1982.

[60] R.F. Voss, "Fractals in Nature: From characterization to stimulation," in *The Science of Fractal Images*, H.-O. Peitgen and D. Saupe, Eds. New York: Springer-Verlag, 1988, pp. 21-70.

[61] P.D. Welch, "The Use of Fast Fourier Transform for the Estimation of Power Spectra: A Method Based on Time Averaging Over Short, Modified Periodograms," *IEEE Transactions on Audio and Electroacoustics*, vol. AU-15, pp. 70-73, June 1967.

[62] Michael W. Whitt, Fawwaz T. Ulaby, and Thomas F. Haddock, "The Development of a Millimeter-wave Network Analyzer Based Scatterometer," Radiation Laboratory Report 022872-1-T, University of Michigan, January 1987.

[63] N. Wiener, *Nonlinear Problems in Random Theory*. Cambridge: MIT Press, 1958.

[64] R.E. Ziemer and W.H. Tranter, *Principles of Communications: Systems, Modulation, and Noise*, 2nd ed. Boston: Houghton Mifflin Company, 1985.

[65] Austin, R.T., and A.W. England, Radar scattering from volcanic debris flows, *Progress in Electromagnetic Research Symposium*, 1991, Cambridge, MA, July 1-5, 1991.

[66] Austin, R.T., and A.W. England, Surface characterization of volcanic debris flows at multiple scales, *Proc. of IGARSS'91*, pp. 1675-1678, Espoo, Finland, June 3-6, 1991.

[67] Austin, R.T., and A.W. England, Multi-scale roughness spectra of volcanic debris flows, *Lunar and Planetary Science Conf. XXIII*, Houston, Texas, March 16-20, 1992.

[68] Austin, R.T., and A.W. England, Radar scattering by volcanic debris flow surface analogues, *Proc. of IGARSS'94*, Pasadena, CA, August 8-12, 1994.

[69] Austin, R.T., *Electromagnetic Wave Scattering by Power-Law Surfaces*, a dissertation submitted in partial fulfillment of the requirements for the degree of Doctor of Philosophy in Electrical Engineering at The University of Michigan, 1994.